



THE HONG KONG  
POLYTECHNIC UNIVERSITY

香港理工大學

Pao Yue-kong Library

包玉剛圖書館

---

## Copyright Undertaking

This thesis is protected by copyright, with all rights reserved.

**By reading and using the thesis, the reader understands and agrees to the following terms:**

1. The reader will abide by the rules and legal ordinances governing copyright regarding the use of the thesis.
2. The reader will use the thesis for the purpose of research or private study only and not for distribution or further reproduction or any other purpose.
3. The reader agrees to indemnify and hold the University harmless from and against any loss, damage, cost, liability or expenses arising from copyright infringement or unauthorized usage.

### IMPORTANT

If you have reasons to believe that any materials in this thesis are deemed not suitable to be distributed in this form, or a copyright owner having difficulty with the material being included in our database, please contact [lbsys@polyu.edu.hk](mailto:lbsys@polyu.edu.hk) providing details. The Library will look into your claim and consider taking remedial action upon receipt of the written requests.

**STUDY OF LEAD-FREE  
FERROELECTRIC CERAMICS WITH  
TUNABLE PHOTOLUMINESCENCE  
PROPERTIES**

**CHAN YI LOK**

**M. Phil**

**The Hong Kong Polytechnic University**

**2018**

**The Hong Kong Polytechnic University**

**Department of Applied Physics**

**Study of Lead-free Ferroelectric Ceramics with  
Tunable Photoluminescence Properties**

**Chan Yi Lok**

A thesis submitted in partial fulfillment of the requirements for  
The degree of Master of Philosophy

**August 2017**

# CERTIFICATE OF ORIGINALITY

I hereby declare that this thesis is my own work and that, to the best of my knowledge and belief, it reproduces no material previously published or written, nor material that has been accepted for the award of any other degree or diploma, except where due acknowledgement has been made in the text.

\_\_\_\_\_ (Sign)

\_\_\_\_\_ Chan Yi Lok \_\_\_\_\_ (Name of student)

**Abstract**

Rare-earth (RE) dopants can not only improve the functional properties of ceramics but also produce photoluminescence (PL) emissions. Depending on the RE dopants, up-conversion (UC) and down-conversion (DC) PL emissions can be obtained. With the use of external stimuli, such as electric field (E-field) and chemical reaction, tuning PL can be achieved. Tunable PL property plays an important role in optical applications, such as biological labeling, volumetric 3D displays and long-distance quantum communication if rapid and reversible manipulation is realized. In this work, external E-field has been chosen as stimulus to tune PL. Applying external E-field, phase change might result, thus structural symmetry could be enhanced and the PL emission will be weakened. Therefore, it is anticipated that turning PL at room temperature might be possible when the transition temperature  $T_m$  (i.e., the temperature at which the dielectric constant becomes maximum) of the sample is close to room temperature. This work thus aims to develop new lead-free RE-doped barium zirconate titanate (BZT)-based ceramics with tunable PL properties under E-field at room temperature. Ferroelectric ceramics BZT has been chosen as the host mainly because of their adjustable  $T_m$  by the Zr/Ti ratio. Three RE ions,  $Dy^{3+}$ ,  $Er^{3+}$  and  $Eu^{3+}$ , have been doped into the BZT ceramics as activators for producing PL emissions. The PL response of the RE-doped BZT ceramics have been studied under E-field.

$BaZr_xTi_{1-x}O_3$  (BZT-x) ceramics with  $x = 0.15, 0.2, 0.25$  and  $0.3$  have been fabricated by solid-state reaction for selecting suitable host for the doping of RE ions. In consistent with other research works, the  $T_m$  of the ceramics determined based on their temperature-dependent dielectric properties decreases with increasing Zr content. For the BZT-x ceramics with  $x = 0.15$  and  $0.2$ , their  $T_m$  are close to room temperature, and thus they are



selected as the host ceramics in this work. Probably due to the decrease in  $T_m$ , both the ferroelectric and piezoelectric properties of the ceramics are weakened with increasing Zr content.

Three groups of RE-doped samples have been fabricated using solid-state reaction method; they are: (i) BZT-x ceramics ( $x = 0.15$  and  $0.2$ ) doped with  $0.2 \text{ mol\% Dy}^{3+}$  (BZT-x-Dy); (ii) BZT-x ceramics ( $x = 0.1, 0.15$  and  $0.2$ ) doped with  $0.2 \text{ mol\% Er}^{3+}$  (BZT-x-Er); and (iii) BZT-x ceramics ( $x = 0.15, 0.175$  and  $0.2$ ) doped with  $0.2 \text{ mol\% Eu}^{3+}$  (BZT-x-Eu). All the samples are also abbreviated as BZT-x-RE. The XRD results indicate that the three RE ions have successfully diffused into the host and no impurity phases are observed within the detection limit. The in-situ XRD results of BZT-0.15-Er ceramic reveals rhombohedral-to-cubic phase change and strain might be induced by external E-field. The  $T_m$  of the BZT-0.15-RE and BZT-0.2-RE ceramics are found in the range of  $62\text{-}67^\circ\text{C}$  and  $30\text{-}37^\circ\text{C}$ , respectively. The doping of  $\text{Er}^{3+}$  or  $\text{Eu}^{3+}$  ions significantly improves the piezoelectric properties of the BZT-x ceramics while the effect of the  $\text{Dy}^{3+}$ -doping is relatively weak. The UC PL properties of the BZT-x-Er ceramics have been studied. Based on the power-dependent measurements, multi-photon absorption process is confirmed in the UC emission. Typical DC PL emissions are obtained for all the BZT-x-RE ceramics. For studying the effects of structural phase change, the UC PL emissions of the BZT-0.15-Er ceramic and the DC PL emissions of the BZT-x-Eu ( $x = 0.15$  and  $0.175$ ) ceramics have been measured as functions of temperature. In general, the PL intensity decreases with increasing temperature as multiphonon relaxation rate is enhanced. Our results also show that the thermally induced rhombohedral-to-cubic phase change decreases the PL intensity. Moreover, the result of the BZT-0.15-Er ceramic



reveals the occurrence of thermal agitation (TAG) between two thermally coupled emission levels  $^4S_{3/2}$  and  $^2H_{11/2}$ .

The PL responses under E-field for the BZT-x-RE ceramics have been studied. The observed PL intensities of all the BZT-x-RE ceramics are found diminished under a sufficiently high E-field. Phase change induced by E-field is believed to be the major cause for the weakening of PL intensity. Under a sufficiently high E-field, rhombohedral-to-cubic phase change happens for all the BZT-x-RE ceramics (except BZT-0.1-Er), and thus leading to an enhancement in structural symmetry and then a reduction in PL intensity. For the BZT-0.1-Er ceramic, rhombohedral-to-orthorhombic as well as orthorhombic-to-tetragonal phase changes occur under an E-field. As their effects on structural symmetry are opposed, the overall change in PL intensity becomes insignificant. Under an E-field of 2 kV/mm, the BZT-0.2-RE ceramics, which contain more cubic phase at room temperature, show less change ( $< 10\%$ ) in PL intensity as compared to the BZT-0.15-RE ceramics ( $\geq 20\%$ ). Among all the ceramics, the BZT-0.15-Er ceramic exhibits the largest reduction in PL intensity (75-80%) under an E-field of 2 kV/mm. Different from the other two dopants,  $Er^{3+}$  is reported to be more sensitive to the crystal symmetry of the host. However, the recovery of PL intensity for all the ceramics is small, generally less than 10% upon the removal of E-field. This suggests that the reversibility of the E-field-induced PL response is not high.



## Acknowledgements

I would like to express sincere gratitude to my supervisor, Dr. K. W. Kwok for his patience, advice, support and encouragement throughout my whole study.

Moreover, I gratefully acknowledge the technical support provided by the Materials Research Centre of the Hong Kong Polytechnic University. Without their help, I cannot finish my experimental work readily.

I would also like to thank all members in Dr. Kwok's group, especially Dr. Xiao Wu, Miss Hailing Sun, Mr. Tak Hang Chung, Mr. Ho Fung Ting and Mr. Rui Wen for their friendship, help and valuable discussions on my experiments. In addition, I would like to give my sincere thanks to my colleagues in our department, Miss Mei Yan Tse, Mr. Ming Kiu Tsang, Miss Yuen Ting Wong, Mr. Chi Man Wong, Mr. Ka Kit Wong and Mr. Man Chung Wong for their great help and assistance. I would also like to thank Mr. Jun Li (Functional Materials Research Laboratory, Tongji University, China) for his technical support.

Last but not the least, I am deeply indebted to my family and friends for their understanding, constant support and encouragement.



## Table of Contents

Abstract.....	I
Acknowledgements.....	IV
Table of Contents .....	V
List of Figures .....	IX
List of Tables.....	XV
Chapter 1 Introduction.....	1
1.1. Ferroelectric materials.....	1
1.1.1. Perovskite structure.....	2
1.1.2. Lead-free piezoelectric ceramics .....	3
1.1.3. Barium zirconate titanate (BZT).....	4
1.2. Luminescence.....	10
1.3. Photoluminescence.....	10
1.4. Up-conversion process .....	11
1.5. Down-conversion process .....	15
1.6. Rare-earth ions (RE ions).....	16
1.6.1. Dysprosium ion ( $\text{Dy}^{3+}$ ion) .....	18
1.6.2. Erbium ion ( $\text{Er}^{3+}$ ion) .....	19
1.6.3. Europium ion ( $\text{Eu}^{3+}$ ion) .....	21
1.7. Tunable photoluminescence properties.....	23
1.8. Motivation of research .....	29
1.9. Scope of work .....	30



Chapter 2	Sample Fabrication and Characterization .....	31
2.1.	Fabrication procedure of the ceramics .....	31
2.2.	Characterization procedure .....	32
2.2.1.	Crystalline structure .....	32
2.2.2.	Microstructure .....	33
2.2.3.	Dielectric properties .....	34
2.2.3.1.	Dielectric constant and dielectric loss.....	35
2.2.3.2.	Temperature dependence of dielectric properties .....	35
2.2.4.	Ferroelectric properties .....	36
2.2.5.	Piezoelectric properties .....	38
2.2.6.	Photoluminescence properties.....	38
2.2.6.1.	Temperature dependence of PL properties.....	40
2.2.6.2.	Preparation of transparent electrode .....	40
Chapter 3	BZT Ceramics .....	41
3.1.	Introduction.....	41
3.2.	Crystalline structure .....	41
3.3.	Microstructure .....	43
3.4.	Dielectric properties .....	44
3.4.1.	Dielectric constant and dielectric loss.....	44
3.4.2.	Temperature dependence of dielectric properties .....	45
3.5.	Ferroelectric properties .....	48
3.6.	Piezoelectric properties .....	49
3.7.	Conclusions.....	49



---

**THE HONG KONG POLYTECHNIC UNIVERSITY**

Chapter 4	RE-Doped BZT Ceramics .....	50
4.1.	Introduction.....	50
4.2.	Crystalline structure .....	51
4.3.	Microstructure .....	55
4.4.	Dielectric properties .....	58
4.4.1.	Dielectric constant and dielectric loss.....	58
4.4.2.	Temperature dependence of dielectric properties .....	59
4.5.	Ferroelectric properties .....	65
4.6.	Piezoelectric properties .....	67
4.7.	Photoluminescence properties.....	68
4.7.1.	Up-conversion PL properties .....	68
4.7.2.	Down-conversion PL properties .....	74
4.7.2.1.	BZT-x-Dy ceramics.....	74
4.7.2.2.	BZT-x-Er ceramics.....	79
4.7.2.3.	BZT-x-Eu ceramics .....	81
4.7.3.	Temperature dependence of PL properties.....	84
4.7.3.1.	BZT-x-Er ceramics .....	84
4.7.3.2.	BZT-x-Eu ceramics .....	86
4.8.	Conclusions.....	89
Chapter 5	Electric Field-Induced PL Response of RE-Doped BZT Ceramics.....	91
5.1.	Introduction.....	91
5.2.	BZT-x-Dy ceramics.....	92
5.3.	BZT-x-Er ceramics.....	95



**THE HONG KONG POLYTECHNIC UNIVERSITY**

5.4. BZT-x-Eu ceramics ..... 105

5.5. Conclusions ..... 110

Chapter 6 Conclusions ..... 111

References ..... 114



List of Figures

**FIGURE 1-1** RELATIONSHIP OF PIEZOELECTRIC AND SUBGROUPS BASED ON CRYSTAL SYMMETRY [2]. ..... 2

**FIGURE 1-2** UNIT CELL STRUCTURE OF A PEROVSKITE HAS A CHEMICAL FORMULA  $ABO_3$ ..... 3

**FIGURE 1-3** PHASE DIAGRAM OF BZT-X CERAMICS WITH  $0 \leq x \leq 0.3$  OBTAINED FROM DIELECTRIC SPECTRA MEASURED AT 1 KHZ [15]. ..... 5

**FIGURE 1-4** PHASE DIAGRAM OF BZT-X SOLID SOLUTION WITH  $0 \leq x \leq 0.3$  OBTAINED FROM RESONANT FREQUENCY CURVES AND DIELECTRIC SPECTRA [18]. ..... 6

**FIGURE 1-5** LATENT HEATS AT CURIE POINT MEASURED WITH DTA OF BZT CERAMICS [17]. ..... 7

**FIGURE 1-6** SCHEMATIC DIAGRAM OF PL PROCESSES OF EMISSION (A) BY ACTIVATOR, (B) BY ACTIVATOR AND SENSITIZER, WITHIN THE HOST LATTICE. .... 11

**FIGURE 1-7** SCHEMATIC DIAGRAM OF FIVE BASIC MECHANISMS OF UP-CONVERSION PROCESS, (A) ESA, (B) ETU, (C) CUC, (D) PA AND (E) EMU. (E) RANDOM HOPPING AMONG TYPE III IONS IS INDICATED AS “NX”. LINE COLORS DO NOT INDICATE WAVELENGTHS. .... 12

**FIGURE 1-8** ENERGY LEVELS OF TRIVALENT RARE-EARTH ION IN  $LaF_3$  WITH ANTICIPATED EMITTING STATES IN THE VISIBLE, NEAR IR AND UV REGION MARKED WITH RED DOTS [49]. ..... 17

**FIGURE 1-9** ENERGY LEVELS DIAGRAM OF  $Dy^{3+}$  ..... 19

**FIGURE 1-10** ENERGY LEVELS DIAGRAM OF  $Er^{3+}$ . ..... 20

**FIGURE 1-11** ENERGY LEVELS DIAGRAM OF  $Eu^{3+}$ . ..... 22

**FIGURE 1-12** (A) THE FINE SCAN XRD PATTERN AND (B) PL RESPONSE UNDER OF BCTZ:Pr MEASURED WITH APPLYING THE OFF AND ON-FIELD FOR THREE CYCLES [78]. ..... 24

**FIGURE 1-13** THE TEMPERATURE DEPENDENCE DIELECTRIC PROPERTIES MEASURED WITH POLED AND UNPOLED SAMPLE [78]. ..... 25

**FIGURE 1-14** THE PL RESPONSE UNDER SIX CYCLES OF E-FIELD AND THE XRD PATTERN UNDER 5<sup>TH</sup> AND 10<sup>TH</sup> CYCLE OF E-FIELD [78]. ..... 25



**FIGURE 1-15** PL SPECTRA MEASURED WITH (A) UNPOLED AND (B) POLED BNT-6BT: EU SPECIMENS. THE INSETS ARE THE MAGNIFIED OF THE  $^5D_0 \rightarrow ^7F_0$  STARK LINE [80]..... 27

**FIGURE 1-16** PL SPECTRUM OF (A) UNPOLED SAMPLE, (B) SAMPLE UNDER AN E-FIELD OF 3.5 KV/MM AND (C) SAMPLE AFTER REMOVAL OF FIELD MEASURED AT 80°C [80]. ..... 27

**FIGURE 1-17** (A) EMISSION SPECTRUM OF ER-DOPED PMN-PT CERAMICS UNDER DIFFERENT STRENGTHS OF E-FIELD AND INSERTED PHOTO OF ACTUAL FLUORESCENCE; (B) THE INTEGRATED INTENSITY OF EMISSION AGAINST THE BIAS E-FIELD GRAPH [81]. ..... 28

**FIGURE 1-18** MONOPOLAR E-FIELD-INDUCED STRAIN (SE) LOOP OF ER-DOPED PMN-PT CERAMICS MEASURED AT ROOM TEMPERATURE [81]..... 29

**FIGURE 2-1** FLOW DIAGRAM OF THE FABRICATION PROCEDURE..... 32

**FIGURE 2-2** THE SCHEMATIC DIAGRAM OF X-RAY DIFFRACTION IN CRYSTAL..... 33

**FIGURE 2-3** THE SCHEMATIC DIAGRAM OF A FE-SEM. .... 34

**FIGURE 2-4** THE SCHEMATIC DIAGRAM OF TEMPERATURE DEPENDENCE DIELECTRIC MEASUREMENT SETUP. .... 36

**FIGURE 2-5** PE LOOP WITH FERROELECTRIC PARAMETERS MARKED ON IT. .... 36

**FIGURE 2-6** THE SCHEMATIC DIAGRAM OF PE LOOP MEASUREMENT SETUP. .... 37

**FIGURE 2-7** THE SCHEMATIC DIAGRAM OF POLING SETUP. .... 38

**FIGURE 2-8** SAMPLE CHAMBER WITH OPTIONAL POLARIZERS AND LASER COUPLING FLANGE [85]. ..... 39

**FIGURE 3-1** THE XRD PATTERNS OF THE BZT-X CERAMIC POWDERS IN THE RANGE OF (A) 20-80° AND (B) 44-46°..... 42

**FIGURE 3-2** FE-SEM MICROGRAPH OF BZT-X CERAMICS. (A) X = 0.15, (B) X = 0.2, (C) AND (D) X = 0.25, (E) X = 0.3. .... 44

**FIGURE 3-3** TEMPERATURE DEPENDENCE OF DIELECTRIC PROPERTIES OF BZT-X CERAMICS (A) X = 0.15, (B) X = 0.2, (C) X = 0.25 AND (D) X = 0.3. .... 46



---

THE HONG KONG POLYTECHNIC UNIVERSITY

**FIGURE 3-4** PLOT OF  $\ln(1/E_R - 1/E_M)$  AGAINST  $\ln(T - T_M)$  FOR THE BZT-0.15 AND BZT-0.2 CERAMICS AT 10 KHZ. .... 47

**FIGURE 3-5** PE LOOPS OF BZT-X CERAMICS. .... 48

**FIGURE 4-1** THE XRD PATTERNS OF THE BZT-0.15 AND BZT-X-DY CERAMICS POWDERS IN THE RANGE OF (A) 20-80° AND (B) 44-46° ..... 52

**FIGURE 4-2** THE XRD PATTERNS OF THE BZT-0.15 AND BZT-X-ER CERAMICS POWDERS IN THE RANGE OF (A) 20-80° AND (B) 44-46° ..... 52

**FIGURE 4-3** THE XRD PATTERNS OF THE BZT-0.15 AND BZT-X-EU CERAMICS POWDERS IN THE RANGE OF (A) 20-80° AND (B) 44-46° ..... 53

**FIGURE 4-4** THE XRD PATTERNS OF THE BZT-0.15-ER CERAMICS IN THE RANGE OF (A) 44-45.5° AND (B) 55-56.5° UNDER AN EXTERNAL E-FIELD OF 0-2000 V/MM. .... 54

**FIGURE 4-5** FE-SEM MICROGRAPHS OF BZT-X-DY CERAMICS, (A) X = 0.15 AND (B) X = 0.2. .... 55

**FIGURE 4-6** FE-SEM MICROGRAPHS OF BZT-X-ER CERAMICS, (A) X = 0.1, (B) X = 0.15 AND (C) X = 0.2. .... 56

**FIGURE 4-7** FE-SEM MICROGRAPHS OF BZT-X-EU CERAMICS, (A) X = 0.15, (B) X = 0.175 AND (C) X = 0.2. .... 57

**FIGURE 4-8** TEMPERATURE DEPENDENCE OF DIELECTRIC PROPERTIES OF BZT-X-DY CERAMICS, (A) X = 0.15 AND (B) X = 0.2. .... 60

**FIGURE 4-9** TEMPERATURE DEPENDENCE OF DIELECTRIC PROPERTIES OF BZT-X-ER CERAMICS, (A) X = 0.1, (B) X = 0.15 AND (C) X = 0.2. .... 61

**FIGURE 4-10** TEMPERATURE DEPENDENCE OF DIELECTRIC PROPERTIES OF BZT-X-EU CERAMICS, (A) X = 0.15, (B) X = 0.175 AND (C) X = 0.2. .... 62

**FIGURE 4-11** PLOT OF  $\ln(1/E_R - 1/E_M)$  AGAINST  $\ln(T - T_M)$  FOR THE BZT-X-DY CERAMICS AT 10 KHZ. .. 63

**FIGURE 4-12** PLOT OF  $\ln(1/E_R - 1/E_M)$  AGAINST  $\ln(T - T_M)$  FOR THE BZT-X-ER CERAMICS AT 10 KHZ. .... 63

**FIGURE 4-13** PLOT OF  $\ln(1/E_R - 1/E_M)$  AGAINST  $\ln(T - T_M)$  FOR THE BZT-X-EU CERAMICS AT 10 KHZ. .. 64



<b>FIGURE 4-14</b> PE LOOPS OF BZT-X-DY CERAMICS. ....	65
<b>FIGURE 4-15</b> PE LOOPS OF BZT-X-ER CERAMICS. ....	66
<b>FIGURE 4-16</b> PE LOOP OF BZT-X-EU CERAMICS. ....	66
<b>FIGURE 4-17</b> (A) UC PL EMISSION SPECTRA UNDER 980-NM LASER EXCITATION WITH POWER DENSITIES RANGING FROM 0.278 TO 1.705 W/CM <sup>2</sup> AND THE INSET SHOWS THE RED EMISSION LOCATED BETWEEN 640 AND 680 NM, (B) EMISSION INTENSITIES AGAINST LASER POWER DENSITIES AND (C) NORMALIZED INTENSITIES AGAINST TIME MEASURED UNDER 0.278 W/CM <sup>2</sup> EXCITATION OF BZT-0.15-ER THIN CERAMICS SAMPLE WITH ITO ELECTRODE.....	71
<b>FIGURE 4-18</b> UC PL EMISSION SPECTRA UNDER 980-NM LASER EXCITATION WITH POWER DENSITIES RANGING FROM 0.278 TO 1.705 W/CM <sup>2</sup> OF BZT-X-ER THICK CERAMICS SAMPLES. THE INSET SHOWS THE RED EMISSION LOCATED BETWEEN 640 AND 680 NM, (A) X = 0.1, (B) X = 0.15 AND (C) X = 0.2...	73
<b>FIGURE 4-19</b> UC EMISSION INTENSITIES AGAINST LASER POWER DENSITIES OF BZT-X-ER THICK CERAMIC SAMPLES. (A) X = 0.1, (B) X = 0.15 AND (C) X = 0.2.....	74
<b>FIGURE 4-20</b> DC PLE SPECTRA OF BZT-X-DY CERAMICS MONITORED AT (A) 475 NM AND (B) 574 NM, AND DC PL EMISSION SPECTRA OF BZT-X-DY AND BNT-6BT CERAMICS UNDER (C) 388.5-NM, (D) 428.5-NM AND (E) 454-NM EXCITATION. ....	78
<b>FIGURE 4-21</b> DC PLE SPECTRA OF EMISSION PEAKS AT (A) 532.5, (B) 545 AND (C) 670 NM, (D) EMISSION SPECTRA UNDER 488.5-NM EXCITATION OF BZT-X-ER CERAMICS AND THE INSET IS THE RED EMISSION. ....	81
<b>FIGURE 4-22</b> DC PLE SPECTRA OF EMISSION AT (A) 596 NM AND (B) 615 NM OF BZT-X-EU CERAMICS, (C) DC PL EMISSION SPECTRA UNDER 466-NM AND 530-NM EXCITATION OF BZT-0.175-EU CERAMICS, (D) DC PL EMISSION SPECTRA UNDER 466-NM EXCITATION OF BZT-X-EU CERAMICS.....	83
<b>FIGURE 4-23</b> (A) 3D PLOT OF TEMPERATURE DEPENDENT UC PL EMISSION SPECTRA AND (B) NORMALIZED INTENSITIES OF TWO GREEN EMISSION PEAKS VERSUS TEMPERATURE OF BZT-0.15-ER CERAMIC. ....	85



**FIGURE 4-24** 3D PLOTS OF TEMPERATURE DEPENDENT DC PL EMISSION SPECTRA BZT-X-EU CERAMICS, (A) X = 0.15 AND (B) X = 0.175. NORMALIZED INTENSITIES OF TWO GREEN EMISSION PEAKS VERSUS TEMPERATURE OF BZT-X-EU CERAMICS (WITH BACKGROUND SUBTRACTED), (C) X = 0.15 AND (D) X = 0.175..... 88

**FIGURE 5-1** (A) DC PL RESPONSE UNDER DIFFERENT E-FIELDS OF BZT-0.15-DY, DC PL RESPONSE OF BZT-X-DY CERAMICS UNDER E-FIELD AND REMOVAL OF FIELD (B) X = 0.15 AND (C) X = 0.2..... 94

**FIGURE 5-2** UC PL RESPONSE UNDER (A) DIFFERENT E-FIELDS, AND (B) UNDER E-FIELD AND REMOVAL OF FIELD OF BZT-0.1-ER CERAMIC..... 96

**FIGURE 5-3** DC PL RESPONSE UNDER (A) DIFFERENT E-FIELDS, AND (B) UNDER E-FIELD AND REMOVAL OF FIELD OF BZT-0.1-ER CERAMIC..... 97

**FIGURE 5-4** UC PL RESPONSE UNDER (A) DIFFERENT E-FIELDS, (B) E-FIELD AND REMOVAL OF FIELD, AND (C) UC EMISSION SPECTRA WITH AN ADDITIONAL PEAK FOUND AT 567.5 NM WHEN AN E-FIELD OF 2 KV/MM IS APPLIED, OF BZT-0.15-ER CERAMIC..... 100

**FIGURE 5-5** DC PL RESPONSE UNDER (A) DIFFERENT E-FIELDS, (B) AND (C) UNDER E-FIELD AND REMOVAL OF FIELD OF BZT-0.15-ER CERAMIC..... 101

**FIGURE 5-6** (A) VARIATION OF APPLIED E-FIELD AND (B) THE TWO OBSERVED DC PL INTENSITIES OF BZT-0.15-ER CERAMIC..... 103

**FIGURE 5-7** DC PL RESPONSE (AT 548 NM) OF BZT-0.15-ER CERAMIC AT 0 V/MM AND 1 KV/MM IN THE 10 CONSECUTIVE E-FIELD CYCLES. THE INSET IS THE MAGNIFIED 2<sup>ND</sup> - 10<sup>TH</sup> CYCLES..... 103

**FIGURE 5-8** (A) UC AND (B) DC PL RESPONSE UNDER DIFFERENT E-FIELDS OF BZT-0.2-ER CERAMIC. 105

**FIGURE 5-9** DC PL RESPONSE UNDER (A) DIFFERENT E-FIELDS, (B) UNDER E-FIELD AND REMOVAL OF FIELD OF BZT-0.15-EU CERAMIC..... 106

**FIGURE 5-10** DC PL RESPONSE UNDER (A) DIFFERENT E-FIELDS, (B) UNDER E-FIELD AND REMOVAL OF FIELD OF BZT-0.175-EU CERAMIC..... 108



---

THE HONG KONG POLYTECHNIC UNIVERSITY

FIGURE 5-11 DC PL RESPONSE UNDER (A) DIFFERENT E-FIELDS, (B) UNDER E-FIELD AND REMOVAL OF  
FIELD OF BZT-0.2-EU CERAMIC..... 109



## List of Tables

<b>TABLE 1</b> THE TEMPERATURE OF DIELECTRIC CONSTANT MAXIMUM ( $T_M$ ), DIELECTRIC CONSTANT MAXIMUM ( $\epsilon_M$ ), AND DIFFUSENESS CONSTANT ( $\gamma$ ) FOR THE FOUR SAMPLES AT 10 KHZ [26].....	8
<b>TABLE 2</b> AVERAGE GRAIN SIZES OF THE BZT-X CERAMICS.....	44
<b>TABLE 3</b> THE DIELECTRIC CONSTANT ( $\epsilon_R$ ) AND DIELECTRIC LOSS ( $\tan \delta$ ) OF BZT-X CERAMICS MEASURED AT ROOM TEMPERATURE AND 1 KHZ .....	45
<b>TABLE 4</b> $T_M$ , $E_M$ AND $\gamma$ OF THE BZT-0.15 AND BZT-0.2 CERAMICS AT 10 KHZ .....	47
<b>TABLE 5</b> $P_R$ AND $P_{SAT}$ OF THE BZT-X CERAMICS.....	49
<b>TABLE 6</b> THE PIEZOELECTRIC COEFFICIENT ( $D_{33}$ ) OF BZT-X CERAMICS .....	49
<b>TABLE 7</b> AVERAGE GRAIN SIZES OF THE BZT-X-DY CERAMICS .....	57
<b>TABLE 8</b> AVERAGE GRAIN SIZES OF THE BZT-X-ER CERAMICS.....	57
<b>TABLE 9</b> AVERAGE GRAIN SIZES OF THE BZT-X-EU CERAMICS .....	57
<b>TABLE 10</b> THE DIELECTRIC CONSTANT ( $\epsilon_R$ ) AND DIELECTRIC LOSS ( $\tan \delta$ ) OF BZT-X-RE CERAMICS MEASURED AT ROOM TEMPERATURE AND 1 KHZ .....	58
<b>TABLE 11</b> $T_M$ , $E_M$ AND $\gamma$ OF THE BZT-X-DY CERAMICS AT 10 KHZ.....	64
<b>TABLE 12</b> $T_M$ , $E_M$ AND $\gamma$ OF THE BZT-X-ER CERAMICS AT 10 KHZ.....	64
<b>TABLE 13</b> $T_M$ , $E_M$ AND $\gamma$ OF THE BZT-X-EU CERAMICS AT 10 KHZ.....	64
<b>TABLE 14</b> $P_R$ AND $P_{SAT}$ OF THE BZT-X-RE CERAMICS .....	67
<b>TABLE 15</b> THE PIEZOELECTRIC COEFFICIENT ( $D_{33}$ ) OF BZT-X-RE CERAMICS .....	68
<b>TABLE 16</b> POSITIONS OF THE NON $DY^{3+}$ EMISSION PEAKS FOUND UNDER DIFFERENT MEASURING CONDITIONS (FILTER AND EXCITATION WAVELENGTH).....	78



## **Chapter 1 Introduction**

### **1.1. Ferroelectric materials**

Materials with a switchable macroscopic polarization are classified as ferroelectric materials [1]. In 1921, ferroelectricity was first discovered in Rochelle salt, a single-crystal material [2]. During the early to mid-1940s, polycrystalline ferroelectric ceramics, barium titanate ( $\text{BaTiO}_3$ ), have been developed. In 1946, Gray has discovered that the domains within the grains can be oriented with external electric field (E-field), and therefore ceramic materials are able to perform like single crystals possessing both ferroelectric and piezoelectric properties [2], [3]. Ferroelectric ceramics has various applications, such as piezoelectric sonar transducers, radio filters and stereo tweeters, because of their high dielectric constant and electrically switchable spontaneous polarization. Piezoelectricity was first discovered in 1880 by Jacques and Pierre Curie. It is the effect of generating electricity by applying mechanical stress. In order to use the piezoelectric effect in ferroelectric ceramics, poling with a sufficiently high E-field is required. Although each of the individual crystallites of the ferroelectric ceramic is piezoelectric, the ceramic without poling is inactive.

The relationship of piezoelectric materials and subgroups based on crystal symmetry is shown in Figure 1-1. The seven basic crystal systems, which are triclinic, monoclinic, orthorhombic, tetragonal, rhombohedral, hexagonal and cubic, can be divided into 32 point groups. 21 classes of the 32 point groups are non-centrosymmetric that is a necessary condition for piezoelectric materials. However, only 20 of them are piezoelectric, the other one is not due to other combined symmetry elements.

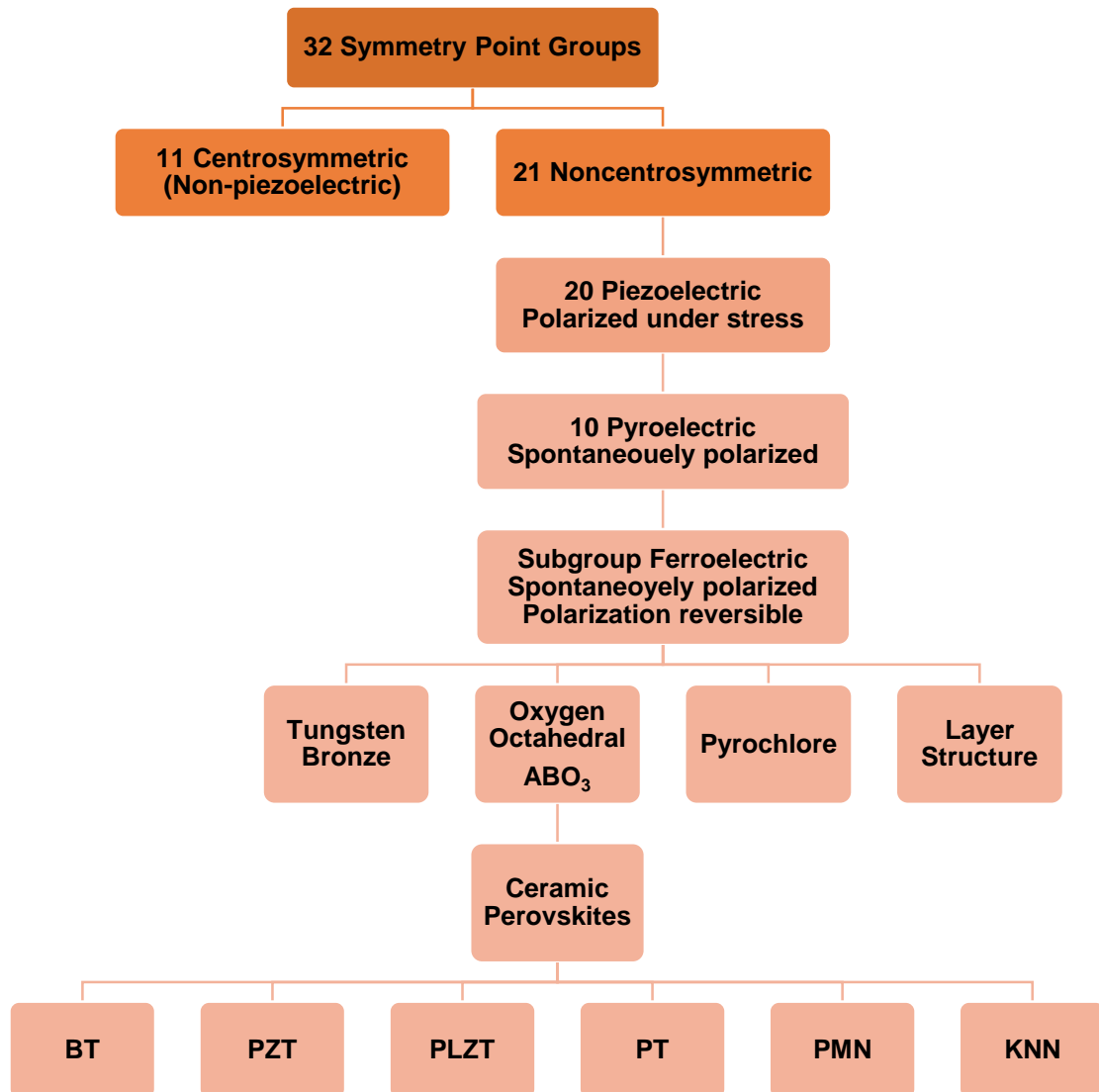
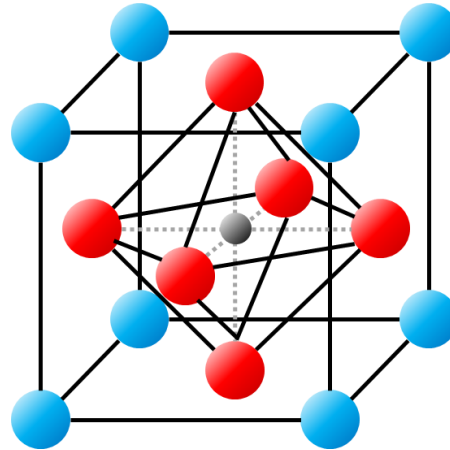


FIGURE 1-1 Relationship of piezoelectric and subgroups based on crystal symmetry [2].

### 1.1.1. Perovskite structure

A perovskite structure has a chemical formula  $ABO_3$  with oxygen located in the face centers.  $BaTiO_3$  (BT) is one of the well-known ferroelectric materials with the perovskite structure. Figure 1-2 shows a unit cell of the  $ABO_3$  structure. Using BT as an example to

explain the figure, the blue spheres represent  $\text{Ba}^{2+}$  (A site, coordination number (CN) = 12), the red spheres represent  $\text{O}^{2-}$  and the black sphere represents  $\text{Ti}^{4+}$  (B site, CN = 6).



**FIGURE 1-2** Unit cell structure of a perovskite has a chemical formula  $\text{ABO}_3$ .

When an E-field is applied to the unit cell, e.g., in the upward direction, the black spheres (B-site ions) will move along it. For ferroelectric single crystals, there are eight possible directions which are equivalent to  $[111]$  to move in rhombohedral plane; twelve directions which are equivalent to  $[101]$  in orthorhombic plane, and six directions which are equivalent to  $[001]$  in the tetragonal plane [4].

### 1.1.2. Lead-free piezoelectric ceramics

$\text{Pb}(\text{Zr}_x\text{Ti}_{1-x})\text{O}_3$  (PZT) ceramics have been widely used practically due to their high piezoelectricity [5]. The common commercial applications of PZT ceramics include actuators, transducers and sensors. These devices require materials with high longitudinal electromechanical coupling coefficient ( $k_{33}$ ) and piezoelectric coefficients ( $d_{33}$ ). Despite of their excellent piezoelectric properties, they contain more than 60 wt% of PbO which will evaporate lead during sintering at high temperatures [6], [7]. In addition, improper



disposal of PZT is considered as a serious hazard to environment and human health. Therefore, lead-free piezoelectric ceramics have been developed for replacing them.

Reported lead-free piezoelectric materials include ferroelectrics with perovskite structure, tungsten bronze structure and bismuth layer-structure. Among them, perovskite ferroelectrics exhibit high piezoelectric properties, for examples  $\text{Bi}_{0.5}\text{Na}_{0.5}\text{TiO}_3$  (BNT),  $\text{K}_{0.5}\text{Na}_{0.5}\text{NbO}_3$  (KNN),  $\text{BaTiO}_3$  (BT),  $\text{Ba}(\text{Zr}, \text{Ti})\text{O}_3$  (BZT) and  $(\text{Ba}, \text{Sr})\text{TiO}_3$  (BST). For instance,  $\text{Ba}_{0.27}\text{Sr}_{0.75}\text{Nb}_2\text{O}_{5.78}$  [8],  $\text{Ba}_{(4+x)}\text{Na}_{(2-2x)}\text{Nb}_{10}\text{O}_{30}$  [9], and  $\text{K}_{(6-x-y)}\text{Li}_{(4+x)}\text{Nb}_{(10+y)}\text{O}_{30}$  [10] are materials with tungsten bronze structure.  $\text{CaBi}_4\text{Ti}_4\text{O}_{15}$  (CBT) [11],  $\text{Bi}_4\text{Ti}_3\text{O}_{12}$  (BTO) [12] and  $(\text{Ca}, \text{Sr})\text{Bi}_4\text{Ti}_4\text{O}_{15}$  (CSBT) [13] are materials with bismuth layer-structure.

### 1.1.3. Barium zirconate titanate (BZT)

$\text{BaZr}_x\text{Ti}_{1-x}\text{O}_3$  (abbreviated as BZT-x) is one of the lead-free piezoelectric ceramics with perovskite structure. It is a possible alternative to BST for fabricating ceramic capacitors as  $\text{Zr}^{4+}$  is chemically more stable than  $\text{Ti}^{4+}$  [14].

Figure 1-3 shows the phase diagram of BZT-x with  $0 \leq x \leq 0.3$  [15].  $T_c$  is the Curie temperature above which the ferroelectric materials will become paraelectric (cubic phase).  $T_1$  is the orthorhombic-tetragonal phase transition temperature and  $T_2$  is the rhombohedral-orthorhombic phase transition temperature. As shown in Figure 1-3, the three phase transitions combine into one, i.e., the rhombohedral-cubic phase transition at  $x \geq 0.15$ . Another research shares similar results, in which the two transition temperatures  $T_1$  and  $T_c$  become the same at  $x \sim 0.11$  [16]. On the other hand, some researchers suggested that the orthorhombic and tetragonal phases still exist in a narrow temperature range below  $T_c$  even at high Zr contents (i.e., x) [17]–[19]. Based on the X-ray analysis



as well as resonance frequency studies, Kell and Hellicar [18] have identified the orthorhombic and rhombohedra structures of BZT. Figure 1-4 shows the phase diagram of the BZT-x solid solution with  $0 \leq x \leq 0.3$  proposed by them. Unlike the solutions with less Zr content (i.e.,  $x$ ), the orthorhombic and tetragonal phases exist in a narrow temperature range ( $\sim 10^\circ\text{C}$ ) below  $T_c$  for the solutions with  $x \geq 0.15$  (Figure 1-4). Hennings et al. [17] have used a hot-stage X-ray diffractometer to measure the phase transition of ceramic samples in a temperature range of  $-100$  to  $300^\circ\text{C}$ . The phases are distinguished based on the characteristic splitting of the cubic (400) perovskite reflection into separate peaks. It has been reported that the tetragonal and orthorhombic phases could be detected in the rhombohedral region at  $15^\circ\text{C}$  and  $20^\circ\text{C}$ , respectively, below  $T_c$ .

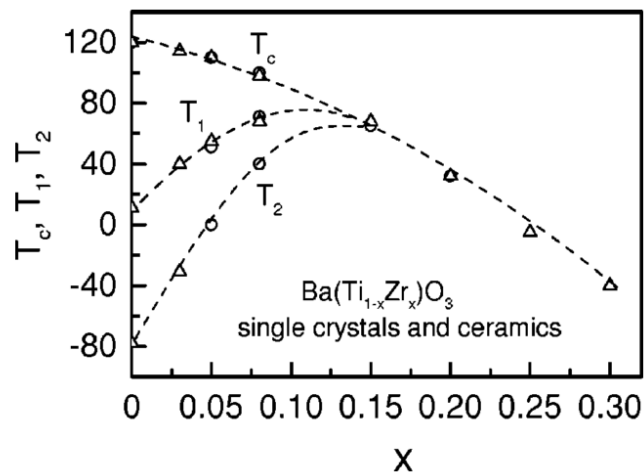


**FIGURE 1-3** Phase diagram of BZT-x ceramics with  $0 \leq x \leq 0.3$  obtained from dielectric spectra measured at 1 kHz [15].

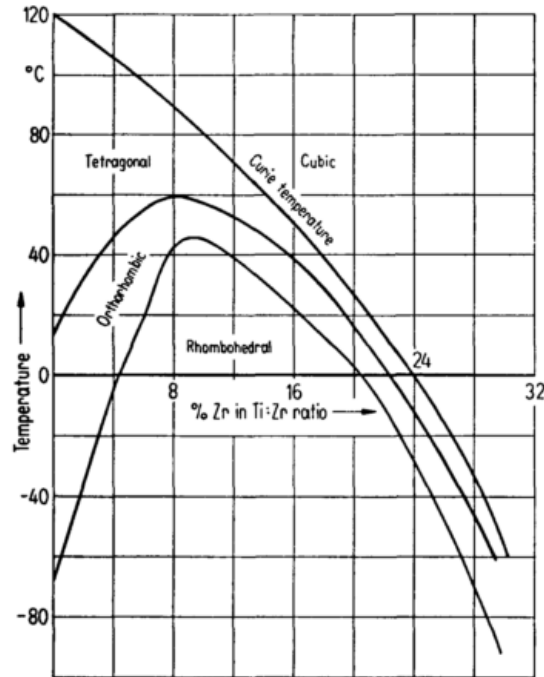


**FIGURE 1-4** Phase diagram of BZT-x solid solution with  $0 \leq x \leq 0.3$  obtained from resonant frequency curves and dielectric spectra [18].

Latent heats have also been measured for investigating the phase transitions of BZT. Figure 1-5 shows the latent heats of BZT ceramics at their  $T_c$  determined using differential thermal analysis (DTA) [17]. The latent heat decreases gradually with increasing Zr concentration (i.e.,  $y$  as used in the figure), and becomes zero at  $y = 0.09$ . Based on the relationship between the first-order phase transition and latent heat, it is concluded that the phase transition of BZT with high Zr contents (e.g.,  $y > 0.09$ ) might change from the first-order to second-order.

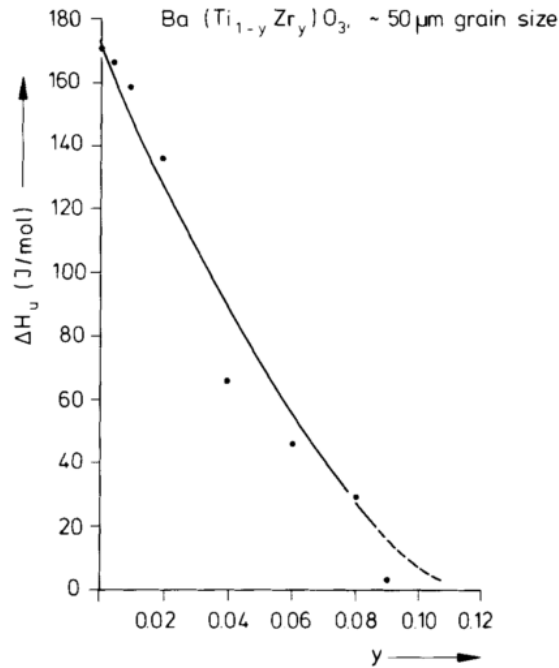


FIGURE 1-5 Latent heats at Curie point measured with DTA of BZT ceramics [17].

A diffuse phase transition has four typical characteristics. They are (1) a broadened transition peak in the dielectric constant ( $\epsilon_r$ )-temperature curve; (2) a relatively large difference between the temperatures having the maximum  $\epsilon_r$  (i.e.,  $\epsilon_m$ ) and dielectric loss ( $\tan \delta$ ); (3) a deviation from the Curie-Weiss law in the vicinity of the temperature having maximum  $\epsilon_r$  (i.e.,  $T_m$ ); and (4) a frequency dispersion for both  $\epsilon_r$  and  $\tan \delta$  near the transition region, and a frequency dependence of  $T_m$  [20]–[22]. The diffuseness of such a phase transition can be characterized using the modified Curie-Weiss law:

$$1/\epsilon_r - 1/\epsilon_m = (T - T_m)^\gamma / C' \quad (1.1)$$

where  $C'$  is the Curie-like constant and  $\gamma$  is the degree of diffuseness [23], [24].  $\gamma$  can have a value ranging from 1 for normal ferroelectrics obeying the Curie-Weiss law to 2 for ideal relaxor ferroelectrics exhibiting a complete diffuse phase transition. As indicated in Table 1, the higher Zr content of the ceramic, the stronger the diffuseness of the phase



transition is. It has also been reported that the diffuseness is affected by the grain size. For BZT-0.2 ceramic, the diffuseness decreases with increasing grain size, i.e., a fine-grained sample displays relaxor-like ferroelectric behavior while a coarse-grained sample does not [25].

**TABLE 1** The temperature of dielectric constant maximum ( $T_m$ ), dielectric constant maximum ( $\epsilon_m$ ), and diffuseness constant ( $\gamma$ ) for the four samples at 10 kHz [26]

<b>Sample</b>	<b>BZT-0.2</b>	<b>BZT-0.25</b>	<b>BZT-0.3</b>	<b>BZT-0.35</b>
$T_m$ (K)	297	257	198	166
$\epsilon_m$ (K)	7620	12250	5376	4343
$\gamma$	1.62	1.81	1.93	2.01

A high dielectric tunability (86%) has been reported for BZT-0.2 ceramics measured at room temperature under a bias E-field of 20 kV/cm at 10 kHz [26]. As the Zr content ( $x$ ) increases, the tunability decreases, giving a value of 54%, 26% and 19% for the ceramics with  $x = 0.25, 0.3$  and  $0.35$ , respectively. This is mainly because of the close proximity of the transition temperature of BZT-0.2 ceramics to room temperature [27].

Polar nano-region (PNR) is one of the directions in understanding the promising properties of BZT- $x$  ceramics. Buscaglia et al. have studied the atomic-scale structures of BZT- $x$  ceramics using high-energy X-ray diffraction and Raman spectroscopy [28]. For the ceramics with  $x = 0.1$  and  $0.2$ , some polar bands are preserved in Raman spectra measured at temperatures above  $T_c$ , indicating the presence of short-range correlated displacements on the B-site of the  $ABO_3$  structure. It is believed that the short-range correlated displacements are attributed to Ti-rich polar clusters inside a non-polar paraelectric matrix of average cubic type structure. Ti-rich polar clusters are responsible



for the long-range ferroelectric order found below  $T_c$  while Zr-rich clusters are non-polar or weakly polar. Locally associated off-centre displacement of Zr/Ti cations within the local rhombohedral symmetry are suggested as the source of polar clusters observed in the ceramics with  $x = 0.1, 0.2$  and  $0.4$ .  $Zr^{4+}$  and  $Ti^{4+}$  have a large difference in ionic radius which leads to a reduction of local strain. The reduced local strain induces the formation and growth of PNRs. In addition to the Raman results, BZT-0.2 ceramic contains both rhombohedral and cubic phases at room temperature. Xu et al. have studied the dielectric responses of fine-grained BZT-0.2 ceramics under bias E-field [29]. The ceramics have a cubic phase and exhibit frequency-dependent dielectric loss and slim PE loop which are suggested to be connected with PNRs in their paraelectric matrix. Their dielectric properties have also been found to become nonlinear under bias E-field, and the nonlinearity is dependent on the duration of the bias E-field. Based on a theoretical study of the nonlinear dielectric constants using a multi-polarization mechanism model, it is suggested that polarization reorientation of PNRs induced by the bias field is one of the possible causes for the time-dependence.

Owing to the good dielectric properties, BZT ceramics have been widely used for the fabrication of capacitors. The temperature dependence of dielectric properties, the nature of phase transitions, as well as the relaxor characteristics have been extensively investigated [17], [30], [31]. It is also a promising lead-free piezoelectric material because of its good electrostrictive and piezoelectric properties [15], [32], [33]. For the BZT- $x$  ceramics with  $x$  in the range of 0.03-0.08, the piezoelectric strain increases from 0.18% at 4 kV/mm to 25% at 12 kV/mm [15]. BZT ceramics can be used as actuator as they display linear field-induced strain [34].



## 1.2. Luminescence

Luminescence comes from a Latin root *lumen* which literally means light [35]. It is used for all phenomena of lighting that are not resulted from heat. The modern definition of it is “a spontaneous emission of radiation from an electronically excited species or from a vibrationally excited species not in thermal equilibrium with its environment” [36, p. 367]. According to the modes of excitation, different types of luminescence are classified. Photon (photoluminescence), high-energy electron beam (cathodoluminescence), electric current passed through a substance (electroluminescence), chemical reaction (chemiluminescence), stress (triboluminescence) and biochemical reaction by a living organism (bioluminescence) are possible excitation sources of luminescence. Light-emitting diode (LED) is an example of applications of electroluminescence.

## 1.3. Photoluminescence

Photoluminescence (PL) is defined as emission of light resulted from “direct photoexcitation of the emitting species” [36, p. 393]. There are three types of PL: fluorescence, phosphorescence and delayed fluorescence. Based on the duration of emission after the end of excitation, fluorescence (light disappears simultaneously with the end of excitation) and phosphorescence (light persists after the end of excitation) are classified. Delayed fluorescence is defined as “luminescence decaying more slowly than expected from the rate of decay of the emitting state” [36, p. 321].

Figure 1-6 shows the schematic diagram of two PL processes. As shown in Figure 1-6 (a), the activator, which is inside the host lattice, is excited by photon and then emits radiation and heat [37]. Another PL process involves activator and sensitizer within the

host lattice is shown in Figure 1-6 (b). The sensitizer is excited by photon and then transfers energy to the activator. Similar to the mentioned process, the activator emits the “transferred” energy as radiation and heat. The first process is often in singly doped ion system while the latter one is found in co-doped ion system.

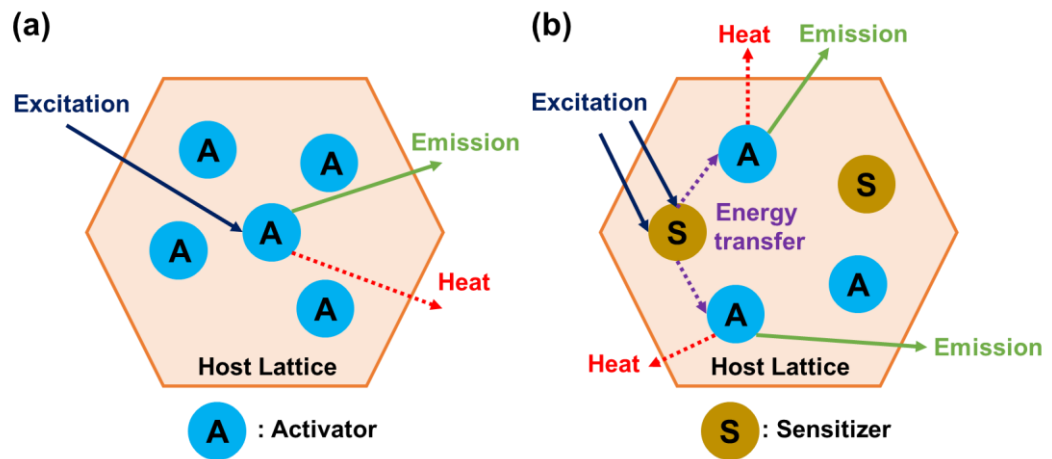


**FIGURE 1-6** Schematic diagram of PL processes of emission (a) by activator, (b) by activator and sensitizer, within the host lattice.

#### 1.4. Up-conversion process

There are five mechanisms for up-conversion (UC) process: excited state absorption (ESA), energy transfer up-conversion (ETU), cooperative up-conversion (CUC), photon avalanche (PA), and energy migration up-conversion (EMU) as illustrated in Figure 1-7 [38].

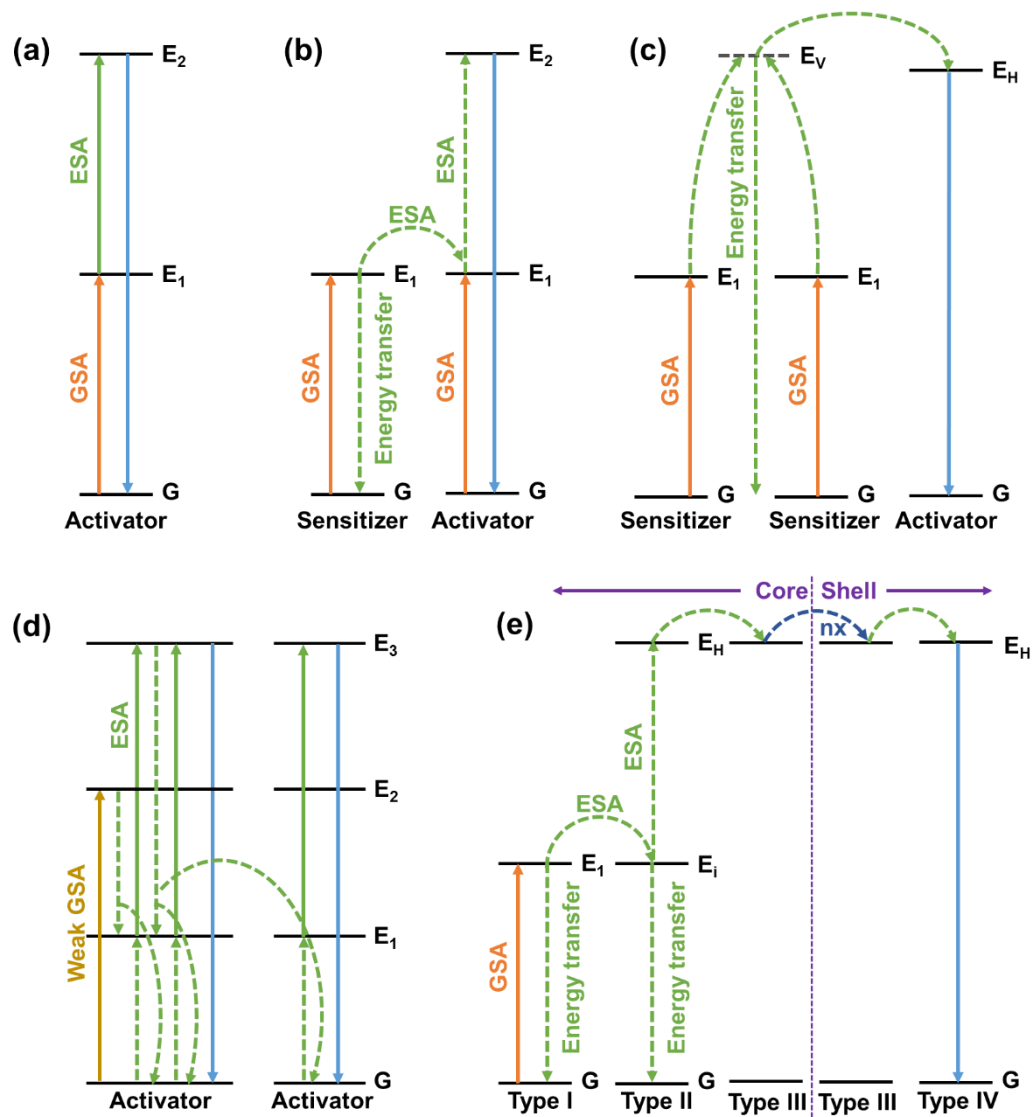


**FIGURE 1-7** Schematic diagram of five basic mechanisms of up-conversion process, (a) ESA, (b) ETU, (c) CUC, (d) PA and (e) EMU. (e) Random hopping among Type III ions is indicated as “nx”. Line colors do not indicate wavelengths.

Excited state absorption (ESA) is a UC process in a single ion which an electron absorbs at least two photons as shown in Figure 1-7 (a). The number of absorbed photons is dependent on the number of excited states. Electrons initially located in the ground state (G) is excited to a metastable excited state (E<sub>1</sub>) via absorbing a single electron with



energy equal to the energy gap between G and  $E_1$  (i.e., satisfying the resonance condition). The absorption is called ground state absorption (GSA). The long-lived nature of  $E_1$  allows the excited electron to absorb a second photon with the same energy, and the excited electron can be further excited to a higher energy state ( $E_2$ ). The transition is called excited state absorption (ESA). The excited electron finally returns to the ground state and emits a photon simultaneously. The emitted photon has higher energy than the absorbed (or incident) photon. The emission process is referred as radiative relaxation. Monochromatic excitation source can be used if the energy gaps between G and  $E_1$ , and  $E_1$  and  $E_2$  are same. For example, a 980-nm laser diode can be used for Er-doped luminescent materials.

Energy transfer up-conversion (ETU) achieves UC emission with similar principles of ESA process. An electron is excited to  $E_2$  via two absorption processes. Unlike ESA, the excited electron in  $E_1$  (i.e., after GSA) does not absorb a second photon for transiting to  $E_2$ . Instead, it absorbs the energy released from another excited electron of another ion (sensitizer) when it relaxes non-radiatively back to G (Figure 1-7 (b)). The energy transfer process requires the energy gap between G and  $E_1$  of the sensitizer to be matched with that between  $E_1$  and  $E_2$  of the activator. Phonon will be involved if there is minor energy mismatch between the transition pairs [39]. A coulombic overlap between the two electronic systems is required for the occurrence of non-radiative energy transfer through dipole-dipole interactions. The UC efficiency of ETU process depends on the distance-dependent relative overlap of the E-fields of the ion pair, and is usually around two orders of magnitude higher than that of ESA.

Cooperative up-conversion (CUC) is similar to ETU as both sensitizers and activators are involved (Figure 1-7 (c)) [40]. Different from ETU, the activator ion in



CUC does not have a real intermediate energy level. Via GSA, two electrons (from two sensitizers) are excited to  $E_1$ . The excited electrons cooperatively promote to a virtual excited state ( $E_v$ ), then energy transfers from  $E_v$  to activator ions and thus UC emission happens. Yb-doped yttrium aluminum garnet (YAG,  $Y_3Al_5O_3$ ) nanophosphors and Yb<sup>3+</sup> and Er<sup>3+</sup> co-doped  $Al_2O_3$  thin film are examples of the materials that have been reported with CUC mechanism [41], [42].

Photon avalanche (PA) realizes UC emission by achieving a population of electrons by ESA and ETU as shown in Figure 1-7 (d). Four energy levels, G,  $E_1$ ,  $E_2$  and  $E_3$ , are involved in this process. By weak non-resonant GSA, an electron is excited from G to a second metastable excited state ( $E_2$ ). Energy transfer occurs when this electron relaxes to  $E_1$ . It may excite a ground-state electron of the same ion or an adjacent ion to  $E_1$  through ion-pair relaxation energy transfer [43]. Excitation of an electron from  $E_1$  to  $E_3$  is achieved by incident radiation whose energy matches with the energy gap between  $E_1$  and  $E_3$ . When the electron relaxes non-radiatively from  $E_3$  to  $E_1$ , ion-pair relaxation occurs and leads to the excitation of two electrons from G to  $E_1$ . These two electrons will be further excited to  $E_3$  by the incident radiation. As this process occurs continuously, the population of the  $E_3$  state increases exponentially. At last, electrons relax radiatively to G and thus UC emission is resulted. Three non-linear behaviors: transmission, emission and pump power-dependent rise-time, can be used to identify the PA process [43], [44].

Energy migration up-conversion (EMU) can be adopted to achieve tunable UC emissions by varying the gadolinium (Gd) content through core-shell structure [45]. As illustrated in Figure 1-7 (e), four types of lanthanide ions are involved in the process: sensitizer (Type I), accumulator (Type II), migrator (Type III) and activator (Type IV). Type I and II ions locate at the core, Type III ion locates in the core and shell, while Type



IV ion locates in the shell. Though GSA, electron of Type I ion is excited to  $E_1$  state by the incident radiation. Via energy transfer, the electron of Type II ions is excited to high-lying excited state ( $E_H$ ). The metastable excited state ( $E_i$ ) of Type II ion is required to be long-lived for achieving UC emission as it needs to harvest at least two photons from Type I ion. Therefore, typical RE ions such as  $\text{Ho}^{3+}$ ,  $\text{Tm}^{3+}$  and  $\text{Er}^{3+}$  ions are often chosen as Type II ion. The energy stored in Type II ion transfers to Type III ion, and then the excitation energy migrates within the sub-lattices of Type III ions through the core-shell interface. Finally, UC emission occurs when the energy is transferred to the Type IV ion.

### **1.5. Down-conversion process**

Down-conversion (DC) process involves the absorption of a photon with frequency  $\nu$  by a nonlinear medium and simultaneous emission of photons with frequencies  $\nu_i$ , where  $\nu \geq \sum \nu_i$ . This process is also known as parametric down-conversion. The parametric gain in the nonlinear material determines the efficiency of the DC process. Furthermore, the parametric gain is dependent on (1) the power of incident radiation, (2) photon frequencies, (3) radiations' indices of refraction in the material, and (4) the nonlinear "hyper-susceptibility" of the material. DC process with an external quantum efficiency (EQE) less than 100% can be denoted as luminescence down-shifting (DS) [46]. EQE is defined as the ratio between the photogenerated charges harvested at the electrodes to the number of incident photons with a specific frequency [47].

**1.6. Rare-earth ions (RE ions)**

Rare-earth (RE) elements have 17 members, which include 15 lanthanides, scandium (Sc) and yttrium (Y) [48]. The 15 lanthanides are lanthanum (La), cerium (Ce), praseodymium (Pr), neodymium (Nd), promethium (Pm), samarium (Sm), europium (Eu), gadolinium (Gd), terbium (Tb), dysprosium (Dy), holmium (Ho), erbium (Er), thulium (Tm), ytterbium (Yb) and lutetium (Lu).

The energy levels of 13 RE ions in  $\text{LaF}_3$  are shown in Figure 1-8, in which their emitting states for visible light, near infrared (IR) and ultraviolet (UV) are marked with red dots. All those energy levels are originated from the 4f configurations which are less dependent on the host material as compared with those from the 5d states [49].

RE elements are often used as dopants for improving the functional properties of ceramic hosts. For example, via substituting RE elements into the A-sites, the leakage current of  $\text{BiFeO}_3$  is reduced while its magnetoelectric effect is enhanced owing to the suppression of the magnetic spin cycloid [50]. The doping has also led to a structural phase transition of BFO. The doping of RE elements can effectively enhance the microstructure and phase structure of  $\text{Ba}_x\text{Sr}_{1-x}\text{TiO}_3$ -based barium boroaluminosilicate (BST-BBAS) glass-ceramics [51]. RE-doped phosphors are widely used for optical temperature sensing applications. Comparing with traditional sensors, RE-doped phosphors is more sensitive, free from electromagnetic interference, compatible with electronic device, and able to do long path monitoring [52]. The co-doping of large RE elements (La, Nd and Sm) and small RE elements (such as Gd, Dy, Er and Y) can enhance the thermoelectric properties of  $\text{SrTiO}_3$  [53].

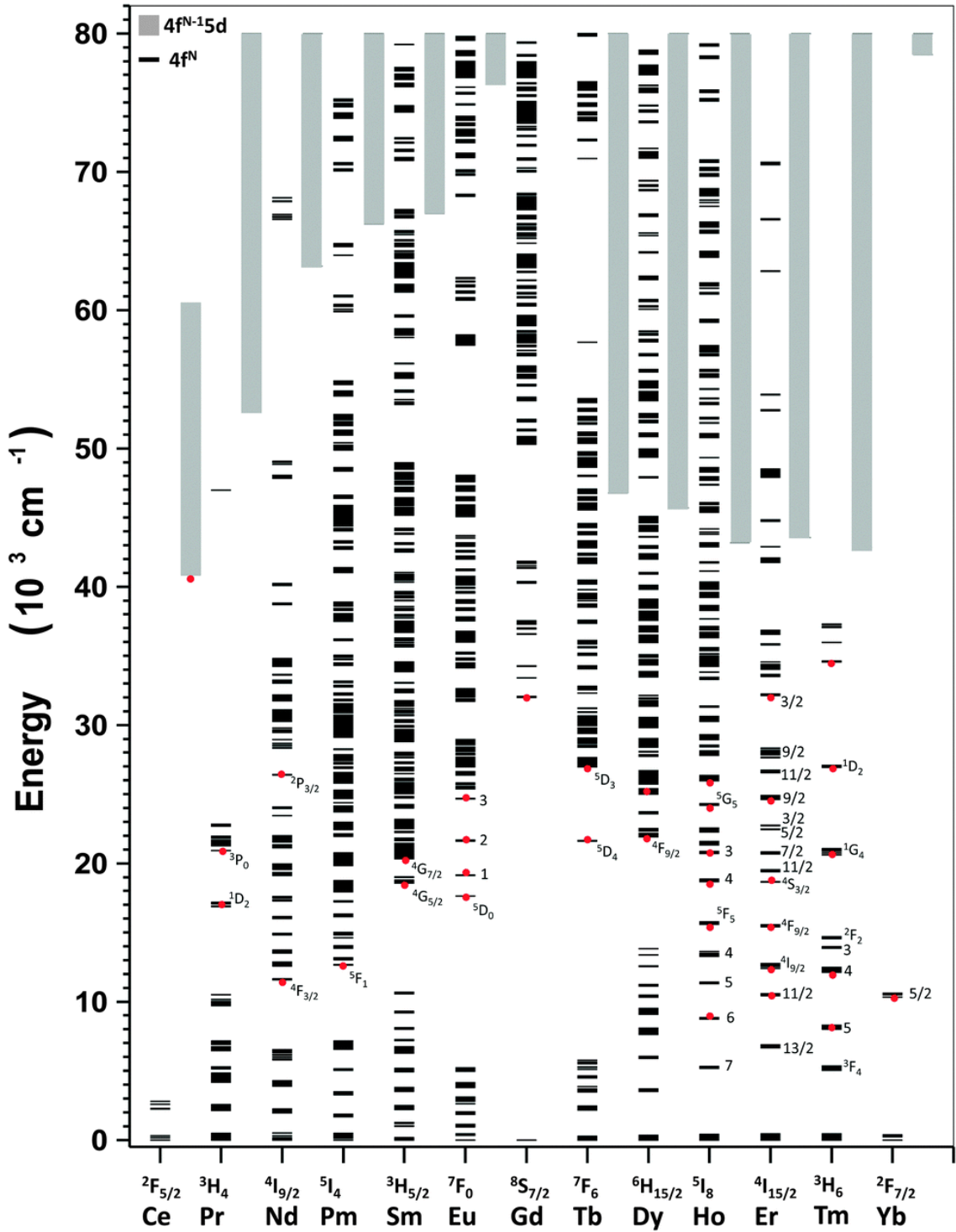


FIGURE 1-8 Energy levels of trivalent rare-earth ion in LaF<sub>3</sub> with anticipated emitting states in the visible, near IR and UV region marked with red dots [49].

**1.6.1. Dysprosium ion ( $\text{Dy}^{3+}$  ion)**

$\text{Dy}^{3+}$  ion is one of the lanthanides ions, which has been widely used for optical applications owing to its luminescent properties.  $\text{Dy}^{3+}$  ion exhibits yellow and blue emissions at 570-600 nm ( ${}^4\text{F}_{9/2} \rightarrow {}^6\text{H}_{13/2}$ ) and 470-500 nm ( ${}^4\text{F}_{9/2} \rightarrow {}^6\text{H}_{15/2}$ ), respectively (Figure 1-9) [54]. The ratio of PL intensities of the two emissions is dependent on the host composition and the concentration of  $\text{Dy}^{3+}$  ions. It has then been used for doping various glasses and phosphors to produce white light [54]–[56]. Owing to the lacking of red emission, the emitted white light belongs to cold white light [57]. For decreasing the color temperatures,  $\text{Eu}^{3+}$  is usually co-doped with  $\text{Dy}^{3+}$  for providing red emissions [57]–[60].

$\text{Dy}^{3+}$  ion can also improve the dielectric properties of BZT ceramics. e.g., BZT-0.15 and BZT-0.2 [16], [61]. Owing to the high dielectric constants, BZT ceramics are often used to fabricate multilayer capacitors. Via substituting into the cation sites, the dielectric properties of BZT ceramics can be improved and the lifespan of the fabricated capacitors can be prolonged. Because of the smaller size as compared with  $\text{Ba}^{2+}$  ion, a core-shell structure is achieved and thus the dielectric properties are improved [62], [63]

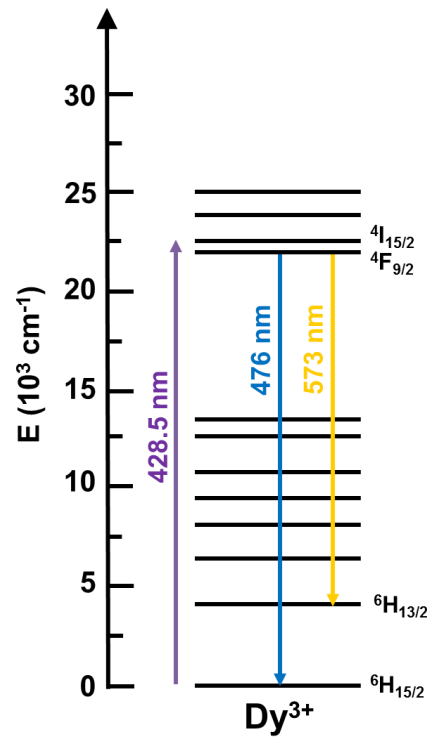


FIGURE 1-9 Energy levels diagram of Dy<sup>3+</sup>.

### 1.6.2. Erbium ion (Er<sup>3+</sup> ion)

Er<sup>3+</sup> ion exhibits luminescence of both Stokes (down-conversion) and anti-Stokes (up-conversion) types [64]. As shown in Figure 1-10, electrons can be excited from the  $4I_{15/2}$  ground state to the  $4I_{11/2}$  level or  $4F_{7/2}$  level via absorbing 980-nm or 488.5-nm photons, respectively, which are commonly provided by commercially available lasers or xenon lamps. For realizing the up-conversion emission, electrons at the  $4I_{11/2}$  level are further excited to the  $4F_{7/2}$  levels by the 980-nm photons. For both types of emissions, electrons at the  $4F_{7/2}$  level relax non-radioactively to the  $2H_{11/2}$ ,  $4S_{3/2}$  and  $4F_{9/2}$  levels through multiphonon relaxation (MPR); and then radioactively to the ground state  $4I_{15/2}$ . Accordingly, the wavelength of the typical emissions of Er<sup>3+</sup> are in the range of 500-530

nm ( ${}^2H_{11/2} \rightarrow {}^4I_{15/2}$ , green), 530-570 nm ( ${}^4S_{3/2} \rightarrow {}^4I_{15/2}$ , green) and 650-660 nm ( ${}^4F_{9/2} \rightarrow {}^4I_{15/2}$ , red).

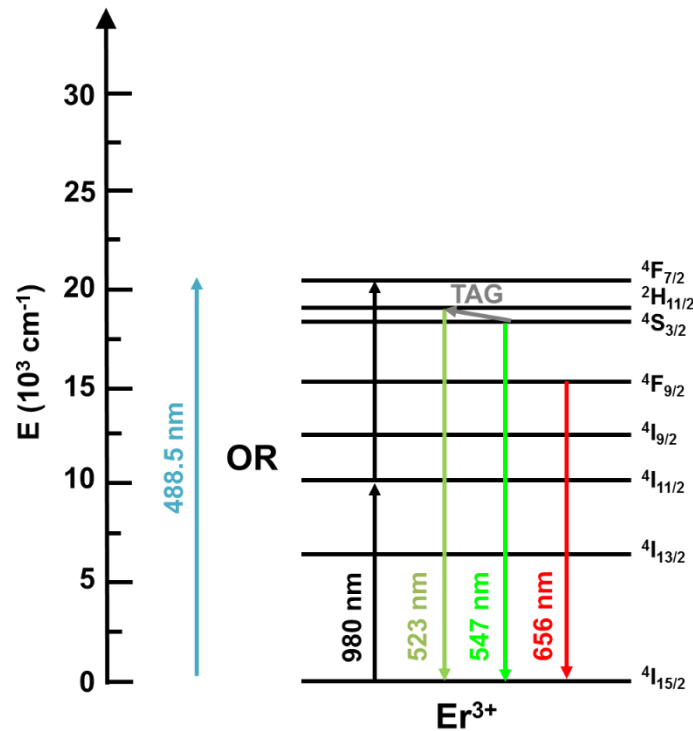


FIGURE 1-10 Energy levels diagram of  $Er^{3+}$ .

Because of the similar energies, the  ${}^4S_{3/2}$  and  ${}^2H_{11/2}$  levels are considered as a pair of thermally coupled emission levels [64]. By thermal agitation (TAG), electrons at the  ${}^4S_{3/2}$  level can be excited to the  ${}^2H_{11/2}$  level. At high temperatures, more electrons are excited and then the emission at 523 nm will become stronger and that at 547 nm becomes weaker. As a result, the thermally coupled emission levels allow Er-doped materials to be applied for optical temperature sensing. Based on the fluorescence intensity ratio (FIR) of the two green emissions, optical temperature sensors are developed. The FIR is defined as [64], [65],



$$\begin{aligned} FIR &= \frac{I_{523}}{I_{547}} = \frac{N(^2H_{11/2})}{N(^4S_{3/2})} \\ &= \frac{c_1(\nu)A_1g_1h\nu_1\beta_1}{c_2(\nu)A_2g_2h\nu_2\beta_2} \exp\left(\frac{-\Delta E}{kT}\right) = C \exp\left(\frac{-\Delta E_{12}}{kT}\right) \end{aligned} \quad (1.2)$$

where  $I_{523}$  and  $I_{547}$  are the integrated fluorescence intensities,  $N$  is the population number,  $c_i(\nu)$  is the response rate,  $A_i$  is the spontaneous radiative rate from the corresponding excited level to the ground state,  $g_i$  is the degeneracy,  $h\nu_i$  is the energy of the emitted photons,  $\beta_i$  is the branching ratio,  $\Delta E_{12}$  is the band gap between the two levels,  $k$  is the Boltzman constant, and  $T$  is temperature. The sensor sensitivity is calculated as,

$$\frac{dR}{dT} = FIR \left( \frac{-\Delta E_{12}}{kT^2} \right). \quad (1.3)$$

The sensors are less dependent on the measurement conditions and have better accuracy and resolution [66], [67].

It has also been shown that the emissions of Er-doped ceramics are sensitive to the crystal symmetry of the host [68], [69]. For Er-doped  $(K_{0.5}Na_{0.5})_{1-x}Li_xNb_{1-x}Bi_xO_3$  ceramics, the PL intensity ratio of the red and green emissions ( $I_{red}/I_{green}$ ) becomes the highest for the ceramic having a cubic phase (i.e., at  $x = 0.7$ ). For Er-doped  $Pb(Mg_{1/3}Nb_{2/3})O_3$ - $PbTiO_3$  ceramics, the PL intensity ratio of the red and green emissions  $I_{red}/I_{green}$  is affected by the phase change of the ceramic host. In general, the intensity ratio increases with higher structural symmetry.

### 1.6.3. Europium ion ( $Eu^{3+}$ ion)

$Eu^{3+}$  ion is one of the most emissive RE ions which has an electronic configuration of  $[Xe]4f^6$  [70]. As shown in Figure 1-11,  $^7F_0$  is the ground state of  $Eu^{3+}$  and  $^5D_0$  is the long-lived excited states. The most intense emission bands located at 596 and 615 nm are attributed to the transitions  $^5D_0 \rightarrow ^7F_1$  and  $^5D_0 \rightarrow ^7F_2$ , respectively. The emission at 596



nm is often used as a probe of chiral structures as it satisfies the magnetic dipole selection rules ( $\Delta J = 0, \pm 1$  except  $0 \leftrightarrow 0$ ) [71]. On the other hand, the emission at 615 nm is highly sensitive to chemical environment so it is described as “hypersensitive”.

The co-doping of  $\text{Eu}^{3+}$  and  $\text{Dy}^{3+}$  ions in potassium calcium borate  $\text{KCaBO}_3$  phosphors gives intense white light emission. The emission intensity is strongly dependent on the concentration of  $\text{Dy}^{3+}$ , which is due to the inter-ion energy transfers from  $\text{Dy}^{3+}$  to  $\text{Eu}^{3+}$ . Moreover, the doping of  $\text{Eu}^{3+}$  in BZT-0.25 ceramics has also been shown to exhibit thermoluminescence (TL) [72]. The TL glow-curves indicates the activation energy is between 0.25 and 0.4 eV. Similar to other RE elements,  $\text{Eu}^{3+}$ , as a dopant, also has significant effects on the dielectric properties of the ceramic hosts. For example, the Curie temperature of BZT-0.15 ceramics is reduced by  $90^\circ\text{C}$  while the dielectric constant maximum is enhanced from 8300 to 15200 after the doping of 1 wt% Er.

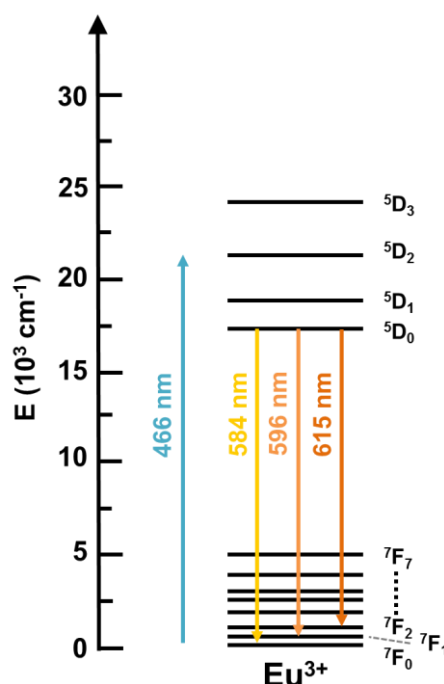


FIGURE 1-11 Energy levels diagram of  $\text{Eu}^{3+}$ .



### 1.7. Tunable photoluminescence properties

Tunable photoluminescence plays an important role in optical applications, such as biological labeling, volumetric 3D displays and long-distance quantum communication [43], [73], [74]. Using external stimuli, fields or chemical reaction, tuning PL can be achieved [75]–[83]. However, there are little works reporting the reversible tuning of PL by external E-field at room temperature.

Recently, it has been reported that in-situ reversible tuning of PL response can be realized in  $\text{Ba}_{0.85}\text{Ca}_{0.15}\text{Ti}_{0.9}\text{Zr}_{0.1}\text{O}_3$  ceramics doped with 0.2 mol% Pr (abbreviated as BCTZ:Pr) using an external E-field [78]. Figure 1-12 (a) shows the XRD patterns of the ceramics under an E-field switching between 0 and 2 kV/mm sinusoidally for three cycles. It can be seen that the crystal phase changes under an E-field but fails to restore after the first two cycles of E-field. As evidenced by the temperature-dependent dielectric properties (Figure 1-13), the E-field induces an irreversible phase change from the mostly tetragonal to rhombohedral phase, which leads to an irreversible variation of PL in the first three cycles of E-field (Figure 1-12 (b)). The PL response under the subsequent cycles of E-field is shown in Figure 1-14, in which the XRD patterns under the 5<sup>th</sup> and 10<sup>th</sup> cycle of E-field are shown for illustrating the absence of phase change. It has then been suggested that the reversible PL changes observed in the subsequent cycles of E-field is attributed to polarization switching rather than phase change.

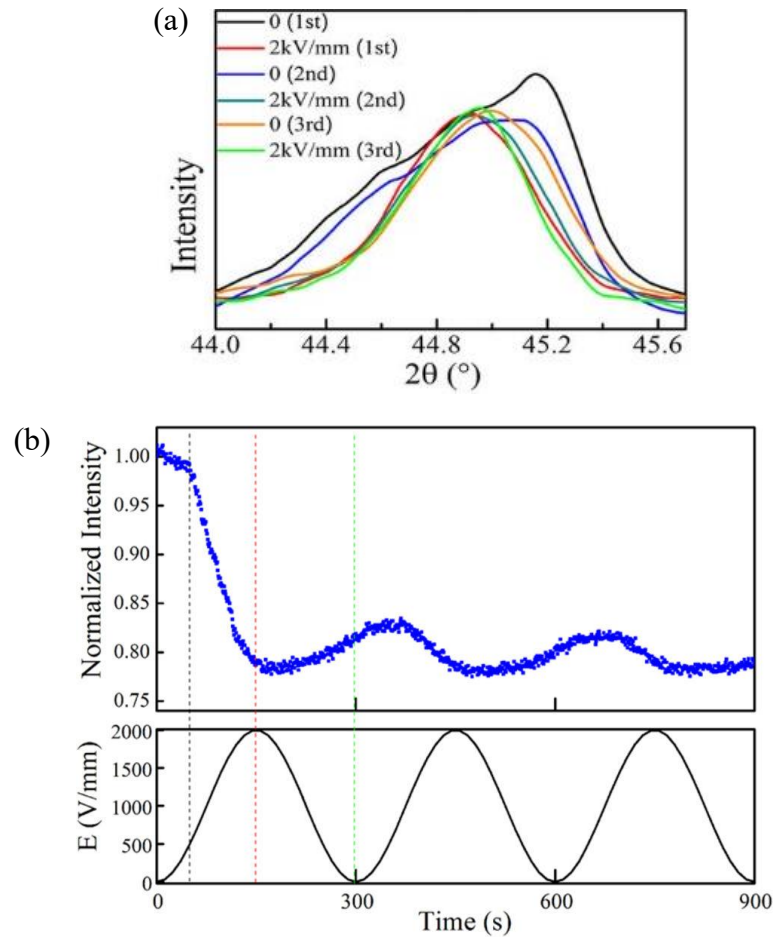


**FIGURE 1-12** (a) The fine scan XRD pattern and (b) PL response under of BCTZ:Pr measured with applying the off and on-field for three cycles [78].

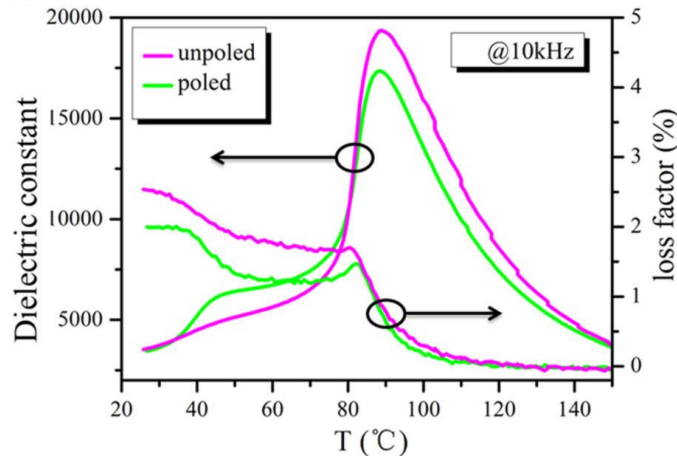


FIGURE 1-13 The temperature dependence dielectric properties measured with poled and unpoled sample [78].

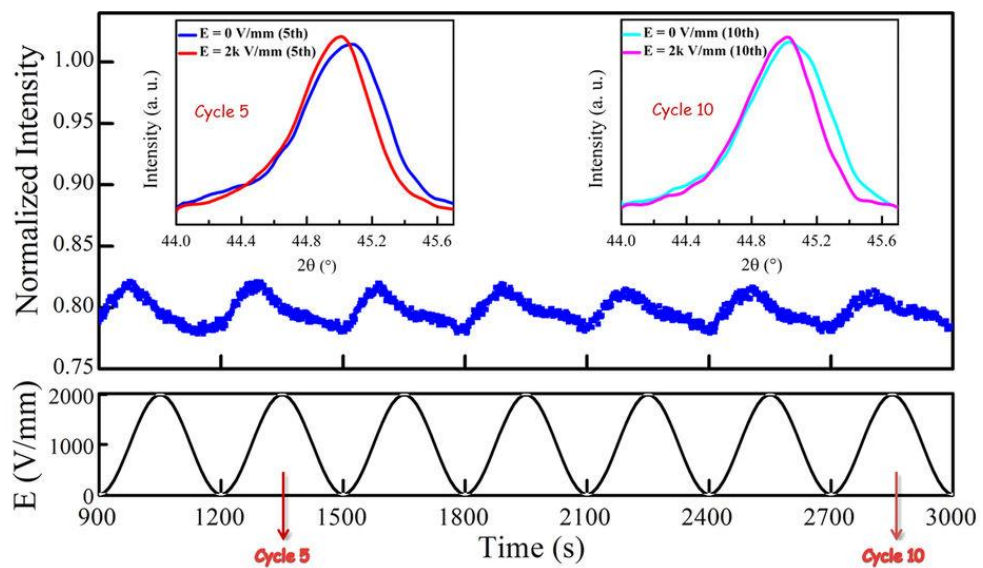


FIGURE 1-14 The PL response under six cycles of E-field and the XRD pattern under 5<sup>th</sup> and 10<sup>th</sup> cycle of E-field [78].



E-field-induced tuning of PL has also been reported for Eu-doped 0.94 (Na<sub>0.5</sub>Bi<sub>0.5</sub>TiO<sub>3</sub>)-0.06(BaTiO<sub>3</sub>) (BNT-6BT) ceramics [80]. The PL spectra of an unpoled and poled sample are shown in Figure 1-15, in which the weak Stark emissions at ~580 nm attributed to the transition  $^5D_0 \rightarrow ^7F_0$  are enlarged in the insets for the ease of observation. Distinct difference in the PL spectra arisen from the poling process (i.e. the application of an external E-field) is observed. The Stark band attributed to the  $^5D_0 \rightarrow ^7F_2$  transition of the unpoled one has only two emission lines at 615 and 625 nm, while the poled sample has three emissions (together with an additional emission line at ~621 nm). The poling process also reduces the relative intensity of the strongest line (~593 nm) of the emission band attributed to the  $^5D_0 \rightarrow ^7F_1$  transition. XRD results reveal a phase transition from the cubic to rhombohedral phase induced by the poling process. It is suggested that the change in the observed PL responses is due to the phase transition. Also, the depoled sample, which changes back to the paraelectric cubic phase, exhibits almost the same PL spectrum as the unpoled one. As shown in Figure 1-16, a new Stark line (shown by an arrow) appears under an E-field and disappear upon removal of the E-field at 80°C. Accordingly, the E-field-induced PL response is reversible at high temperatures close to the depolarization temperature (~85°C). It is then anticipated that if the depolarization temperature is lowered to room temperature, the PL response can be tuned by an E-field in a reversible manner at room temperature.

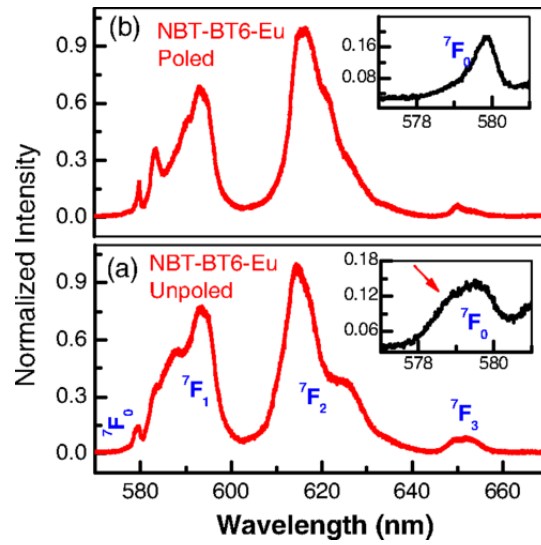


FIGURE 1-15 PL spectra measured with (a) unpoled and (b) poled BNT-6BT: Eu specimens. The insets are the magnified of the  $^5D_0 \rightarrow ^7F_0$  Stark line [80].

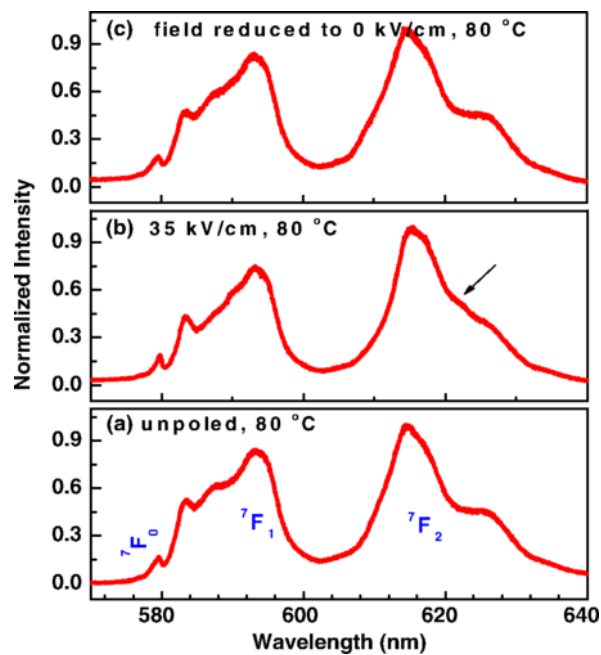
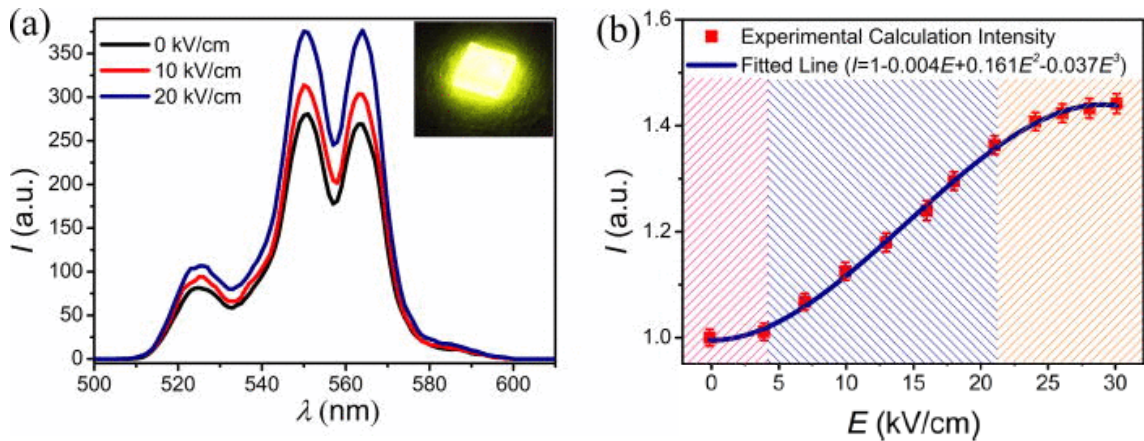
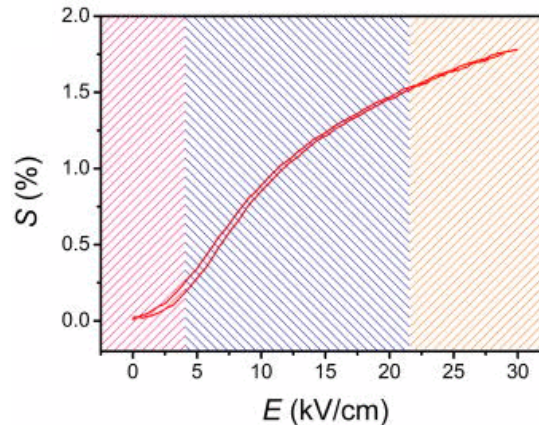


FIGURE 1-16 PL spectrum of (a) unpoled sample, (b) sample under an E-field of 3.5 kV/mm and (c) sample after removal of field measured at 80°C [80].

Liang et al. have also reported an E-field-induced tuning of PL response for Er-doped  $0.75\text{Pb}(\text{Mg}_{1/3}\text{Nb}_{2/3})\text{O}_3\text{-}0.25\text{PbTiO}_3$  (PMN-PT) ferroelectric ceramics [81]. Unlike other works, up-conversion PL emissions of the ceramics are studied. As shown in Figure 1-17 (a), the PL intensity increases by about 40% under an E-field of 20 kV/cm. This is attributed to the strains induced by the E-field, which lowers the crystal symmetry and then enhance the PL emission [84]. As shown in Figure 1-17 (b), the PL intensity increases rapidly as the E-field increases from 4 to 21 kV/cm and then becomes saturated. The authors claimed that the PL intensity decreases as the E-field decreases slowly to zero, and thus the E-field-induced variation of PL is reversible. As supported by similar behavior of the E-field-induced strain (Figure 1-18), they deduced that the strain induced by E-field leads to the deformation of crystal structure and then enhances the emission intensity.



**FIGURE 1-17** (a) Emission spectrum of Er-doped PMN-PT ceramics under different strengths of E-field and inserted photo of actual fluorescence; (b) the integrated intensity of emission against the bias E-field graph [81].



**FIGURE 1-18** Monopolar E-field-induced strain (SE) loop of Er-doped PMN-PT ceramics measured at room temperature [81].

## 1.8. Motivation of research

Tunable PL property allows numerous optical applications and application of E-field has been reported as possible way to tune PL properties. It is assumed that turning PL at room temperature by E-field might be possible when the transition temperature  $T_m$  (i.e., the temperature at which the dielectric constant becomes maximum) of the sample is close to room temperature. Therefore, the present work aims at developing new lead-free RE-doped BZT-based ceramics with tunable PL properties under E-field at room temperature by reducing their  $T_m$ . BZT is a lead-free ferroelectric ceramic with high tunability, great dielectric, ferroelectric and piezoelectric properties. Moreover, its  $T_m$  depends on the Zr content. Therefore, BZT ceramics with different Zr contents will be first fabricated by solid-state reaction for choosing the suitable host to achieve the objective. Then, three RE ions,  $Dy^{3+}$ ,  $Er^{3+}$  and  $Eu^{3+}$ , will be doped into the BZT ceramics and act as activators. Transparent electrode will be deposited on the RE-doped BZT ceramics for observing the PL responses under E-field. Also, the effect of RE dopants on the dielectric, ferroelectric and piezoelectric properties will be investigated.



### 1.9. Scope of work

The main objective of the project is to develop lead-free ferroelectric ceramics with tunable PL response under dc E-field at room temperature. This report contains six chapters.

Chapter 1 gives a brief overview of ferroelectric materials, luminescence, RE ions, tunable PL properties and objectives of the project.

Chapter 2 presents the fabrication procedures, which include the conventional solid-state reaction and preparation of transparent electrode. Also, it contains characterization procedures such as XRD, SEM, dielectric, ferroelectric, piezoelectric and PL measurements.

Chapter 3 reports the characterization and discussion of BZT ceramics.

Chapter 4 includes the characterization and discussion of RE-doped BZT ceramics.

Chapter 5 presents and discusses PL responses under E-field of RE-doped BZT ceramics.

Chapter 6 gives the conclusions.



## Chapter 2 Sample Fabrication and Characterization

### 2.1. Fabrication procedure of the ceramics

$\text{BaZr}_x\text{T}_{1-x}\text{iO}_3$  (abbreviated as BZT-x) and  $\text{BaZr}_x\text{T}_{1-x}\text{iO}_3 + 0.2 \text{ mol\% RE}^{3+}$  (abbreviated as BZT-x-RE) ceramics were prepared by a conventional solid-state reaction method using high-purity metal oxides or carbonate powders:  $\text{BaCO}_3$  (99.5%),  $\text{ZrO}_2$  (99.9%),  $\text{TiO}_2$  (99.9%),  $\text{Dy}_2\text{O}_3$  (99.99%),  $\text{Er}_2\text{O}_3$  (99.99%) and  $\text{Eu}_2\text{O}_3$  (99.99%). BZT-x ceramics with  $x = 0.15, 0.2, 0.25$  and  $0.3$  were prepared. Three RE ions have been chosen as dopants, which are  $\text{Dy}^{3+}$ ,  $\text{Er}^{3+}$  and  $\text{Eu}^{3+}$ . BZT-x-Dy ceramics with  $x = 0.15$  and  $0.2$ , BZT-x-Er ceramics with  $x = 0.1, 0.15$  and  $0.2$ , BZT-x-Eu ceramics with  $x = 0.15, 0.175$  and  $0.2$  were prepared. The powders in the stoichiometric ratio of the compositions were mixed thoroughly in ethanol using zirconia balls for 8 h, and then dried and calcined at  $1150\text{-}1200^\circ\text{C}$  for 4 h. After the calcination, the mixture was ball-milled again for 8 h. After drying, it was mixed thoroughly with a 5-wt% poly(vinyl alcohol) binder solution and then uniaxially pressed into disc samples with an area of  $1.13 \text{ cm}^2$  under  $\sim 300 \text{ MPa}$  of pressure. After burning out the binder at  $800^\circ\text{C}$  for 2 h, the disk samples were sintered at  $1470\text{-}1580^\circ\text{C}$  for 4 to 15 h in air. Figure 2-1 displays the flow diagram of the fabrication procedure.

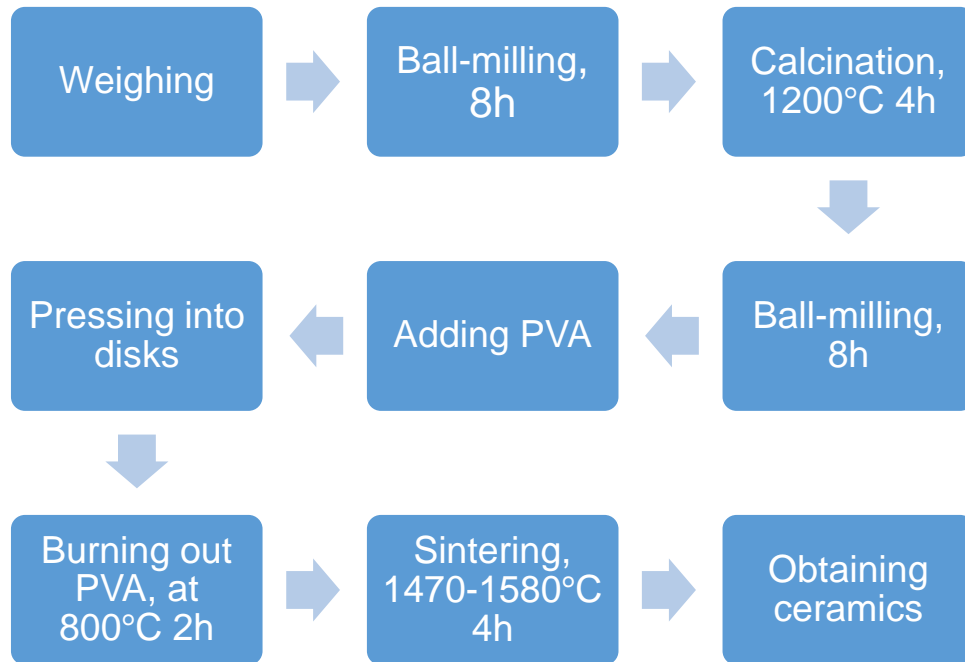


FIGURE 2-1 Flow diagram of the fabrication procedure.

## 2.2. Characterization procedure

### 2.2.1. Crystalline structure

X-ray diffraction (XRD) was used to identify the crystalline structure of the samples. In this study, the ceramics powders were examined using XRD analysis with  $\text{CuK}\alpha$  ( $\lambda = 0.154 \text{ nm}$ ) radiation (SmartLab; Rigaku Co., Japan).

As shown in Figure 2-2, the X-ray interacts with the crystal lattices of the samples and so scattering happens. The X-rays scattered from each crystalline plane interfere with each other, resulting in constructive or destructive interferences and thus a variation of intensity called XRD pattern. According to Bragg's Law, the intensity (of the scattered X-rays) reaches a maximum when the incident (or diffraction) angle  $\theta$  satisfies:

$$2d_{hkl} \sin \theta = k\lambda \quad (2.1)$$

where  $h, k, l$  are the Miller indices,  $d_{hkl}$  is the interplanar spacing of  $\{hkl\}$  set of lattice planes,  $k$  is the order of diffraction, and  $\lambda$  is the wavelength of the X-ray.

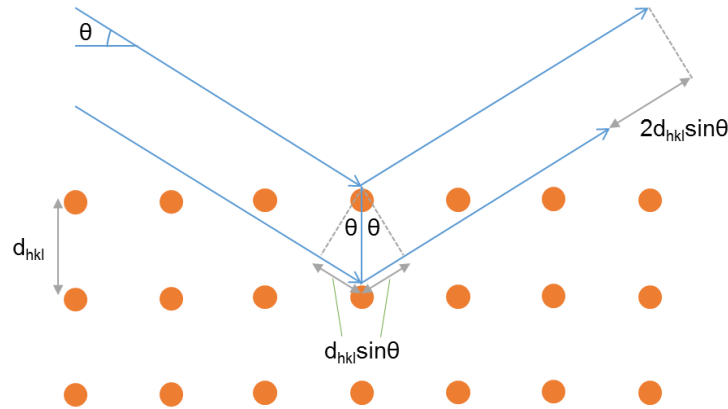


FIGURE 2-2 The schematic diagram of X-ray diffraction in crystal.

The in-situ XRD pattern of ceramic was also observed under an external electric field (E-field). This measurement can verify the effect of E-field on the lattice and phase of the ceramic. A voltage sourcemeter (Model 2410; Keithley Instruments Inc., USA) was used to apply E-fields. The ceramic sample was deposited with transparent electrode and the detailed procedures of deposition will be revealed in the later section (Section 2.2.6.2).

### 2.2.2. Microstructure

The microstructures of the ceramic samples were examined using a field-emission scanning electron microscope (FE-SEM) (JSM-6335F, JEOL Ltd., Japan). Before the examination, the sample surfaces were coated with platinum for conducting away the incident electrons and thus forming the FE-SEM images. A coating system (Model 682, Gatan Inc., USA) was used for depositing a thin layer of platinum on the sample surfaces in argon atmosphere at high vacuum ( $10^{-4}$  Pa).

The FE-SEM is operated at a high vacuum. For imaging, a beam of accelerated electrons is emitted from an electron gun, passes through a series of lens, and then scans across the surface of the samples by means of scan coils. A high voltage is applied for

accelerating the electrons. The electrons lose energy when they are incident on the samples due to random scattering and absorption. This energy exchange causes the reflection of high-energy electrons by elastic scattering, the emission of secondary electrons by inelastic scattering, and the emission of characteristic X-rays. The secondary electrons can be detected by a suitably-positioned detector for imaging. Figure 2-3 shows the schematic diagram of a FE-SEM.

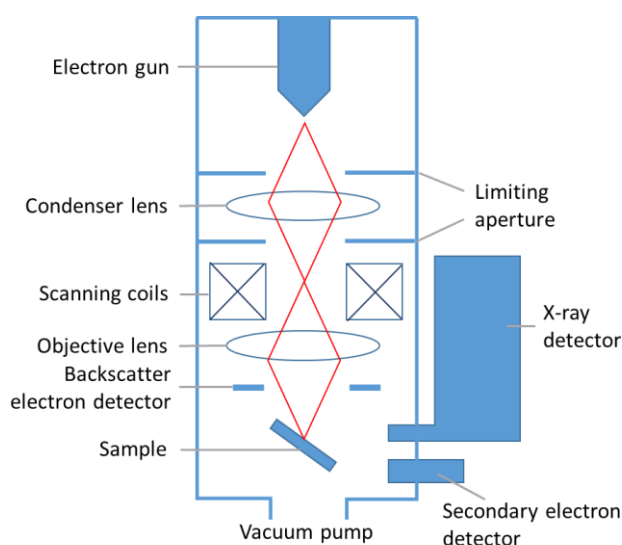


**FIGURE 2-3** The schematic diagram of a FE-SEM.

### 2.2.3. Dielectric properties

The ceramic samples were grinded to obtain a flat surface. Subsequently, silver electrodes were fired on both surfaces at 750°C for 30 min for the measurements of dielectric constant and dielectric loss.

**2.2.3.1. Dielectric constant and dielectric loss**

Dielectric properties of the samples were measured using an impedance analyzer (HP 4294A; Agilent Technologies Inc., USA). Both dielectric constant and dielectric loss were measured at 1 kHz at room temperature. The dielectric constant ( $\epsilon_r$ ), which is also known as relative permittivity, was calculated from:

$$C = \frac{\epsilon_0 \epsilon_r A}{d} \quad (2.2)$$

where C is the capacitance,  $\epsilon_0$  is the permittivity of vacuum, A is the electrode area of the sample, and d is the thickness of sample.  $\epsilon_r$  can be expressed as  $\epsilon_r = \epsilon' + i\epsilon''$ , where  $\epsilon'$  and  $i\epsilon''$  are the real and imaginary part of  $\epsilon_r$  respectively. Dielectric loss ( $\tan \delta$ ) can indicate the quality of the ceramics for practical use. The dielectric loss is calculated as follows:

$$\tan \delta = \frac{\epsilon''}{\epsilon'} \quad (2.3)$$

**2.2.3.2. Temperature dependence of dielectric properties**

For investigating the temperature dependence of dielectric properties, the ceramic samples connected to the impedance analyzer (HP 4194A; Agilent Technologies Inc., USA) was placed inside a tube furnace, in which the temperature was varied from 25 to 120°C at a rate of 0.5°C/min. A thermocouple, connected to a multimeter (Model 2000, Keithley Instruments Inc., USA), was used to measure the temperature close to the sample. The temperature, dielectric loss and capacitance were collected and analyzed by a computer. The schematic diagram of the setup is illustrated in Figure 2-4.

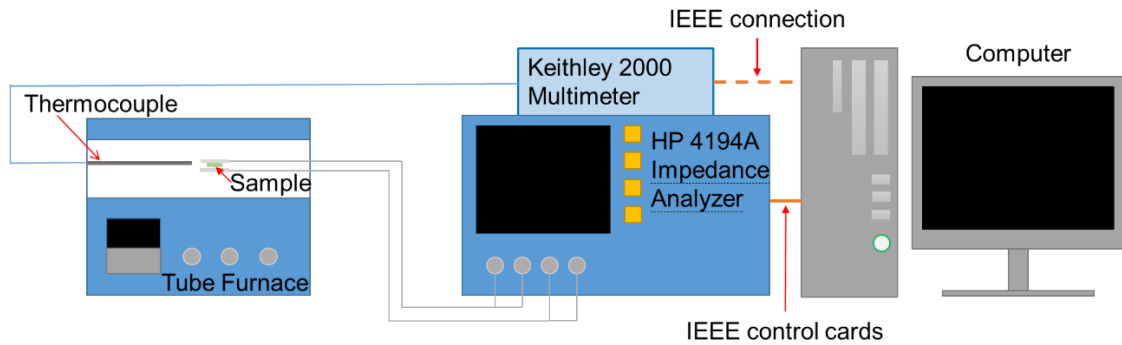


**FIGURE 2-4** The schematic diagram of temperature dependence dielectric measurement setup.

### 2.2.4. Ferroelectric properties

Polarization-electric field (PE) hysteresis loops were measured to verify the relationship between the applied E-field and net polarization. As-prepared ceramic samples with silver electrodes were used for the PE loop measurement. Ferroelectric parameters such as saturation polarization ( $P_{sat}$ ), remnant polarization ( $P_r$ ) and electric coercive field ( $E_c$ ) as illustrated in Figure 2-5 were determined from the PE loop.

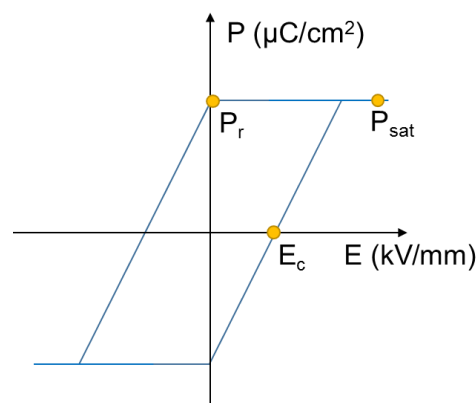


**FIGURE 2-5** PE loop with ferroelectric parameters marked on it.

The PE loops were measured with a modified Sawyer-Tower circuit at 50 Hz. As shown in Figure 2-6, the setup included a digital oscilloscope (DSO) (HP 54645A, Agilent Technologies Inc., USA), an amplifier (Model 609D-6, Trek Inc, USA), a function generator (HP 8116A, Agilent Technologies Inc., USA), a computer and a modified Sawyer-Tower circuit. The Sawyer-Tower circuit contained two capacitors: ferroelectric capacitor ( $C_F$ ) of the ceramics sample and reference capacitor ( $C_R = 10 \mu\text{F}$ ). For the ease of calculation, the value of  $C_R$  was required to be over 1000 times larger than that of  $C_F$  such that the voltage drop across  $C_R$  could be neglected. The sample was immersed in a silicone oil bath for preventing electrical breakdown. An AC voltage signal was produced by the function generator and then amplified 2000 times by the high voltage amplifier before applying on the sample. The input voltage ( $V_i$ ) applied to the sample and the output voltage ( $V_o$ ) across  $C_R$  were measured with the digital oscilloscope. The data were recorded by a computer, and the polarization ( $P$ ) was given as:

$$P = \frac{C_R V_o}{A} \tag{2.4}$$

where  $A$  is the area of electrode.

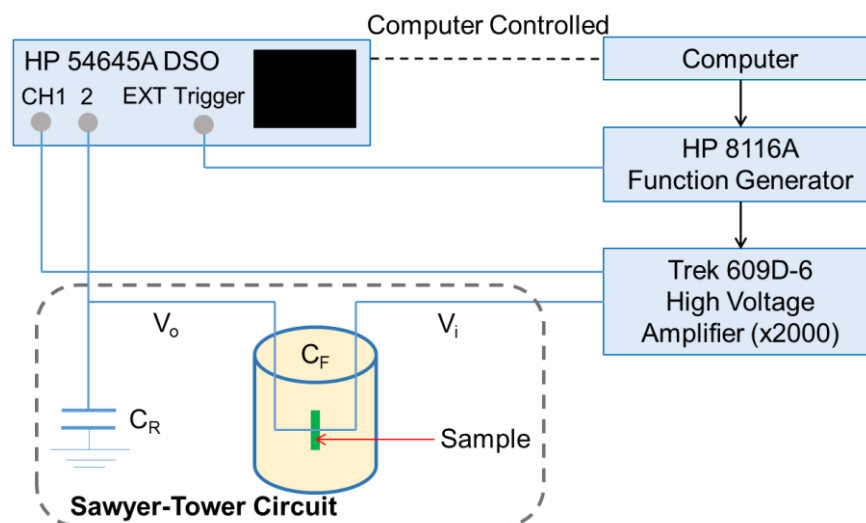


FIGURE 2-6 The schematic diagram of PE loop measurement setup.

### 2.2.5. Piezoelectric properties

Before the measurements, the ceramic samples with silver electrodes on both the top and bottom surfaces were poled under a dc E-field of 2 kV/mm at room temperature in a silicone oil bath for 30 min. The schematic diagram of the poling setup is shown in Figure 2-7. A high voltage amplifier (Model P0621, Trek Inc, USA) was used to amplify the voltage provided by the DC voltage source by 3000 times. Longitudinal piezoelectric coefficient ( $d_{33}$ ) was measured using a piezo  $d_{33}$  meter (ZJ-3B, Institute of Acoustic Academia Sinica, China). The sample was hold between the two probes of the meter, which generated 50-Hz vibrations to trigger the piezoelectric effect. The resulting surface charges were collected and used for determining the  $d_{33}$  value by the meter.

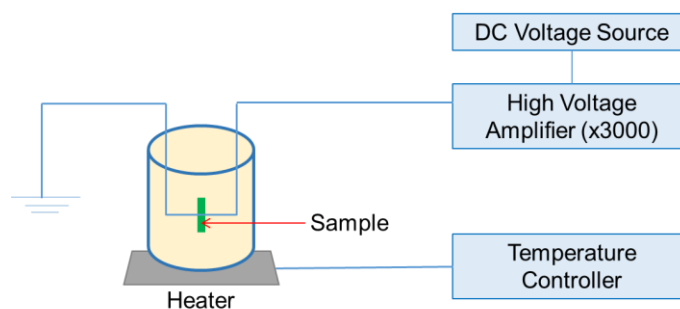
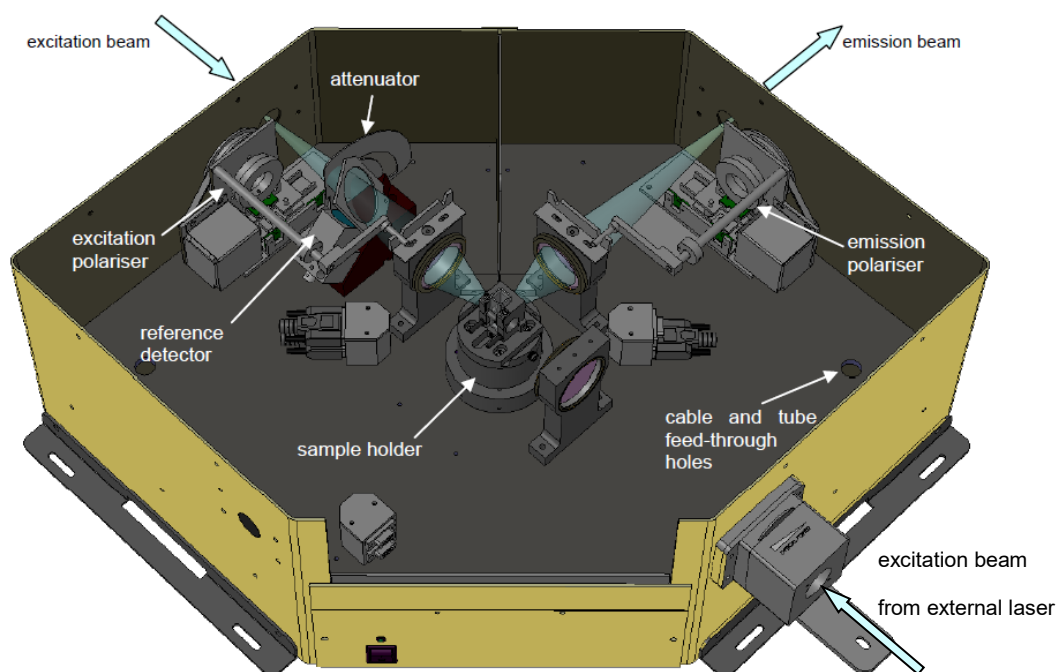


FIGURE 2-7 The schematic diagram of poling setup.

### 2.2.6. Photoluminescence properties

Photoluminescence (PL) properties were measured by a PL spectrometer (FLSP920, Edinburgh Instruments, UK). A xenon arc lamp (Xe900), at 450-W steady state, was used as an excitation source for investigating visible down-conversion emissions. For measuring visible up-conversion emissions, a continuous 980-nm diode laser (MDL-III, CNI Optoelectronics Tech. Co., China) with a maximum power output of 2W was used as an excitation source. The PL spectrum was measured in the range of 200 to 900 nm

using a red sensitive photomultiplier tubes (PMT). For reducing dark noise during the measurement, a Peltier-cooled housing was used to keep the temperature of the PMT at  $-20^{\circ}\text{C}$ . For the lifetime measurements, a microsecond (xenon) flashlamp was used as an excitation source. The 980-nm diode laser was connected with a PM-1 modulator which can provide pulsed excitation for the lifetime measurements. A voltage sourcemeter (Model 2410; Keithley Instruments Inc., USA) was used to apply E-fields in observing in-situ PL responses. The sample chamber of the spectrometer is illustrated in Figure 2-8. The excitation beam on the top left corner was from the xenon lamp while the excitation beam on the bottom right corner was from the laser. The sample holder was then required to rotate when using different light sources. Long-pass filters were inserted in the emission light path for improving the signal to noise ratio.



**FIGURE 2-8** Sample chamber with optional polarizers and laser coupling flange [85].

**2.2.6.1. Temperature dependence of PL properties**

The temperature dependence of PL properties was conducted at the Functional Materials Research Laboratory of Tongji University. The PL spectra were measured with a fluorescence spectrometer (F-7000, Hitachi, Japan). The ceramics samples were heated from room temperature to  $\sim 200^{\circ}\text{C}$  on a heating stage which was controlled by a TP 94 temperature controller (Linkam Scientific Instruments Ltd., Surrey, UK) and was monitored with a Pt-100 thermocouple.

**2.2.6.2. Preparation of transparent electrode**

In order to conduct the PL measurement under an applied E-field, a transparent electrode was deposited on the front surface of the ceramic samples. The transparent electrode allows light incident on the sample for excitation as well as emitting from the samples for detection. The disc sample with the bottom surface coated with silver electrode was first grinded and polished into a thickness of 0.25 mm. An indium tin oxide (ITO) transparent electrode was then deposited on the front surface using a physical vapor deposition method named magnetron sputtering. The sample was heated up to  $300^{\circ}\text{C}$  for better crystallization of ITO. With a gas mixture of oxygen and argon ( $\text{O}_2:\text{Ar} = 1:60$ ), the sputtering was carried out at a pressure of 5 mTorr. Ar plasma was generated by a radio frequency (RF) power supply, and the ITO target was bombarded by the Ar ions. ITO ions were knocked off and attracted to deposit on the sample surface for 40 min. The samples were annealed at  $300^{\circ}\text{C}$  for 1 h and then cooled down to room temperature before the chamber was opened.



## Chapter 3 BZT Ceramics

### 3.1. Introduction

Application of external electric field (E-field) may lead to phase change and then enhance the structural symmetry. Photoluminescence (PL) response has been reported vary with change in structural symmetry [84]. Therefore, tuning PL might be achieved if the transition temperature  $T_m$  (temperature having the dielectric constant maximum) is close to room temperature. This work then aims to develop new lead-free RE-doped barium zirconate titanate (BZT)-based ceramics with tunable PL properties under electric field (E-field) at room temperature via lowering their  $T_m$ . As discussed in Chapter 1, BZT is a lead-free ferroelectric ceramic with high tunability, good dielectric, ferroelectric and piezoelectric properties. In addition,  $T_m$  of BZT is dependent on the Zr content. Therefore,  $BaZr_xTi_{1-x}O_3$  (BZT-x) ferroelectric ceramics with  $x = 0.15, 0.2, 0.25$  and  $0.3$  have been fabricated in this work for determining the suitable host for achieving tuning of PL response. In this chapter, the crystalline structure, microstructure, dielectric, ferroelectric and piezoelectric properties of the BZT-x ceramics have been investigated.

### 3.2. Crystalline structure

The XRD patterns of the BZT-x ceramic powders measured from  $20^\circ$  to  $80^\circ$  are shown in Figure 3-1 (a). All the ceramics have been crystallized in a perovskite structure. The absence of impurity phases (within the resolution limit of XRD equipment) indicates the successfully doping of  $Zr^{4+}$  ions in the B site of the lattices. The peak position of the BZT-0.25 ceramic mostly agrees with JCPDS 36-0019 (BZT-0.25, cubic). However, two diffraction peaks are found at  $45^\circ, 55^\circ, 65^\circ$  and  $75^\circ$  which indicates the sample do not contain cubic phase only. As evidenced by the two diffraction peaks located at  $44-46^\circ$ , all

the ceramics might contain both the cubic and rhombohedral phase (Figure 3-1 (b)). The phase diagram of BZT-x ceramics indicates that the four samples should contain rhombohedral phase and their rhombohedral-cubic transition temperatures are close to room temperature [15]. As also shown in Figure 3-1(b), the diffraction peaks have shifted to small angles with increasing Zr content. It should be due to the larger ionic radius of  $Zr^{4+}$  ion ( $0.72 \text{ \AA}$ , coordination number (CN) = 6) as compared to  $Ti^{4+}$  ion ( $0.605 \text{ \AA}$  ionic radius, CN = 6) and then the expansion of the lattices.

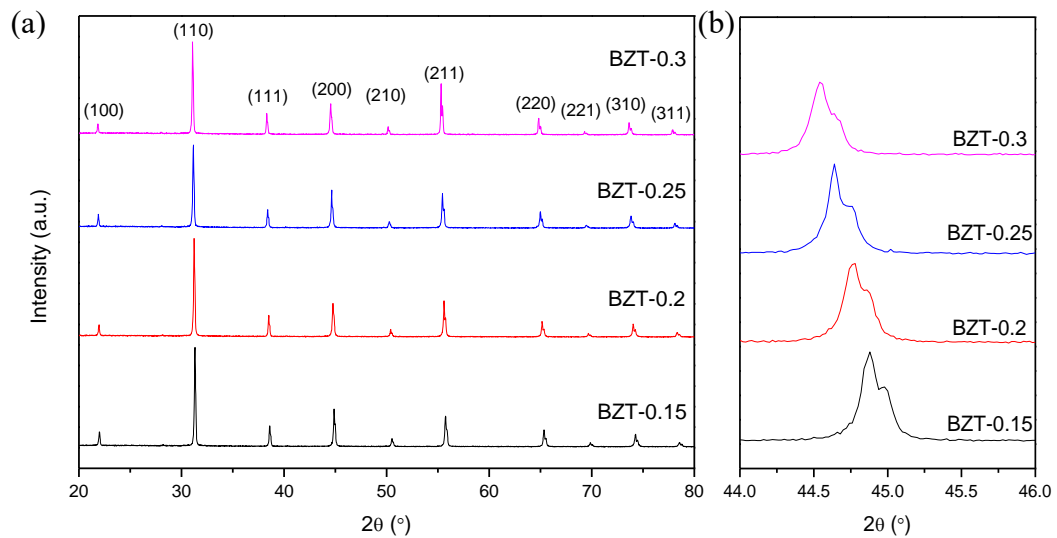
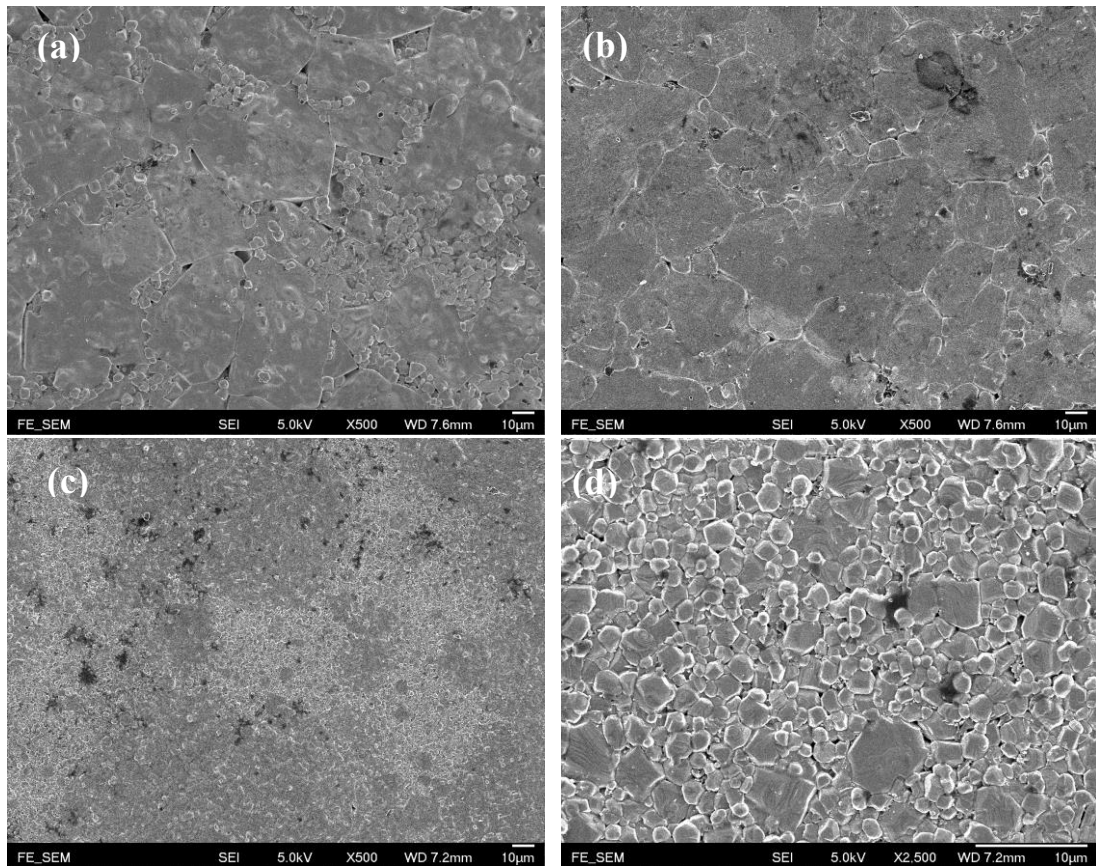


**FIGURE 3-1** The XRD patterns of the BZT-x ceramic powders in the range of (a) 20-80° and (b) 44-46°.



### 3.3. Microstructure

The FE-SEM micrographs of the BZT-x ceramics are shown in Figure 3-2. All the ceramics are dense and have irregular-shaped grains. As illustrated in Table 2, the average grain size of the BZT-0.25 ceramic is about 2.3  $\mu\text{m}$  while the others are much larger, varying in between 30 and 51  $\mu\text{m}$ . This may probably be due to the merging (or melting) of the grains together in those ceramics. Similar morphologies have been observed for the ceramics sintered at lower temperatures. Grain size of BZT-0.2 ceramic has been reported increased from less than 1  $\mu\text{m}$  to 4-6  $\mu\text{m}$  when sintering temperature rise from 1400°C to 1450°C [34].



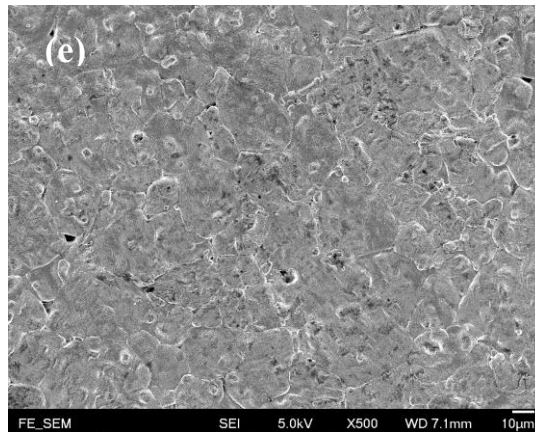


**FIGURE 3-2** FE-SEM micrograph of BZT-x ceramics. (a)  $x = 0.15$ , (b)  $x = 0.2$ , (c) and (d)  $x = 0.25$ , (e)  $x = 0.3$ .

**TABLE 2** Average grain sizes of the BZT-x ceramics

BZT-x	0.15	0.2	0.25	0.3
Sintering temperature (°C)	1570	1470	1520	1500
Grain size (µm)	51.0	45.7	2.3	30.8

### 3.4. Dielectric properties

#### 3.4.1. Dielectric constant and dielectric loss

The observed dielectric constant ( $\epsilon_r$ ) and dielectric loss ( $\tan \delta$ ) of the BZT-x ceramics measured at room temperature and 1 kHz are listed in Table 3. Apparently, both the observed  $\epsilon_r$  and  $\tan \delta$  increase and then decrease with increasing  $x$  (the Zr content), giving maximum values of 12700 and 2.1%, respectively at  $x = 0.2$ . However, the observed variations of  $\epsilon_r$  and  $\tan \delta$  at room temperature should be mainly affected by the phase transitions, which will be discussed in the following section. Nevertheless, all the ceramics have a low dielectric loss ( $< 3\%$ ), corroborating the observed dense structure as shown in Figure 3-2.



**TABLE 3** The dielectric constant ( $\epsilon_r$ ) and dielectric loss ( $\tan \delta$ ) of BZT-x ceramics measured at room temperature and 1 kHz

BZT-x	$\epsilon_r$	$\tan \delta$ (%)
0.15	3000	1.8
0.2	12700	2.1
0.25	10400	0.7
0.3	4300	0.4

### 3.4.2. Temperature dependence of dielectric properties

The temperature dependences of  $\epsilon_r$  and  $\tan \delta$  for the BZT-x ceramics measured at 1 kHz, 10 kHz, 100 kHz and 1 MHz are shown in Figure 3-3. A slightly broadened and frequency-dependent phase transition peak is observed at 64°C for the BZT-0.15 ceramic, confirming its relaxor-like characteristics. At  $x = 0.2$ , the transition peak shifts towards room temperature ( $T_m = 37^\circ\text{C}$ ) with slightly increases in the width and the frequency-dependence of the peak. Although no transition peaks have been observed for the ceramics with  $x = 0.25$  and 0.3 owing to the limitation of our measurements, they should most likely locate below room temperature as indicated by the decreasing trend of  $\epsilon_r$  at high temperatures. This is consistent with the previous results that the  $T_m$  of BZT decreases with increasing Zr content [15]–[18]. As shown in Figure 3-3, the values of the room-temperature  $\epsilon_r$  and  $\tan \delta$  are strongly dependent on their positions at the transition peak. The closer to the transition peak, the higher value they will have.

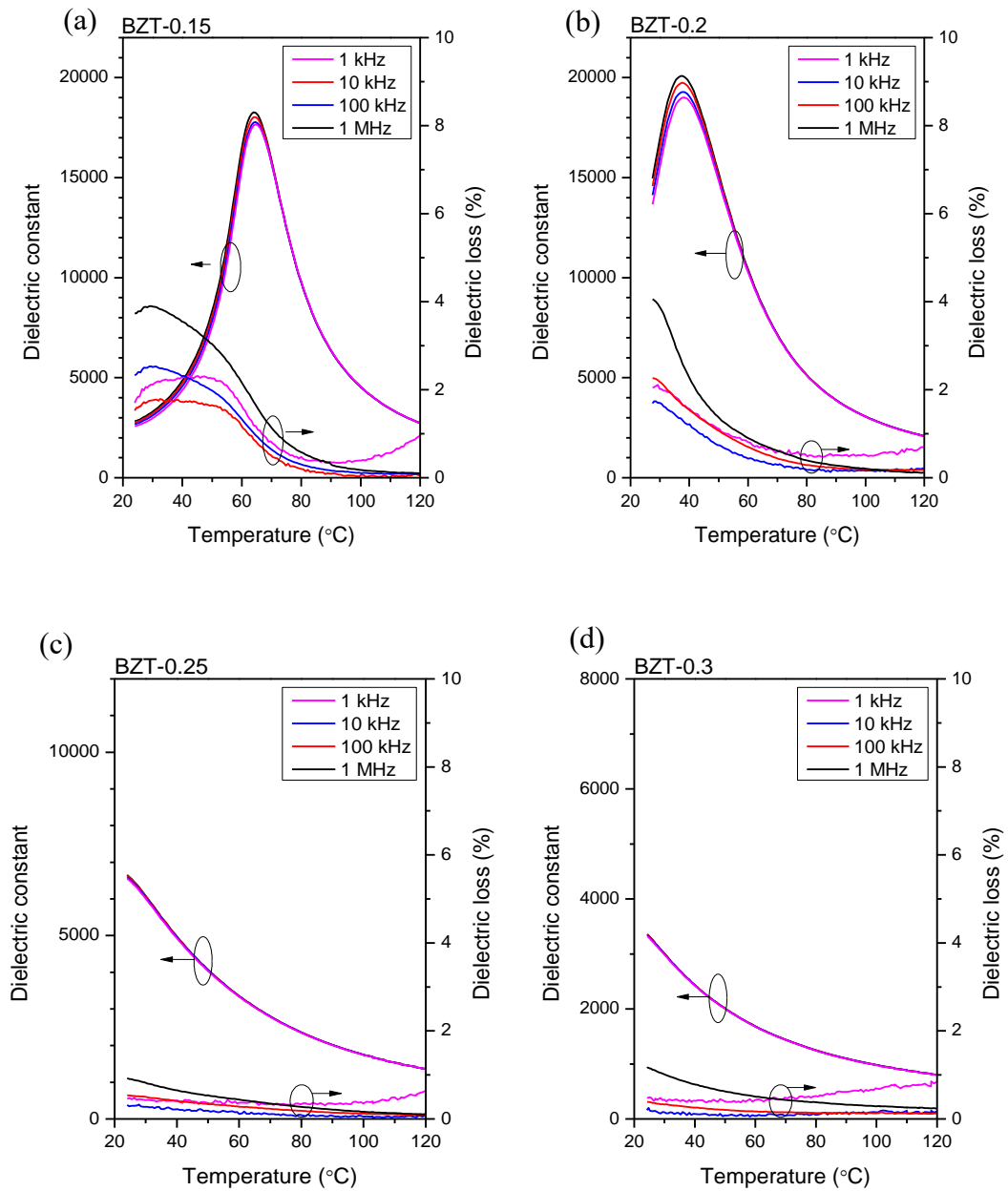


**FIGURE 3-3** Temperature dependence of dielectric properties of BZT-x ceramics (a)  $x = 0.15$ , (b)  $x = 0.2$ , (c)  $x = 0.25$  and (d)  $x = 0.3$ .



The modified Curie-Weiss law (Eq. 1.1) has been used to describe the diffuseness of the phase transition. The plots of  $\ln(1/\epsilon_r - 1/\epsilon_m)$  against  $\ln(T - T_m)$  for the BZT-x ceramics are shown in Figure 3-4. The diffuseness constants ( $\gamma$ ) can be obtained with the slope of the linear fitting curve. The calculated values  $\gamma$  for the ceramics with  $x = 0.15$  and  $0.2$  are  $1.75$  and  $1.78$  respectively. As  $\gamma = 1$  obeys a normal Curie-Weiss law and  $\gamma = 2$  defines a complete diffuse phase transition, the two samples can be considered as relaxor-like ferroelectrics [24]. In addition, BZT ceramics with  $x > 0.25$  are considered as relaxor ferroelectrics [26], [86]. Table 4 lists the  $T_m$ , dielectric constant maximum ( $\epsilon_m$ ) and  $\gamma$  for the ceramics with  $x = 0.15$  and  $0.2$ . Both  $\epsilon_m$  and  $\gamma$  increase with higher Zr content.

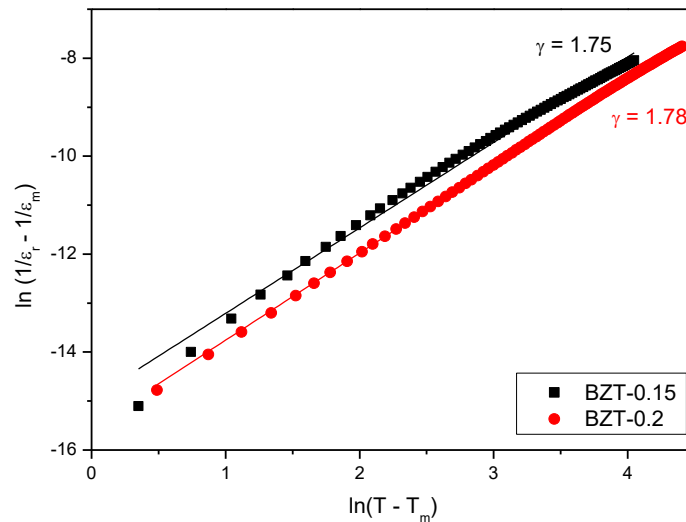


**FIGURE 3-4** Plot of  $\ln(1/\epsilon_r - 1/\epsilon_m)$  against  $\ln(T - T_m)$  for the BZT-0.15 and BZT-0.2 ceramics at 10 kHz.

**TABLE 4**  $T_m$ ,  $\epsilon_m$  and  $\gamma$  of the BZT-0.15 and BZT-0.2 ceramics at 10 kHz

BZT-x	0.15	0.2
$T_m$ (°C)	64	38
$\epsilon_m$	18000	19700
$\gamma$	1.75	1.78



### 3.5. Ferroelectric properties

The PE loops of the BZT-x ceramics measured under an E-field of 2 kV/mm at 50 Hz are shown in Figure 3-5. The observed remnant polarization ( $P_r$ ) decreases with increasing Zr content (Table 5). For the ceramics with  $x > 0.2$ , the observed  $P_r$  decreases significantly to almost zero. These should be due to the increase in amount of the paraelectric cubic phase arisen from the lowering of  $T_m$  to room temperature as shown in Figure 3-3. Also, the measured PE loops for the ceramics with  $x \leq 0.2$  are slim, which may be attributed to the presence of nano-sized polar domains [87]. A large polarization can be obtained when the E-field is sufficiently high to switch the nano-domains. A significant difference between the saturation polarization ( $P_{sat}$ ) and  $P_r$  will be resulted due to the restoration of the randomly oriented nano-domains after the removal of E-field.

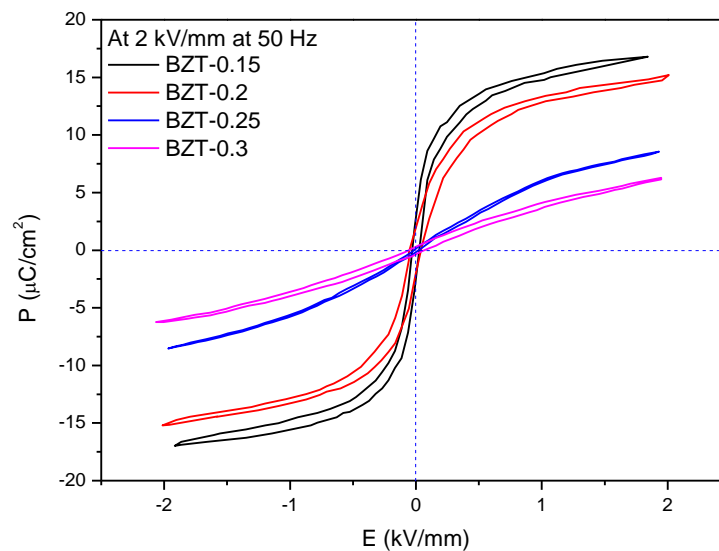


FIGURE 3-5 PE loops of BZT-x ceramics.

TABLE 5  $P_r$  and  $P_{sat}$  of the BZT-x ceramics

BZT-x	0.15	0.2	0.25	0.3
$P_r$ ( $\mu\text{C}/\text{cm}^2$ )	3.4	2.0	0.2	0.2
$P_{sat}$ ( $\mu\text{C}/\text{cm}^2$ )	16.8	15.2	8.5	6.3

### 3.6. Piezoelectric properties

The piezoelectric coefficients ( $d_{33}$ ) of the BZT-x ceramics are listed in Table 6. The observed  $d_{33}$  greatly decreases with increasing Zr content. In consistent with the observation for the PE loops and  $P_r$ , this should probably be due to increase in amount of the paraelectric cubic phase.

TABLE 6 The piezoelectric coefficient ( $d_{33}$ ) of BZT-x ceramics

BZT-x	0.15	0.2	0.25	0.3
$d_{33}$ (pC/N)	73	68	11	8

### 3.7. Conclusions

BZT-x ceramics have been successfully prepared by a solid-state reaction method and their dielectric, piezoelectric and ferroelectric properties have been studied. XRD results indicate that the ceramics have crystallized in a perovskite structure with rhombohedral and cubic phase. The BZT-x ceramics are dense and have irregular-shaped grains. As evidenced by the temperature dependence of dielectric properties, the observed  $T_m$  decreases with increasing Zr. Because of the larger amount of cubic phase, the room-temperature ferroelectric and piezoelectric properties of the ceramics with larger x are weakened. As the BZT-0.15 and BZT-0.2 ceramics have a  $T_m$  very close to room temperature, they have been selected for the hosts in achieving tuning of PL response.



## Chapter 4 RE-Doped BZT Ceramics

### 4.1. Introduction

As discussed in Chapter 1, rare earth (RE) ions can act as not only dopants for improving the functional properties of ceramic host but also activators for effectively producing photoluminescence (PL) emission [16], [50], [61], [72]. Three RE ions:  $\text{Dy}^{3+}$ ,  $\text{Er}^{3+}$  and  $\text{Eu}^{3+}$  have been selected as dopants in this work.  $\text{Dy}^{3+}$  and  $\text{Eu}^{3+}$  ions can enhance dielectric properties of barium zirconate titanate (BZT)-based ceramics [16], [61]. The PL emissions of Er-doped ceramics have been reported to be sensitive to the crystal symmetry of the host and thus to be tunable via electric field-induced phase change [68], [69]. As mentioned in Chapter 3, both the  $\text{BaZr}_x\text{Ti}_{1-x}\text{O}_3$  (BZT- $x$ ) ferroelectric ceramics with  $x = 0.15$  and  $0.2$  possess the transition temperature  $T_m$  (temperature having the dielectric constant maximum) close to room temperature. Therefore, they have been chosen as the host of luminescent materials for achieving tuning of PL under electric field (E-field). Three series of luminescent samples have been fabricated using the solid-state reaction method in this work; they are: (i) BZT- $x$  ceramics ( $x = 0.15$  and  $0.2$ ) doped with  $0.2$  mol%  $\text{Dy}^{3+}$  (BZT- $x$ -Dy); (ii) BZT- $x$  ceramics ( $x = 0.1, 0.15$  and  $0.2$ ) doped with  $0.2$  mol%  $\text{Er}^{3+}$  (BZT- $x$ -Er); and (iii) BZT- $x$  ceramics ( $x = 0.15, 0.175$  and  $0.2$ ) doped with  $0.2$  mol%  $\text{Eu}^{3+}$  (BZT- $x$ -Eu). All the samples are also abbreviated as BZT- $x$ -RE. In this chapter, their crystalline structure, microstructure as well as dielectric, ferroelectric, piezoelectric and PL properties have been investigated.



## 4.2. Crystalline structure

The XRD patterns of the BZT-x-RE ceramics, in powder form, measured in the range of  $20^\circ$  to  $80^\circ$  are shown in Figures 4-1 to 4-3, respectively. The XRD pattern of the BZT-0.15 ceramic is also included in the figures for comparison purpose. All the ceramics have been crystallized in a perovskite structure. No impurity phases are observed within detection limit of XRD, suggesting that the RE ions should have diffused in the BZT-x lattices. The enlarged XRD patterns of the ceramics in the range of  $44^\circ$  to  $46^\circ$  are also given in the figures. Similar to the results discussed in Chapter 3, a shifting of diffraction peaks toward small angles due to the lattice expansion is found with increasing Zr content. By comparing between the BZT-0.15 and BZT-0.15-RE ceramics, no significant shifting of the diffraction peaks is found. This should be due to the small amount (0.2 mol%) of RE dopant that might not be sufficient for inducing a significant change in lattice volume. Two diffraction peaks (located near  $45^\circ$ ) are found for all the ceramics except BZT-0.15-Dy and BZT-0.15-Eu, of which the peak is broadened. This might indicate that most of them (except BZT-0.1-Er) contain both rhombohedral and cubic phases as their rhombohedral-cubic transition temperatures are close to room temperature [15]. With reference to the phase diagram of BZT-x ceramics [15], the BZT-0.1-Er ceramic should possess a rhombohedral-orthorhombic transition temperature very close to room temperature and then contain both rhombohedral and orthorhombic phases at room temperature, and thus two diffraction peaks are found as shown in Figure 4-2 (b).

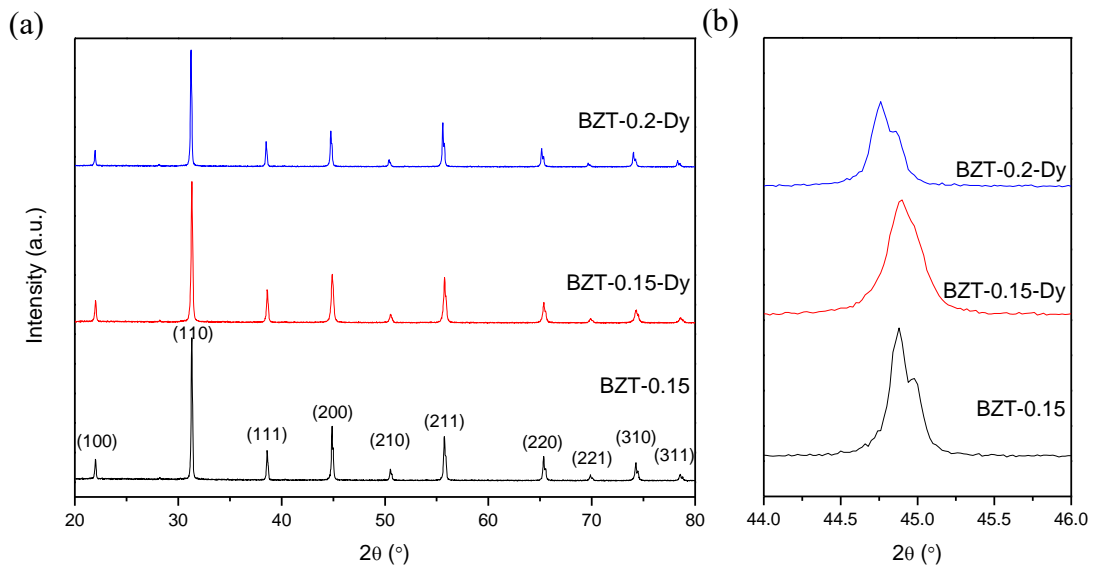


**FIGURE 4-1** The XRD patterns of the BZT-0.15 and BZT-x-Dy ceramics powders in the range of (a) 20-80° and (b) 44-46°.

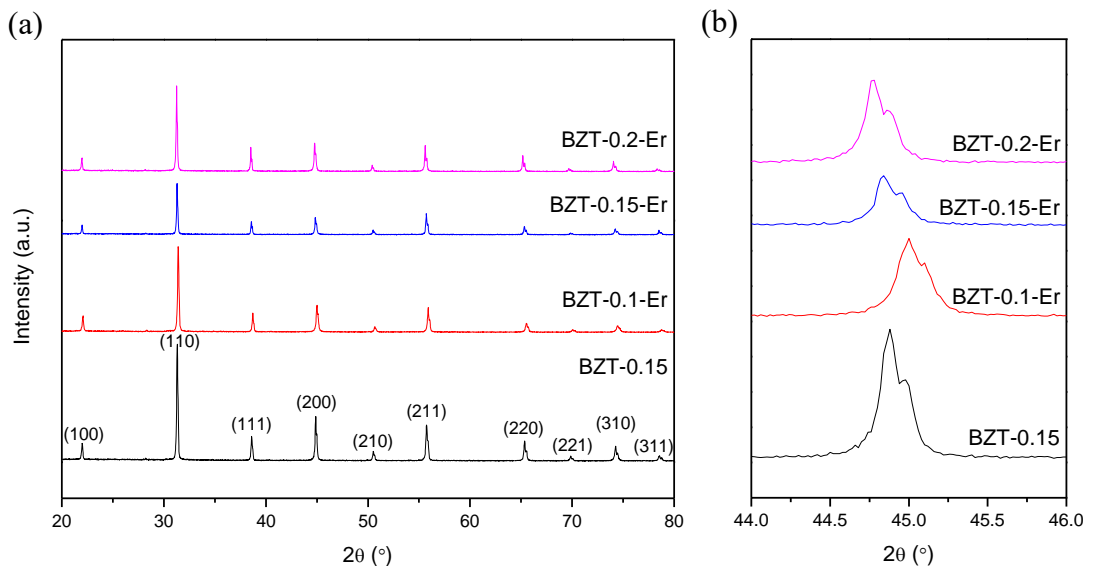


**FIGURE 4-2** The XRD patterns of the BZT-0.15 and BZT-x-Er ceramics powders in the range of (a) 20-80° and (b) 44-46°.

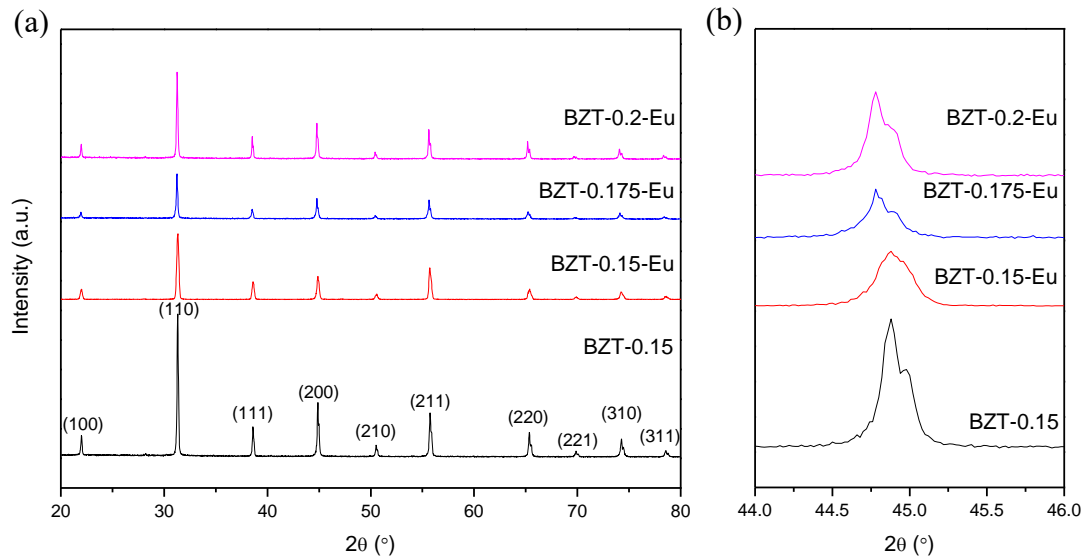


**FIGURE 4-3** The XRD patterns of the BZT-0.15 and BZT-x-Eu ceramics powders in the range of (a) 20-80° and (b) 44-46°.

The in-situ XRD patterns of BZT-0.15-Er ceramic in the range of 44-45.5° and 55-56.5° under an external E-field of 0-2000 V/mm are shown in Figure 4-4 (a) and (b) respectively. As shown in Figure 4-4 (a), a broad peak is found rather than two peaks, when comparing with the one measured with powder (Figure 4-2 (b)). This may be due to the signal intensity of ceramic is weaker than the one of powder. The ceramic should still contain both rhombohedral and cubic phase as the powder one. However, the JCPDS of rhombohedral phase of BZT ceramic is lacked. Therefore, the JCPDS of rhombohedral (R) (85-0368) and cubic (C) phase (31-0174) of BaTiO<sub>3</sub> are used as reference. Both phases contain one diffraction peak in the range of 44-46°. Diffraction peak (002)<sup>R</sup> is located at 45.3° and peak (200)<sup>C</sup> is located at 44.9°. With reference to BaTiO<sub>3</sub>, the peak has decomposed into two peaks which are indicated by green and red line for rhombohedral and cubic phase respectively. The diffraction peaks have shifted towards

small angles with increasing E-field. The shifting indicates the occurrence of lattice expansion, which may be the result of strain induced by E-field. The shifting is reversible as the peaks have almost shifted back to initial position after removal of field. An additional peak is found after application of E-field as shown in Figure 4-4 (b). According to the two JCPDS of BaTiO<sub>3</sub>, rhombohedral phase contains two peaks located at 56.1° and 56.4°, and cubic phase contains one peak located at 55.9° in the range of 55-56.5°. Therefore, the additional peak should be related to cubic phase, which also persists after removal of field, and thus it might be associated with irreversible phase change induced by E-field. This can also reveal the increase of cubic phase content. Moreover, the diffraction peaks have slightly shifted towards small angles due to strain as observed in the range of 44-45.5° (Figure 4-4 (a)).

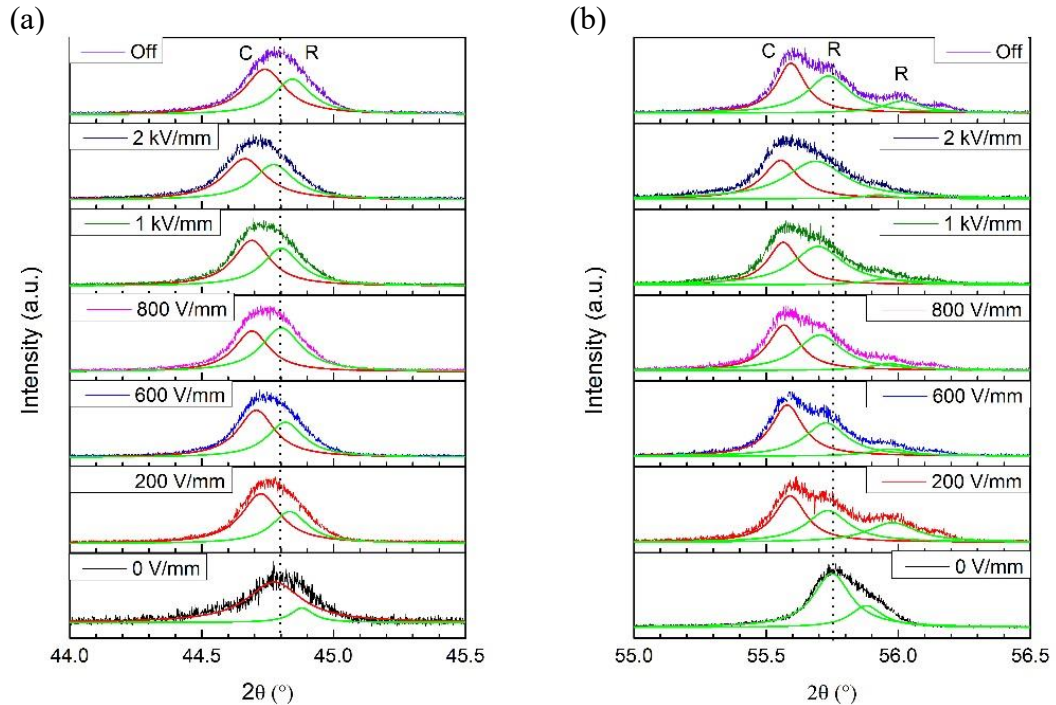


**FIGURE 4-4** The XRD patterns of the BZT-0.15-Er ceramics in the range of (a) 44-45.5° and (b) 55-56.5° under an external E-field of 0-2000 V/mm.

### 4.3. Microstructure

The FE-SEM micrographs of the BZT-x-RE ceramics are shown in Figure 4-5 to 4-7 respectively. All the ceramics are dense and have irregular-shaped grains. As compared with BZT-x-Dy and BZT-x-Er, the grains of BZT-x-Eu ceramics are uniform and fine. As shown in Table 7 to 9, the average grain sizes for the BZT-x-Dy, BZT-x-Er and BZT-x-Eu ceramics are 11-26  $\mu\text{m}$ , 43-57  $\mu\text{m}$  and 5-7  $\mu\text{m}$ , respectively. Comparing with the BZT-x ceramics, the doping of  $\text{Dy}^{3+}$  and  $\text{Eu}^{3+}$  ions can reduce the grain size while the  $\text{Er}^{3+}$ -doping does not lead to significant change. As discussed in Chapter 3, the average grain sizes for the BZT-0.15 and BZT-0.2 ceramics are 51  $\mu\text{m}$  and 45.7  $\mu\text{m}$ , respectively. Grain sizes have been reported reduced with the increasing ionic radius of dopants as dopants with larger ionic radii are hard to enter the unit cell of crystal lattice, and then are able to efficiently suppress the grain growth [88]. Among the three dopants,  $\text{Eu}^{3+}$  ion has the largest ionic radius and  $\text{Er}^{3+}$  has the smallest one. Therefore,  $\text{Er}^{3+}$ -doping does not lead to significant change when comparing with the other two dopants.

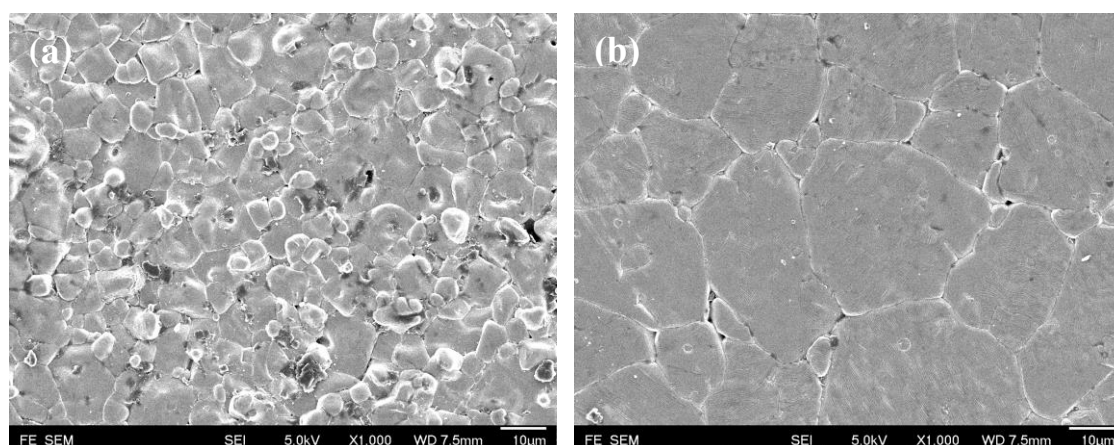


FIGURE 4-5 FE-SEM micrographs of BZT-x-Dy ceramics, (a)  $x = 0.15$  and (b)  $x = 0.2$ .

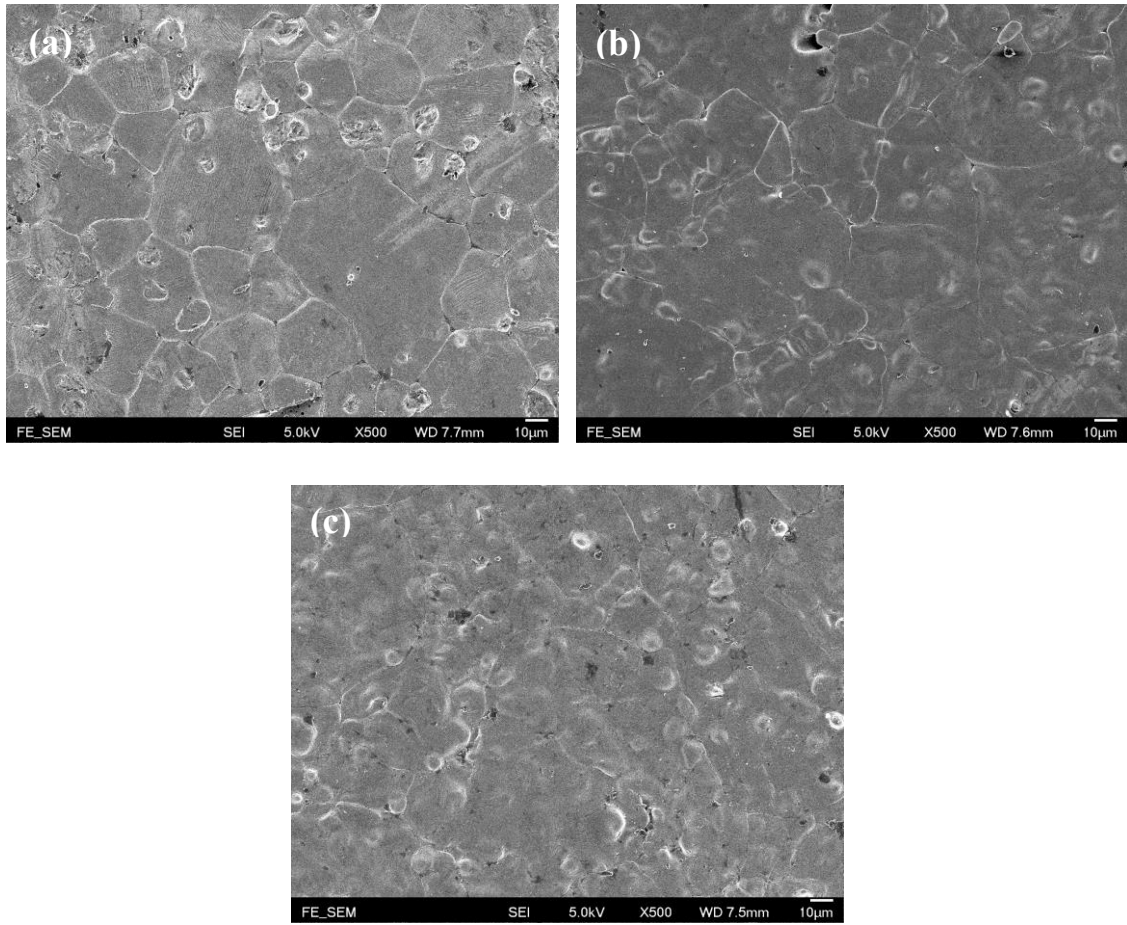
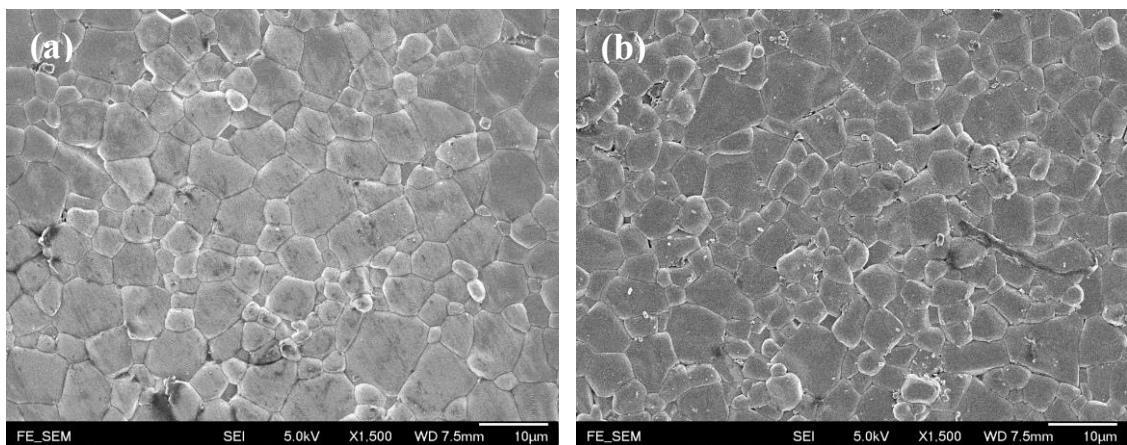


FIGURE 4-6 FE-SEM micrographs of BZT-x-Er ceramics, (a)  $x = 0.1$ , (b)  $x = 0.15$  and (c)  $x = 0.2$ .



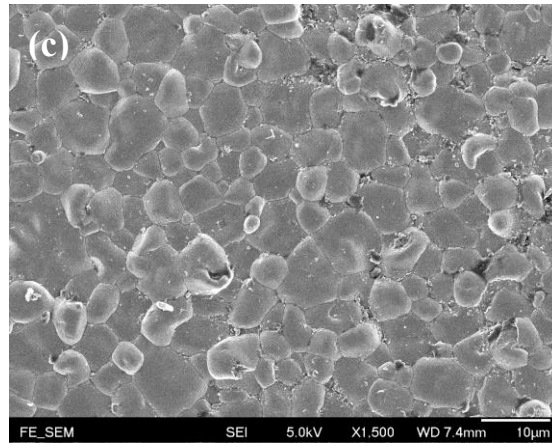


FIGURE 4-7 FE-SEM micrographs of BZT-x-Eu ceramics, (a)  $x = 0.15$ , (b)  $x = 0.175$  and (c)  $x = 0.2$ .

TABLE 7 Average grain sizes of the BZT-x-Dy ceramics

BZT-x-Dy	0.15	0.2
Sintering temperature (°C)	1580	1470
Grain size (µm)	11.1	25.6

TABLE 8 Average grain sizes of the BZT-x-Er ceramics

BZT-x-Er	0.1	0.15	0.2
Sintering temperature (°C)	1450	1560	1550
Grain size (µm)	43.4	55.3	57.1

TABLE 9 Average grain sizes of the BZT-x-Eu ceramics

BZT-x-Eu	0.15	0.175	0.2
Sintering temperature (°C)	1550	1580	1570
Grain size (µm)	4.8	6.2	6.6



#### 4.4. Dielectric properties

##### 4.4.1. Dielectric constant and dielectric loss

The observed dielectric constant ( $\epsilon_r$ ) and dielectric loss ( $\tan \delta$ ) of the BZT-x-RE ceramics measured at room temperature and 1 kHz are shown in Table 10. Apparently, the doping of  $\text{Dy}^{3+}$  and  $\text{Eu}^{3+}$  can enhance the dielectric constant of the ceramics with  $x = 0.15$  from 3000 (BZT-0.15) to 3500, but the  $\text{Eu}^{3+}$ -doping reduces it slightly to 2700. On the other hand, the dielectric constant for the ceramics with  $x = 0.2$  are enhanced from 12700 (BZT-0.2) to 15000 and 14500 after the doping of  $\text{Er}^{3+}$  and  $\text{Eu}^{3+}$ , respectively, but it is decreased to 9000 by the  $\text{Dy}^{3+}$ -doping. Moreover, the observed  $\epsilon_r$  for the ceramics increases with increasing Zr content. Similar to the discussion in Chapter 3, all the observed variations of  $\epsilon_r$  at room temperature should be mainly affected by the phase transitions, which will be discussed in the following section. Nevertheless, all the ceramics have a low dielectric loss ( $< 5\%$ ), which confirms the dense structures observed with FE-SEM.

**TABLE 10** The dielectric constant ( $\epsilon_r$ ) and dielectric loss ( $\tan \delta$ ) of BZT-x-RE ceramics measured at room temperature and 1 kHz

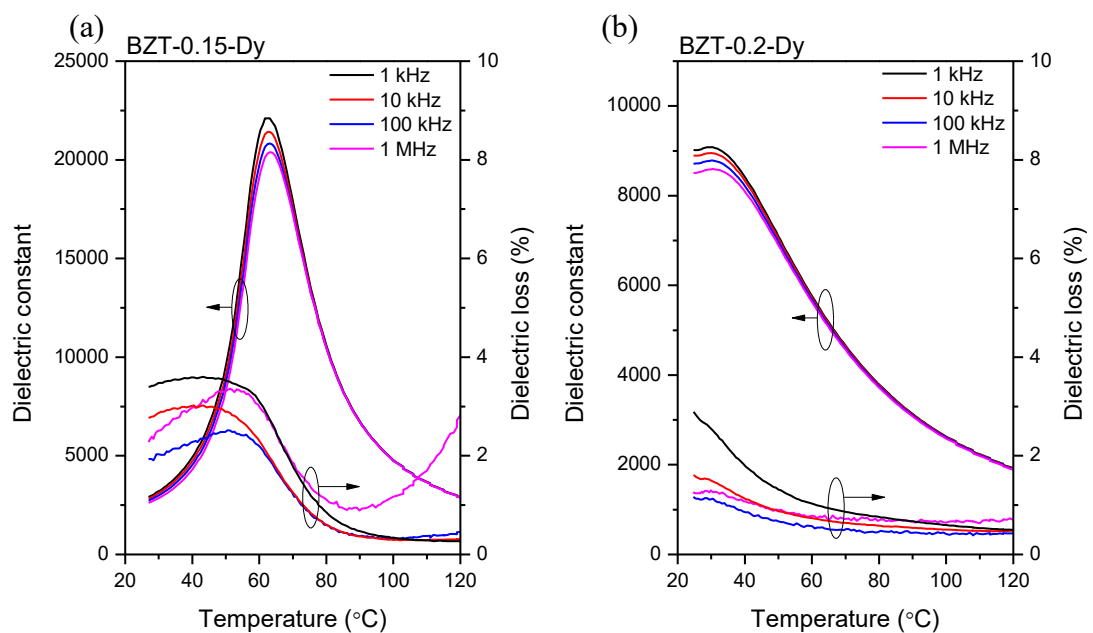
BZT-x-Dy	$\epsilon_r$	$\tan \delta$ (%)
0.15	3500	2.4
0.2	9000	1.5
BZT-x-Er	$\epsilon_r$	$\tan \delta$ (%)
0.1	1900	3.6
0.15	2700	3.8
0.2	15000	3.6
BZT-x-Eu	$\epsilon_r$	$\tan \delta$ (%)
0.15	3500	3.2
0.175	5900	4.3
0.2	14500	3.9



#### 4.4.2. Temperature dependence of dielectric properties

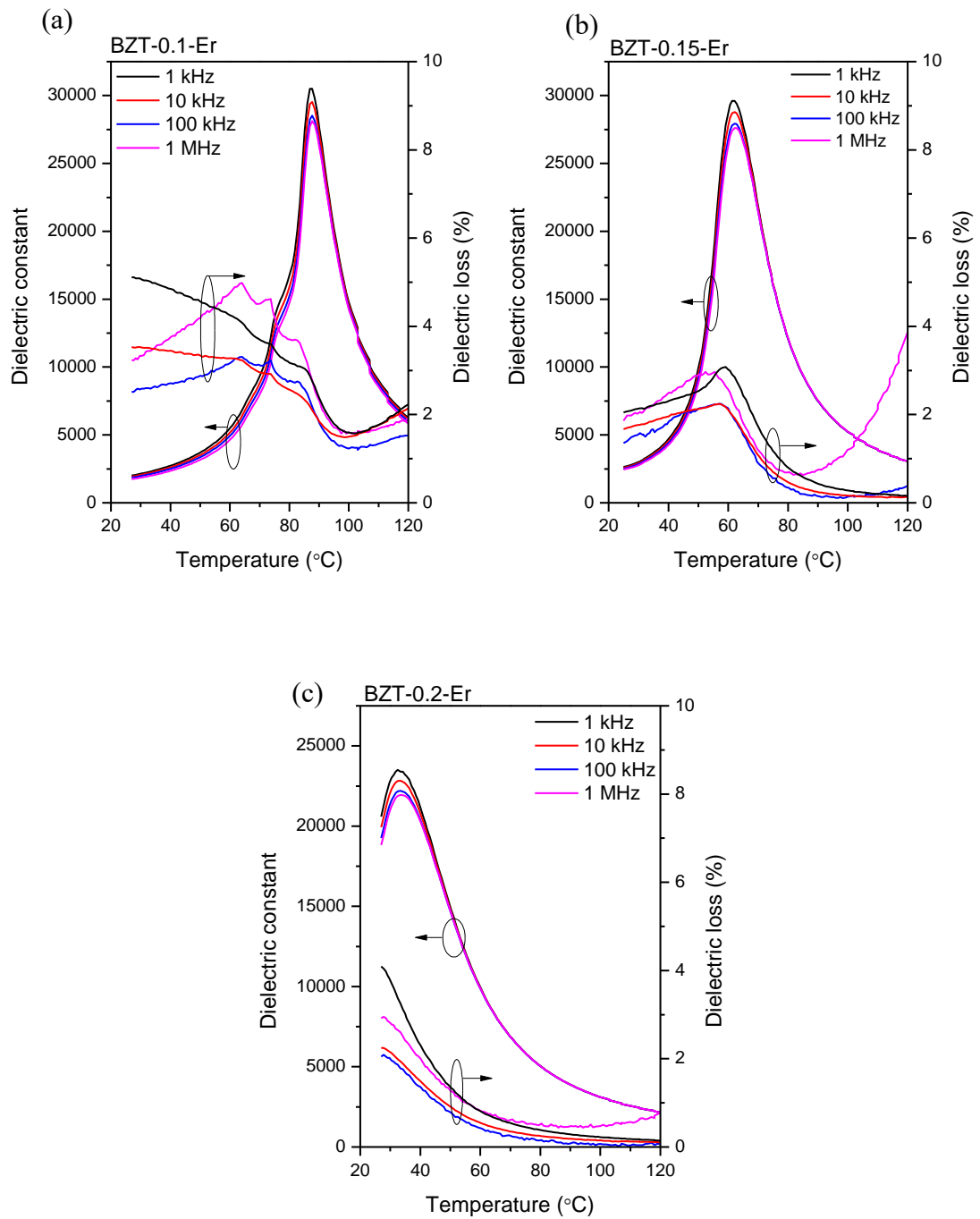
The temperature dependences of  $\epsilon_r$  and  $\tan \delta$  for the BZT-x-RE ceramics measured at 1 kHz, 10 kHz, 100 kHz and 1 MHz are shown in Figure 4-8 to 4-10 respectively. Although a complete transition peak has not been observed for some of them, e.g., BZT-0.2-Dy, because of the limitation of our measurements, it can generally affirm that all the BZT-x-RE ceramics exhibit a slightly broadened and frequency-dispersive transition peak at various temperatures, and thus confirming the diffuse nature of their phase transition. Similar to the BZT-x ceramics, the width of the peak and then the diffuseness of the transition increase slightly with increasing Zr content [26]. In addition to the frequency dispersion of  $\epsilon_r$  and  $\tan \delta$ , another characteristic of a diffuse phase transition, i.e., a relatively large difference between temperatures having the maximum  $\epsilon_r$  (i.e.,  $\epsilon_m$ ) and  $\tan \delta$  is also observed. For example, the observed temperatures for  $\epsilon_m$  and maximum  $\tan \delta$  of the BZT-0.175-Eu ceramic are 60°C and 70°C, respectively (Figure 4-10 (b)). As shown in Figure 4-9 (a), two more (local) maxima are observed in the  $\tan \delta$  curve and weak shoulders are observed in the  $\epsilon_r$  curve before the main transition peak (i.e., at temperatures below  $T_m$ ) for the BZT-0.1-Er ceramic. These should be attributed to the rhombohedral-orthorhombic and orthorhombic-tetragonal phase transitions of the ceramic [15]. According to the modified Curie-Weiss law (Eq. 1.1), the plots of  $\ln(1/\epsilon_r - 1/\epsilon_m)$  against  $\ln(T - T_m)$  for the BZT-x-RE ceramics at 10 kHz are shown in Figure 4-11 to 4-13 respectively. The diffuseness constants ( $\gamma$ ) are determined from the slopes of the linear fitting curves. The calculated  $\gamma$  for most of the BZT-x-RE ceramics (except BZT-0.1-Er) is close to 2, indicating their relaxor-like characteristics [24]. The calculated  $\gamma$  for BZT-0.1-Er is 1.44, which is close to 1 so its property should be more close to normal ferroelectric. The observed  $T_m$ ,  $\epsilon_m$  and  $\gamma$  for the BZT-x-RE ceramics are summarized in

Table 11 to 13, respectively. For each series of the ceramics, both the observed  $T_m$  and  $\epsilon_m$  decrease with increasing Zr content (i.e.,  $x$ ). Unlike  $T_m$  and  $\epsilon_m$ , the  $\gamma$  increases with increasing Zr content. As compared with BZT- $x$ , the doping of  $Dy^{3+}$  and  $Er^{3+}$  has reduced  $T_m$  slightly while the  $Eu^{3+}$ -doping does not have significant effect on  $T_m$ . As discussed in Chapter 3, the observed  $T_m$  for the BZT-0.15 and BZT-0.2 ceramics are  $64^\circ\text{C}$  and  $38^\circ\text{C}$ , respectively. Dopants with large ionic radii are found having a stronger reducing effect on  $T_m$  as they are more likely to induce distortion of crystal lattice than the one with small ionic radius [88]. However, the doping amount in this work is just 0.2 mol%, and thus the reducing effect on  $T_m$  is minor.



**FIGURE 4-8** Temperature dependence of dielectric properties of BZT- $x$ -Dy ceramics,

(a)  $x = 0.15$  and (b)  $x = 0.2$ .



**FIGURE 4-9** Temperature dependence of dielectric properties of BZT-x-Er ceramics, (a)  $x = 0.1$ , (b)  $x = 0.15$  and (c)  $x = 0.2$ .

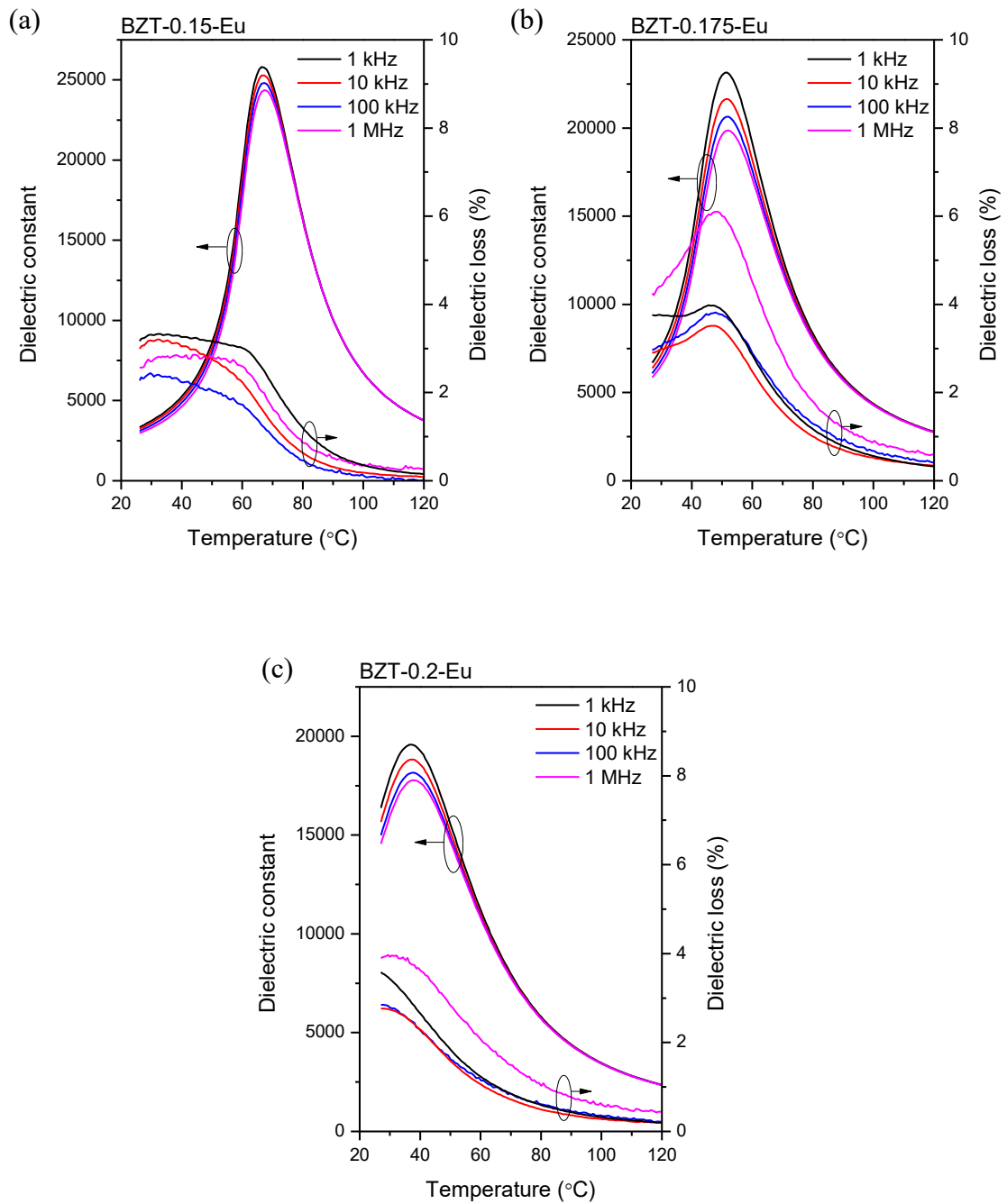


**FIGURE 4-10** Temperature dependence of dielectric properties of BZT-x-Eu ceramics, (a)  $x = 0.15$ , (b)  $x = 0.175$  and (c)  $x = 0.2$ .

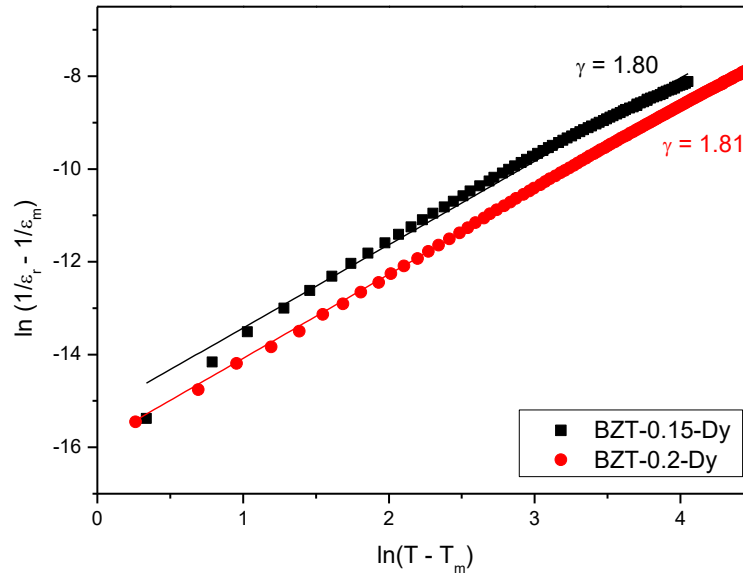


FIGURE 4-11 Plot of  $\ln(1/\epsilon_r - 1/\epsilon_m)$  against  $\ln(T - T_m)$  for the BZT-x-Dy ceramics at 10 kHz.

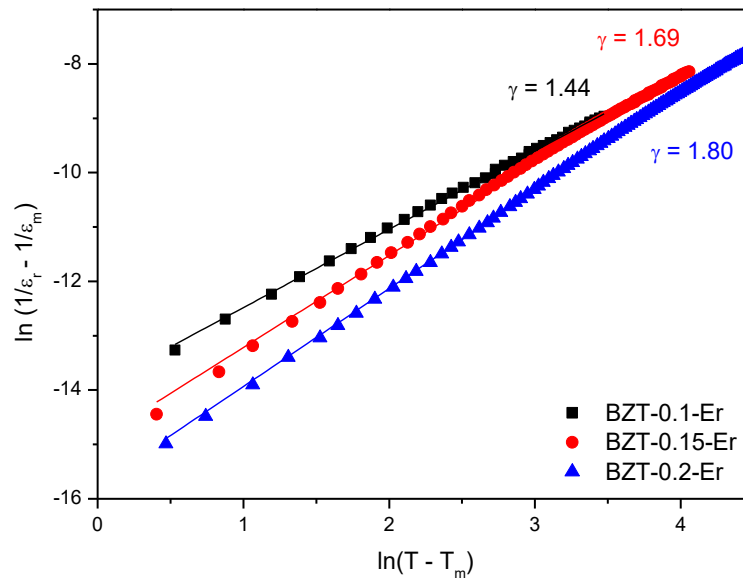


FIGURE 4-12 Plot of  $\ln(1/\epsilon_r - 1/\epsilon_m)$  against  $\ln(T - T_m)$  for the BZT-x-Er ceramics at 10 kHz.

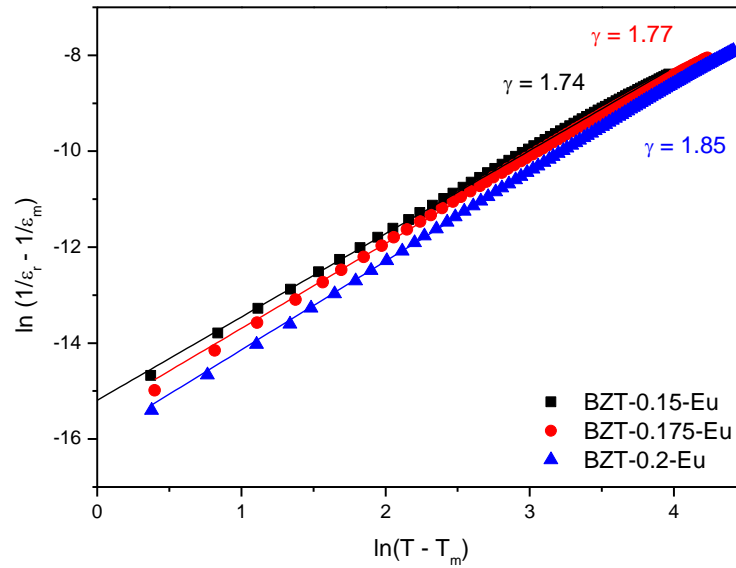


FIGURE 4-13 Plot of  $\ln(1/\epsilon_r - 1/\epsilon_m)$  against  $\ln(T - T_m)$  for the BZT-x-Eu ceramics at 10 kHz.

TABLE 11  $T_m$ ,  $\epsilon_m$  and  $\gamma$  of the BZT-x-Dy ceramics at 10 kHz

BZT-x-Dy	0.15	0.2
$T_m$ (°C)	63	30
$\epsilon_m$	21400	9000
$\gamma$	1.80	1.81

TABLE 12  $T_m$ ,  $\epsilon_m$  and  $\gamma$  of the BZT-x-Er ceramics at 10 kHz

BZT-x-Er	0.1	0.15	0.2
$T_m$ (°C)	88	62	33
$\epsilon_m$	29500	28800	22800
$\gamma$	1.44	1.69	1.80

TABLE 13  $T_m$ ,  $\epsilon_m$  and  $\gamma$  of the BZT-x-Eu ceramics at 10 kHz

BZT-x-Eu	0.15	0.175	0.2
$T_m$ (°C)	67	52	37
$\epsilon_m$	25300	21700	18800
$\gamma$	1.74	1.77	1.85



#### 4.5. Ferroelectric properties

The PE loops of the BZT-x-RE ceramics measured under an E-field of 2 kV/mm at 50 Hz are shown in Figures 4-14 to 4-16, respectively. Similar to BZT-x, the observed  $P_r$  (remnant polarization) and  $P_{sat}$  (saturation polarization) decrease with increasing Zr content (Table 14). As compared with BZT-0.15, the doping of  $Er^{3+}$  and  $Eu^{3+}$  enhances  $P_r$  slightly while the  $Dy^{3+}$ -doping reduces  $P_r$  marginally. Comparing with BZT-0.2, both the  $Dy^{3+}$ - and  $Er^{3+}$ -doping reduce  $P_r$  significantly while the  $Eu^{3+}$ -doping does not have significant effect on  $P_r$ . As discussed in Chapter 3, the observed  $P_r$  and  $P_{sat}$  of the BZT-0.15 ceramic are  $3.4 \mu\text{C}/\text{cm}^2$  and  $16.8 \mu\text{C}/\text{cm}^2$ , while those of the BZT-0.2 ceramic are  $2.0 \mu\text{C}/\text{cm}^2$  and  $15.2 \mu\text{C}/\text{cm}^2$  respectively.

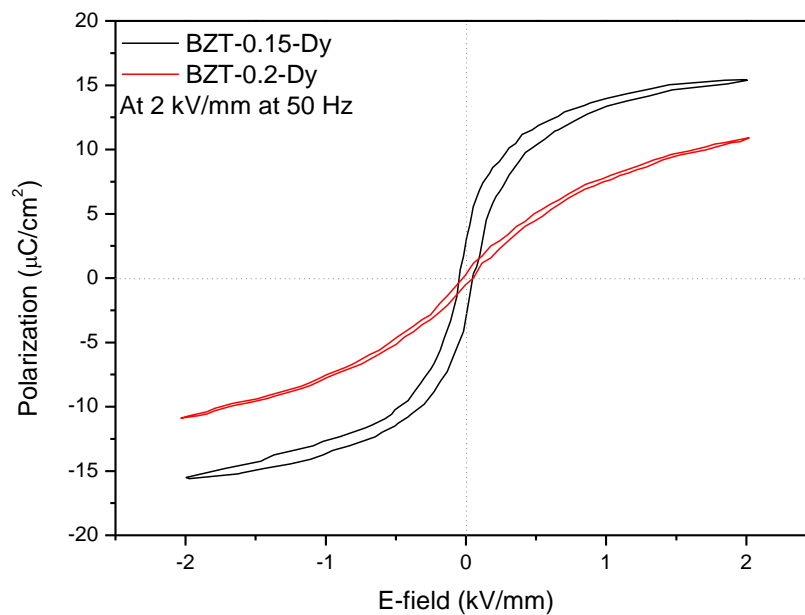


FIGURE 4-14 PE loops of BZT-x-Dy ceramics.

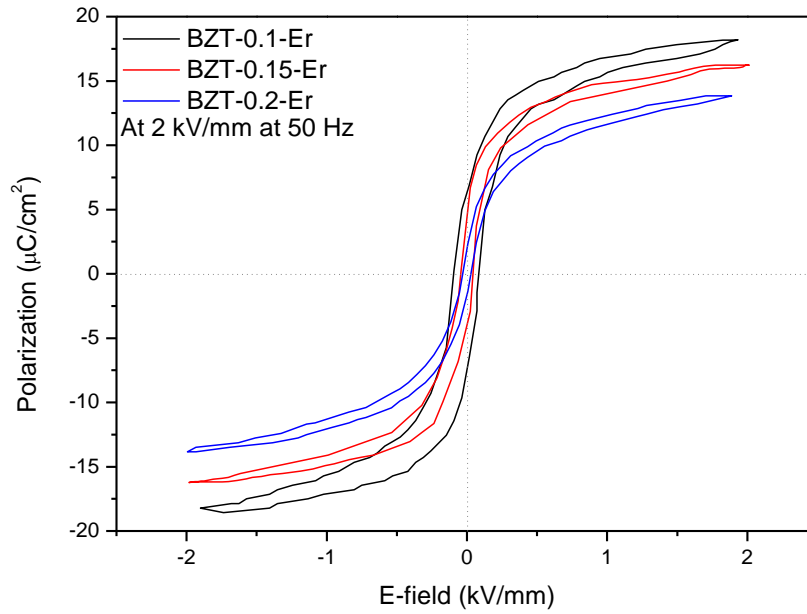


FIGURE 4-15 PE loops of BZT-x-Er ceramics.

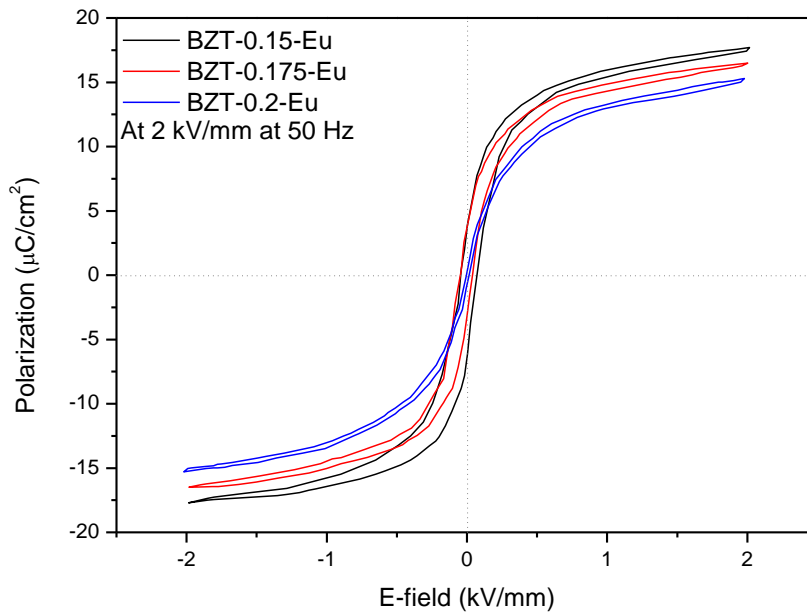


FIGURE 4-16 PE loop of BZT-x-Eu ceramics.

TABLE 14  $P_r$  and  $P_{sat}$  of the BZT-x-RE ceramics

<b>BZT-x-Dy</b>	<b><math>P_r</math> (<math>\mu\text{C}/\text{cm}^2</math>)</b>	<b><math>P_{sat}</math> (<math>\mu\text{C}/\text{cm}^2</math>)</b>
<b>0.15</b>	3.0	15.4
<b>0.2</b>	0.4	10.9
<b>BZT-x-Er</b>	<b><math>P_r</math> (<math>\mu\text{C}/\text{cm}^2</math>)</b>	<b><math>P_{sat}</math> (<math>\mu\text{C}/\text{cm}^2</math>)</b>
<b>0.1</b>	6.5	18.2
<b>0.15</b>	4.2	16.2
<b>0.2</b>	1.7	13.8
<b>BZT-x-Eu</b>	<b><math>P_r</math> (<math>\mu\text{C}/\text{cm}^2</math>)</b>	<b><math>P_{sat}</math> (<math>\mu\text{C}/\text{cm}^2</math>)</b>
<b>0.15</b>	5.1	17.7
<b>0.175</b>	3.6	16.5
<b>0.2</b>	0.8	15.3

#### 4.6. Piezoelectric properties

The piezoelectric coefficients ( $d_{33}$ ) of the BZT-x-RE ceramics are listed in Table 15. For each series of the ceramics, the observed  $d_{33}$  decreases with increasing Zr content, which is consistent with the results of the BZT-x ceramics. Among all the ceramics, the BZT-0.1-Er ceramic has the largest  $d_{33}$  (170 pC/N). This should be attributed to the high  $T_m$  (87°C) and then the absence of the paraelectric cubic phase, which are different from the other BZT-x-RE ceramics. Unlike  $\text{Dy}^{3+}$ , the doping of  $\text{Er}^{3+}$  and  $\text{Eu}^{3+}$  increase the  $d_{33}$  of the BZT-0.15 ceramic from 73 pC/N to 92 pC/N and 120 pC/N, respectively. However, all the three dopants decrease the  $d_{33}$  of the BZT-0.2 ceramic significantly from 68 pC/N to 43 - 19 pC/N. This should be attributed to the simultaneous decrease in  $T_m$  and then an increase in the content of the cubic phase.

TABLE 15 The piezoelectric coefficient ( $d_{33}$ ) of BZT-x-RE ceramics

<b>BZT-x-Dy</b>	<b><math>d_{33}</math> (pC/N)</b>
<b>0.15</b>	72
<b>0.2</b>	19
<b>BZT-x-Er</b>	<b><math>d_{33}</math> (pC/N)</b>
<b>0.1</b>	170
<b>0.15</b>	92
<b>0.2</b>	43
<b>BZT-x-Eu</b>	<b><math>d_{33}</math> (pC/N)</b>
<b>0.15</b>	120
<b>0.175</b>	70
<b>0.2</b>	30

## 4.7. Photoluminescence properties

### 4.7.1. Up-conversion PL properties

As discussed in Chapter 1,  $\text{Er}^{3+}$  ion exhibits luminescence of both Stokes (down-conversion) and anti-Stokes (up-conversion) types. Therefore, it is of great interest to study the effects of external E-field on the up-conversion (UC) PL emissions of the BZT-x-Er ceramics. The UC PL emission spectra for the BZT-0.15-Er ceramic under a 980-nm excitation have first been measured, giving the results as shown in Figure 4-17. The BZT-0.15-Er ceramic is of thickness 0.25 mm and deposited with indium tin oxide (ITO) transparent electrode on the top surface. In order to confirm the occurrence of two-photon absorption processes in producing the observed UC PL emissions, various pumping power densities have been used for the measurements. According to the theoretical consideration of multi-photon absorption processes, the relationship between the observed PL intensity ( $I$ ) and pumping power density ( $P_{\text{pump}}$ ) could be represented by the following power law with the exponent  $n$  equal to 2:



$$I \propto (P_{pump})^n \quad (4.1)$$

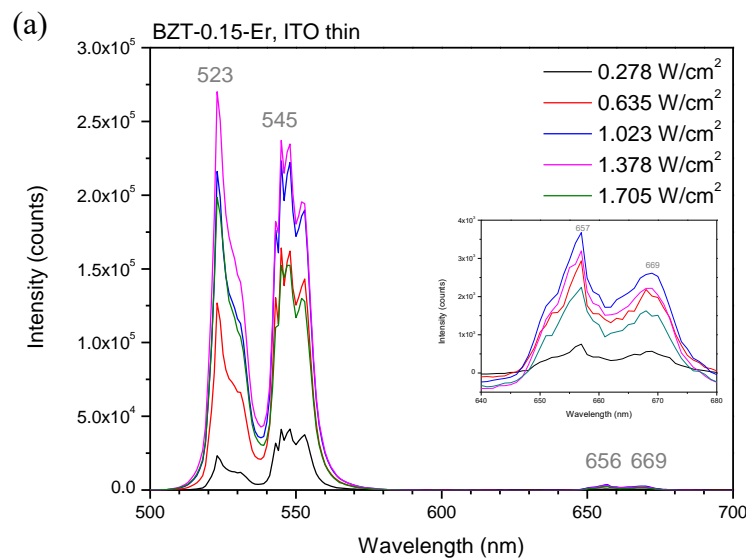
$n$  is the number of photons required for the UC process. As shown in Figure 4-17 (a), three emission bands are generally observed: two strong green emissions at 500-530 nm ( ${}^2H_{11/2} \rightarrow {}^4I_{15/2}$ ) and 530-570 nm ( ${}^4S_{3/2} \rightarrow {}^4I_{15/2}$ ), and a very weak red emission at 650-660 nm ( ${}^4F_{9/2} \rightarrow {}^4I_{15/2}$ ). The red emission has been enlarged and is shown in the inset of Figure 4-17 (a). All the three emission bands have split into numerous peaks due to the Stark effect induced by the crystal field in the BZT host [81]. The PL spectra remains almost unchanged in shape at each pumping power density. Figure 4-17 (b) shows the variations of the PL intensities of the three emission peaks with the pumping power density as well as a straight line with a slope of 2 for the ease of inspection. It can be seen that the observed PL intensities start to deviate from the reference straight line at  $P_{pump} \geq 1.02 \text{ W/cm}^2$ . This apparently suggests that the PL emissions at high pumping power densities are no longer arisen from a two-photon absorption process. However, it is suggested that even at high pumping power densities, the UC PL emissions should be stemmed from two-photon absorption processes, and the deviation from the power law should be caused by other factors, e.g., the phase change induced by the laser heating. As the ceramic sample is thin (0.25 mm) and small (0.45 cm<sup>2</sup>), and is thermally isolated from the sample holder, it may be heated up by the high-power pumping laser. As a result, a rhombohedral-to-cubic phase change and then an increases in structural symmetry may occur, and thus leading to weakening of the PL emissions and then is deviated from the power law. The relation between temperature and PL emission will be revealed in the following section. In order to study UC PL response under E-field, an excitation power that produces stable PL emissions over time is required. The emissions under a low pumping power density of 0.278 W/cm<sup>2</sup> have been recorded for 30 min (Figure 4-17 (c)).

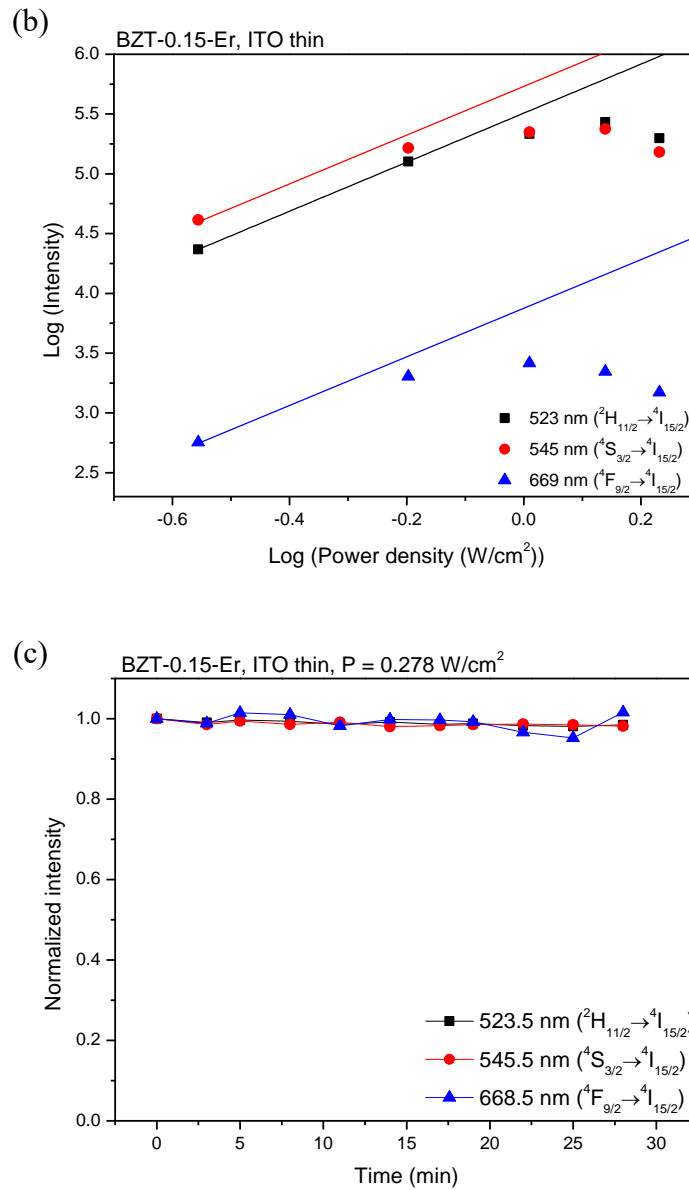


THE HONG KONG POLYTECHNIC UNIVERSITY

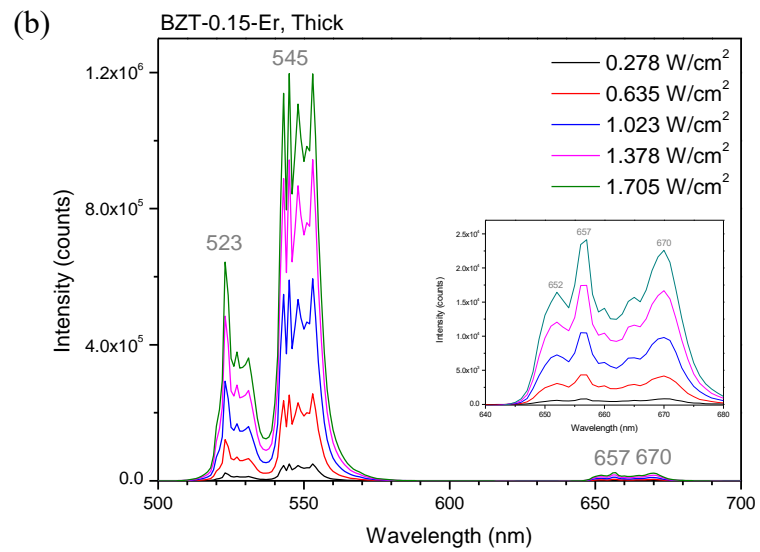
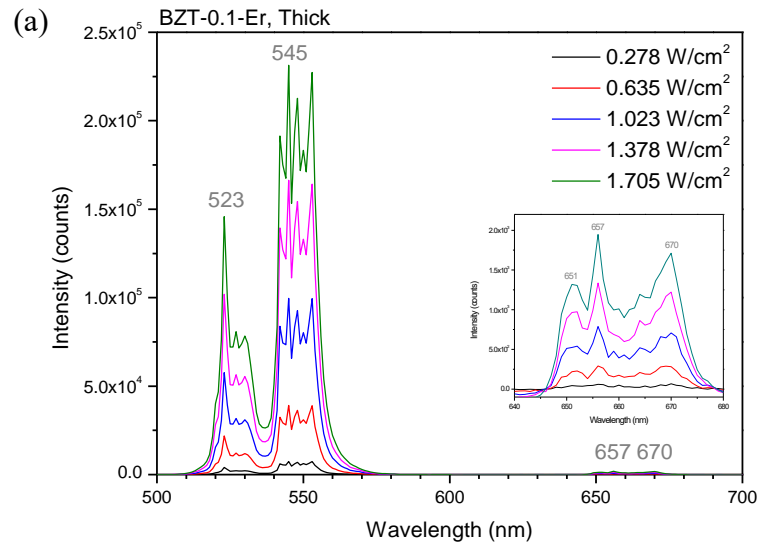
The changes in the PL intensities of the three emission peaks are less than 5%, suggesting that the excitation power is suitable for observing PL responses.

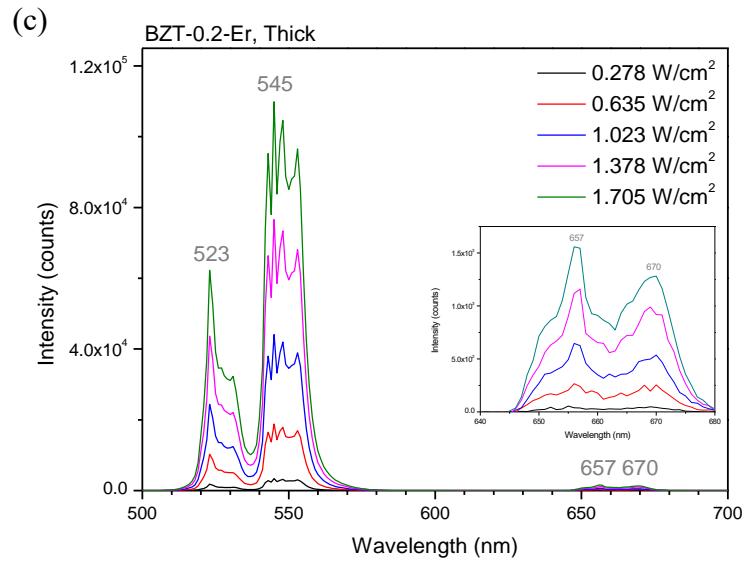
The UC PL emissions of thick and large BZT-x-Er ceramics (0.6 mm and 0.90 cm<sup>2</sup>) have then been evaluated for verifying the suggestion as well as the two-photon absorption process. As shown in Figures 4-18 (a)-(c), UC PL emissions spectra similar to those of the thin BZT-0.15-Er ceramic sample (Figure 4-17 (a)) are observed for the thick ceramics with x = 0.1, 0.15 and 0.2. In general, three emission bands are observed for each ceramic; and the PL spectra for each ceramic remains almost unchanged in shape but increases in intensity with increasing pumping power density. The variations of the PL intensities of the three emission peaks with the pumping power density for each ceramic are shown in Figures 4-19 (a)-(c). It can be seen that the observed PL intensities for each emission band of each ceramic can be well fitted to a straight line with a slope (i.e., n) very close 2 (1.74 - 2.0). This suggests that two photons are involved in producing the observed UC PL emissions even though at high pumping power densities [39].



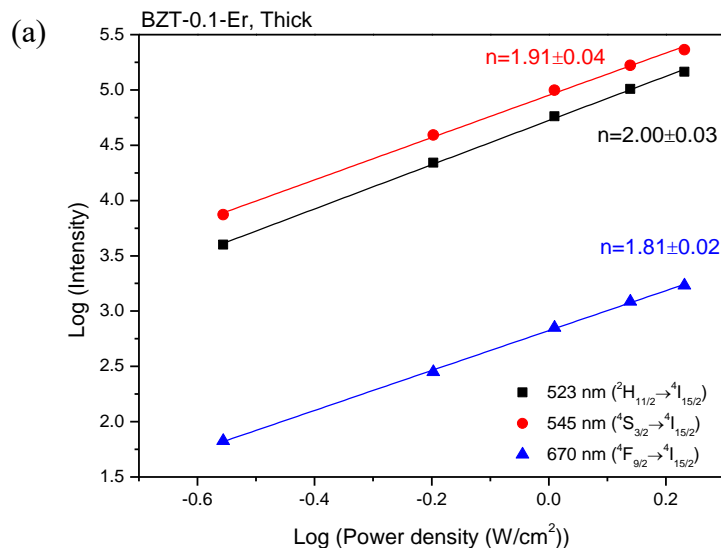


**FIGURE 4-17** (a) UC PL emission spectra under 980-nm laser excitation with power densities ranging from 0.278 to 1.705 W/cm<sup>2</sup> and the inset shows the red emission located between 640 and 680 nm, (b) emission intensities against laser power densities and (c) normalized intensities against time measured under 0.278 W/cm<sup>2</sup> excitation of BZT-0.15-Er thin ceramics sample with ITO electrode.





**FIGURE 4-18** UC PL emission spectra under 980-nm laser excitation with power densities ranging from 0.278 to 1.705 W/cm<sup>2</sup> of BZT-x-Er thick ceramics samples. The inset shows the red emission located between 640 and 680 nm, (a) x = 0.1, (b) x = 0.15 and (c) x = 0.2.



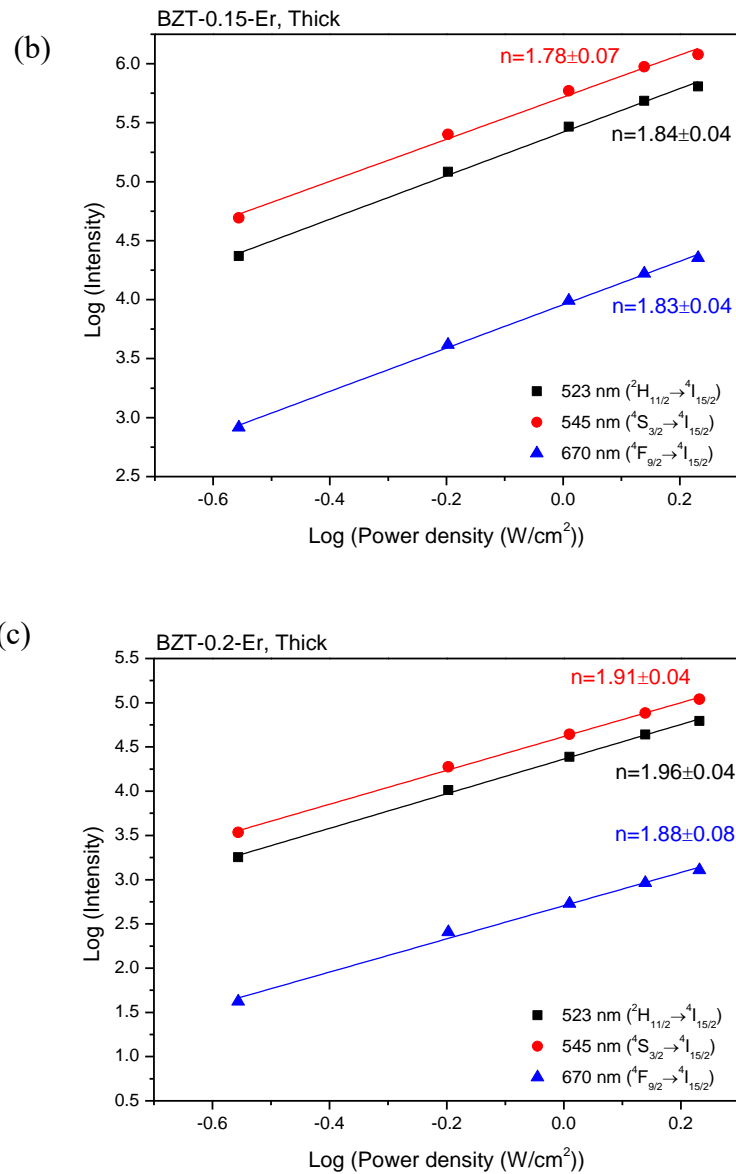


FIGURE 4-19 UC emission intensities against laser power densities of BZT-x-Er thick ceramic samples. (a) x = 0.1, (b) x = 0.15 and (c) x = 0.2.

## 4.7.2. Down-conversion PL properties

### 4.7.2.1. BZT-x-Dy ceramics

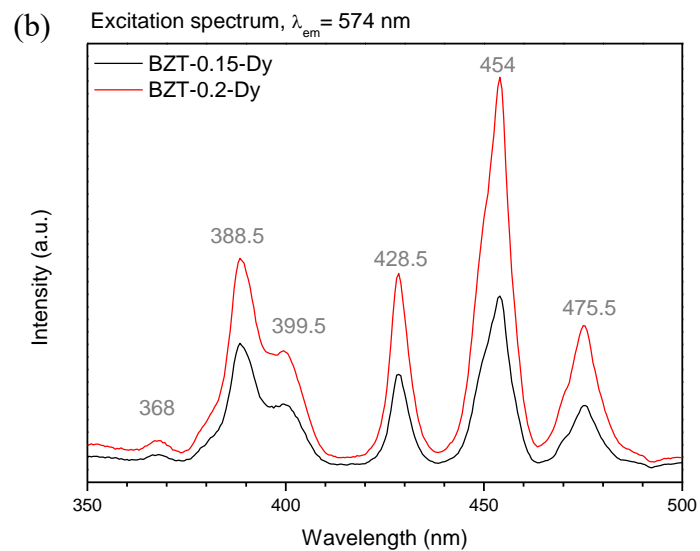
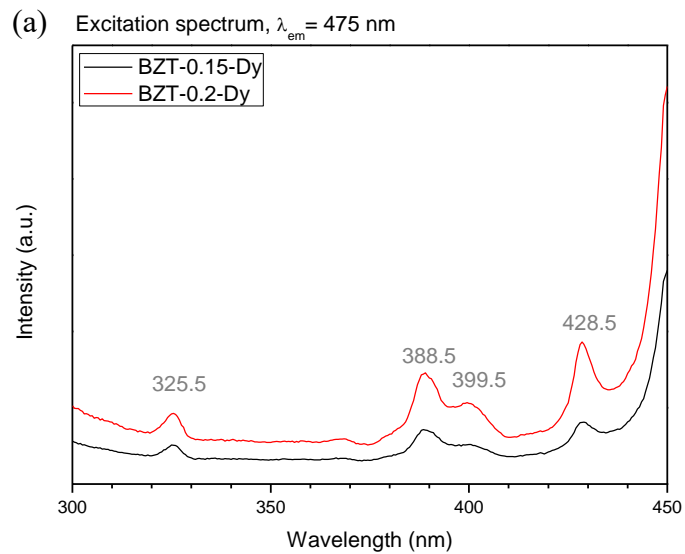
The down-conversion (DC) PL properties of BZT-x-RE ceramics have been studied in order to choose suitable excitation and emission peak for the study of PL response

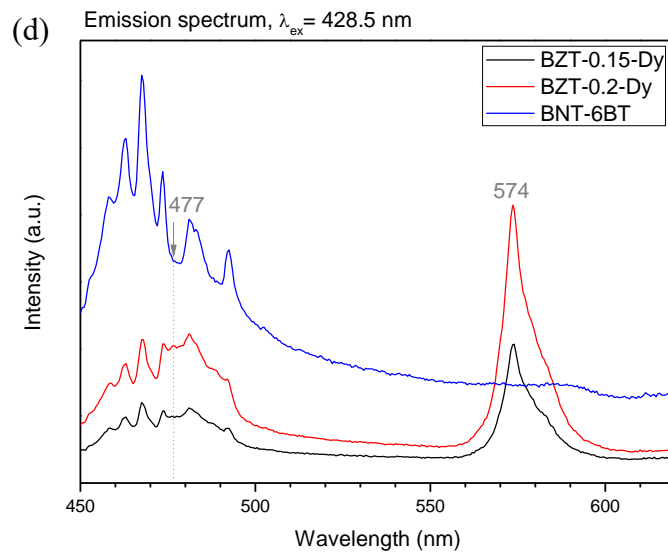
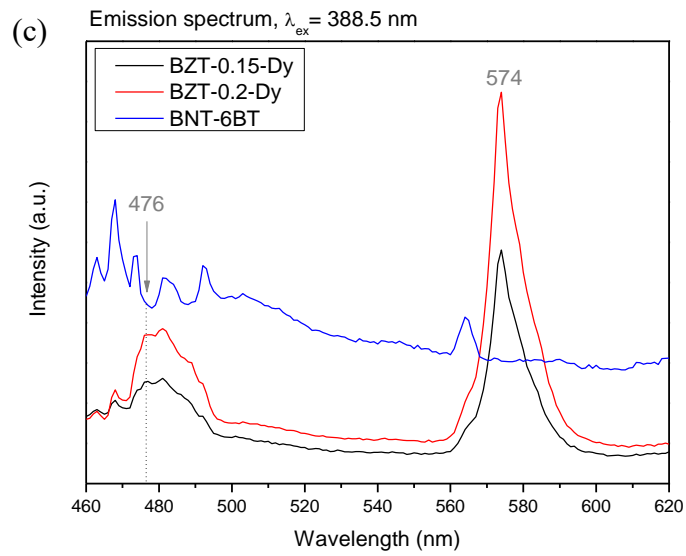


under E-field. In general,  $\text{Dy}^{3+}$  ion exhibits a blue emission at 470-500 nm and a yellow emission at 570-600 nm, which are attributed to the transition  ${}^4\text{F}_{9/2} \rightarrow {}^6\text{H}_{15/2}$  and  ${}^4\text{F}_{9/2} \rightarrow {}^6\text{H}_{13/2}$ , respectively. The photoluminescence excitation (PLE) spectra of the BZT-x-Dy ceramics monitoring at 475 nm and 574 nm have been measured, giving the results as shown in Figure 4-20 (a) and (b) respectively. The peaks attribute to the excitation of  $\text{Dy}^{3+}$  ion from the  ${}^6\text{H}_{15/2}$  ground state to the  ${}^4\text{F}_{7/2}$ ,  ${}^4\text{G}_{11/2}$ ,  ${}^4\text{I}_{15/2}$  and  ${}^4\text{F}_{9/2}$  levels are observed at 388.5 nm, 428.5 nm, 454 nm and 475 nm, respectively, for each ceramic. Owing to the high intensities, 388.5 nm, 428.5 nm and 454 nm are efficient excitation wavelengths for the ceramics. The PL DC emission spectra of the BZT-x-Dy ceramics under these excitation wavelengths are shown in Figure 4-20 (c)-(e) respectively, in which the spectra of a  $0.94(\text{Na}_{0.5}\text{Bi}_{0.5}\text{TiO}_3)$ - $0.06(\text{BaTiO}_3)$  (BNT-6BT) ceramics are also given for comparison purpose. Under the 388.5-nm excitation, blue and yellow emission peaks are found at 476 nm and 574 nm, respectively (Figure 4-20 (c)). It should be noted that the “weak” emissions observed for the 454-nm excitation (Figure 4-20 (e)) should be due to the overwhelming by the excitation source resulted from the use of an “inappropriate” filter. In general, a long-pass filter with wavelength far longer than the excitation wavelength is used for improving the signal to noise ratio. Because of our limitation, a 455-nm long-pass filter has been used for the measurement under the 454-nm excitation. Obviously, a large amount of 460-nm waves, for example, will be detected and, thus overwhelming the emissions at longer wavelengths. It has been noted that emissions in the range of 450-500 nm are commonly observed from other non-Dy-doped luminescent materials as well as non-luminescent materials such as BNT-6BT as shown in the Figures 4-20 (c) and (d). Similar results have also been obtained for the experiments using filters of different wavelengths (Table 16). It is then believed that the emissions observed in the



range of 450-500 nm should be related to the limitation of our equipment rather than to the samples. Based on the results, the 428.5-nm excitation has been used for studying PL responses under E-field.





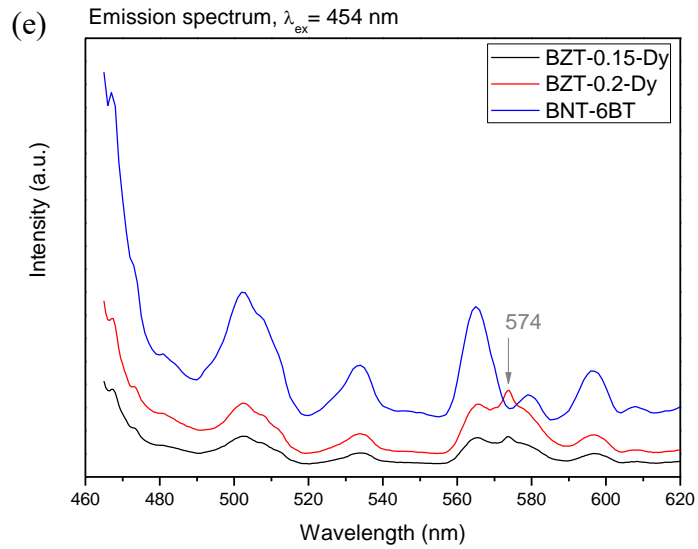


**FIGURE 4-20** DC PLE spectra of BZT-x-Dy ceramics monitored at (a) 475 nm and (b) 574 nm, and DC PL emission spectra of BZT-x-Dy and BNT-6BT ceramics under (c) 388.5-nm, (d) 428.5-nm and (e) 454-nm excitation.

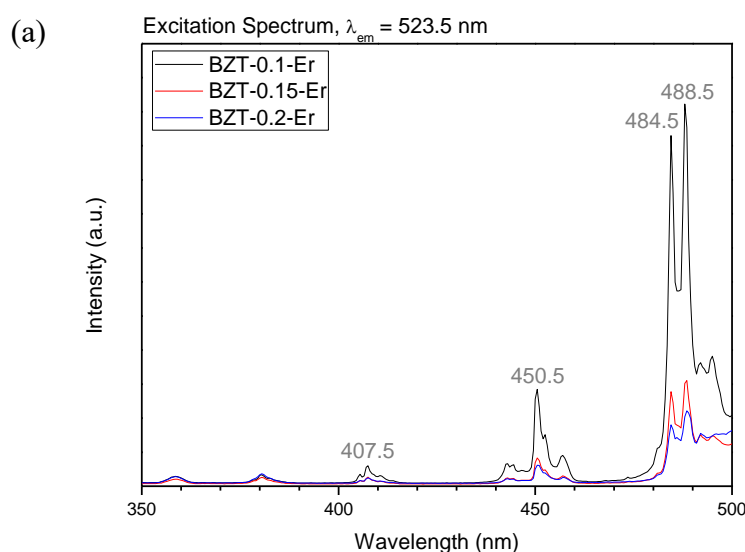
**TABLE 16** Positions of the non Dy<sup>3+</sup> emission peaks found under different measuring conditions (filter and excitation wavelength)

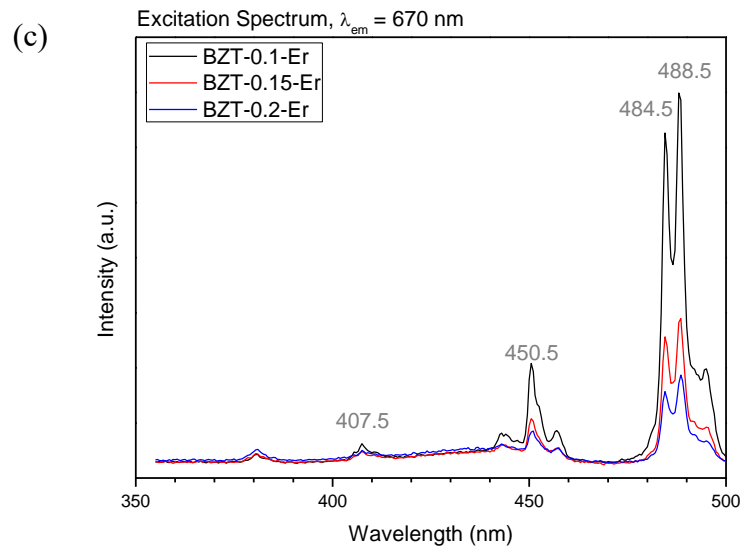
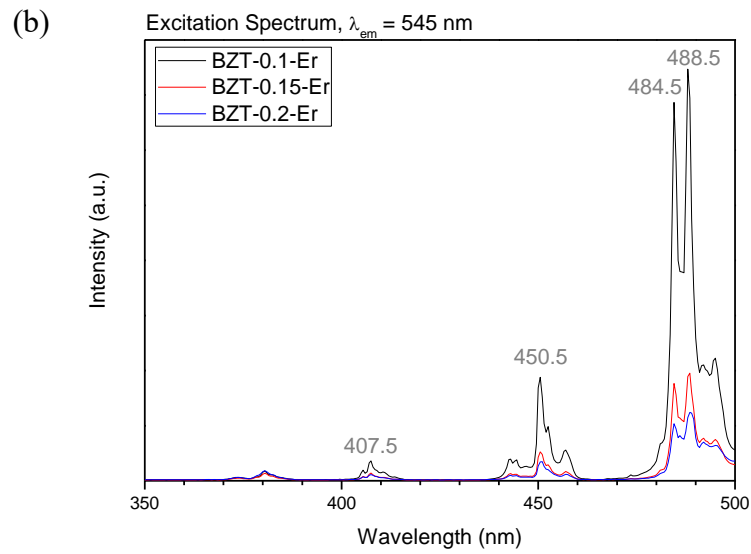
Long-pass filter	Excitation wavelength (nm)	Positions of non-Dy <sup>3+</sup> emission peaks (nm)						
455-nm	388.5		463	468	473	481	492	564
	399.5		463	468	473	481	492	
	428.5	458	462.5	467.5	473.5	481	492.5	
	454			467	473.5	481		565
395-nm	388.5	456	463	468	473	482	493	565
None	428.5			468	474	480		563



#### 4.7.2.2. BZT-x-Er ceramics

With reference to the observed UC PL emissions discussed before (Section 4.7.1) as well as the typical DC emissions of other Er-doped luminescent materials, the DC PLE spectra of the BZT-x-Er ceramics monitoring at 523.5 nm, 545 nm and 670 nm have been measured and the results are shown in Figures 4-21 (a)-(c). Similar PLE spectra are observed for each ceramic sample at each monitoring wavelength. Three main excitation peaks attributed to the excitation of  $\text{Er}^{3+}$  ions from the  $^4\text{I}_{15/2}$  ground state to the  $^2\text{H}_{9/2}$ ,  $^4\text{F}_{5/2}$  and  $^4\text{F}_{7/2}$  levels are observed at  $\sim 407.5$  nm, 450.5 nm and 488.5 nm, respectively. Because of the strongest intensity, 488.5 nm is chosen as the excitation wavelength for evaluating the DC PL emissions of the ceramics. As shown in Figure 4-21 (d), all the ceramics exhibit similar DC PL emissions, i.e., two strong green emissions at 500-530 nm ( $^2\text{H}_{11/2} \rightarrow ^4\text{I}_{15/2}$ ) and 530-570 nm ( $^4\text{S}_{3/2} \rightarrow ^4\text{I}_{15/2}$ ), and a very weak red emission at 650-660 nm ( $^4\text{F}_{9/2} \rightarrow ^4\text{I}_{15/2}$ ). The inset of Figure 4-21 (d) shows the enlarged spectra for the red emission. Similar to the UC PL emission spectra (Figure 4-18 (a)-(c)), Stark splitting arisen from the interaction between  $\text{Er}^{3+}$  ions and the host is observed.





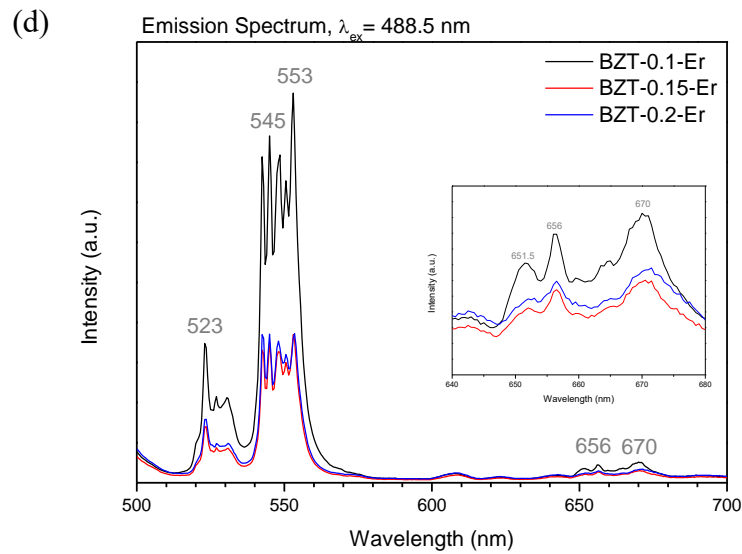


**FIGURE 4-21** DC PLE spectra of emission peaks at (a) 532.5, (b) 545 and (c) 670 nm, (d) emission spectra under 488.5-nm excitation of BZT-x-Er ceramics and the inset is the red emission.

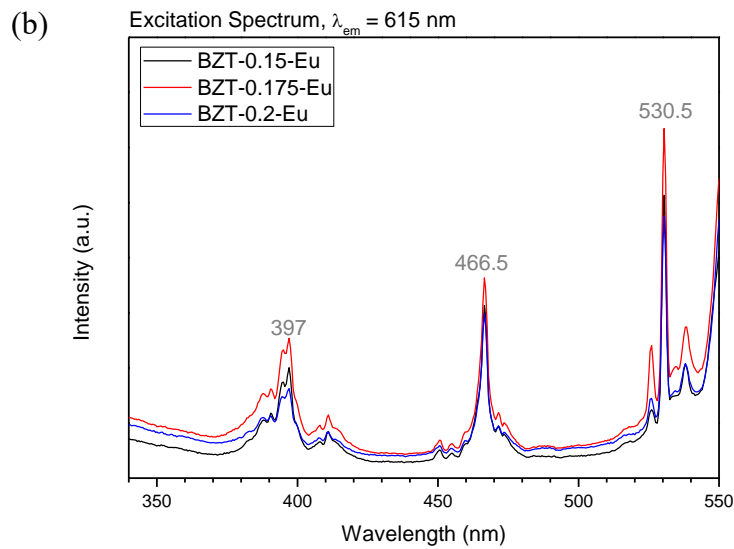
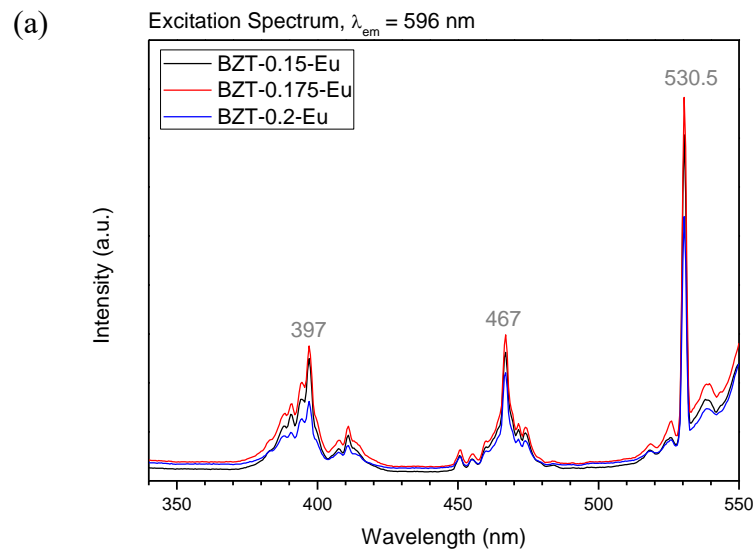
### 4.7.2.3. BZT-x-Eu ceramics

Based on the DC emissions of other Eu-doped luminescent material, the DC PLE spectra of the BZT-x-Eu ceramics monitoring at 596 nm and 615 nm have been measured and the results are shown in Figure 4-22 (a) and (b). The two PLE spectra monitored at different emission wavelengths are almost the same for each ceramic sample. The excitation peaks attributed to the excitation of  $\text{Eu}^{3+}$  ion from the  ${}^7\text{F}_0$  ground state to the  ${}^5\text{L}_6$ ,  ${}^5\text{D}_2$ ,  ${}^5\text{D}_1$  levels are observed at  $\sim 397$  nm, 466 nm and 530.5 nm respectively. Both 466 nm and 530 nm are suitable excitation wavelengths for studying the DC PL emissions of the ceramics. As shown in Figure 4-22 (c), the emission at 615 nm is stronger under 466-nm excitation than 530-nm excitation. Therefore, 466-nm is used as excitation wavelength to study the DC PL response under E-field. Under 466-nm excitation, there



THE HONG KONG POLYTECHNIC UNIVERSITY

are three red emission peaks for the ceramics: 584 nm ( ${}^5D_0 \rightarrow {}^7F_0$ ), 596 nm ( ${}^5D_0 \rightarrow {}^7F_1$ ) and 615 nm ( ${}^5D_0 \rightarrow {}^7F_2$ ) (Figure 4-22 (d)). The emission peaks at 596 nm and 615 nm are more intense than the one at 584 nm, which is consistent with the reported findings [70].



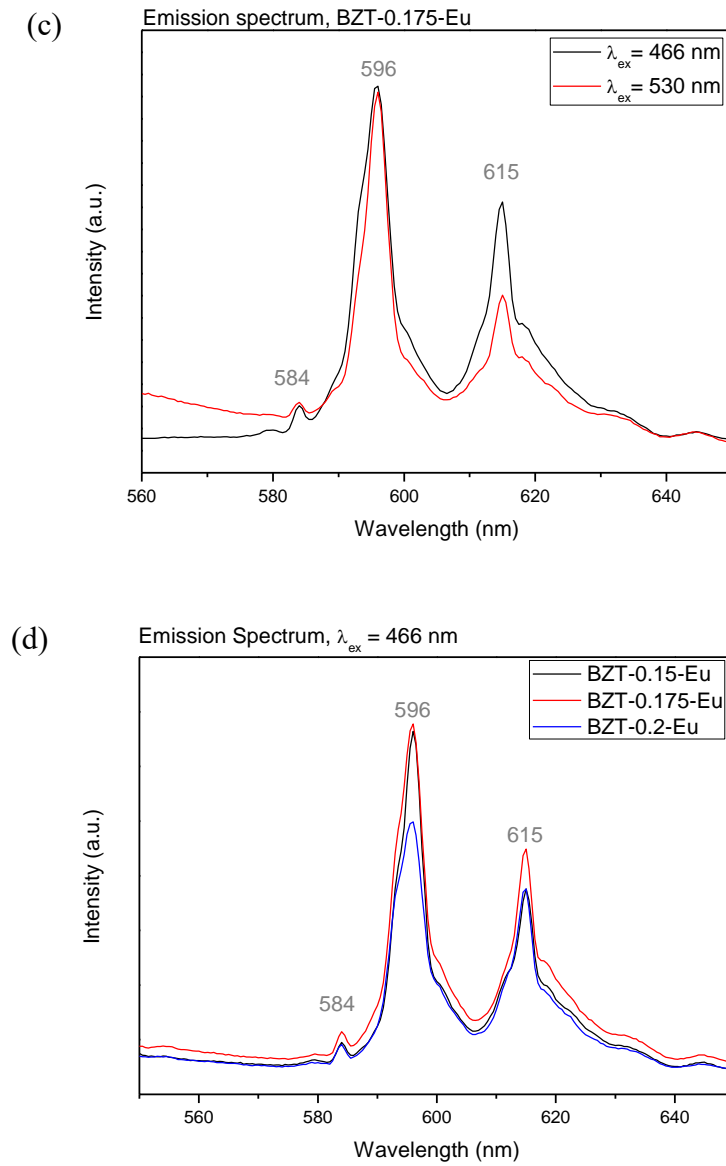


**FIGURE 4-22** DC PLE spectra of emission at (a) 596 nm and (b) 615 nm of BZT-x-Eu ceramics, (c) DC PL emission spectra under 466-nm and 530-nm excitation of BZT-0.175-Eu ceramics, (d) DC PL emission spectra under 466-nm excitation of BZT-x-Eu ceramics.



### 4.7.3. Temperature dependence of PL properties

#### 4.7.3.1. BZT-x-Er ceramics

The UC PL properties of the BZT-x-Er ( $x = 0.15$ ) ceramics at various temperatures have been investigated. Though these measurements, the effect of phase change (induced by temperature) on PL emissions can be revealed. The UC PL emission of the BZT-0.15-Er ceramic under 980-nm excitation are measured in the temperature range of 22-242°C. Figure 4-23 (a) shows the PL spectra from 22 to 102°C. The two green emissions at 523 nm ( $^2H_{11/2} \rightarrow ^4I_{15/2}$ ) and 547 nm ( $^4S_{3/2} \rightarrow ^4I_{15/2}$ ) reduce gradually with increasing temperature (T). Owing to the similar energies, the two emission levels are considered as a pair of thermally coupled emission levels [64]. As the red emission (650-660 nm) is rather weak and thus its change with T has not been observed. The PL intensities of the two green emissions are plotted against temperature (22-242°C) as shown in Figure 4-23 (b). The PL intensity at 523 nm first increases and then starts to decrease at  $T = 64^\circ\text{C}$ . Conversely, the PL intensity at 547 nm decreases steadily with increasing temperature. These should be attributed to thermal agitation (TAG) which excites electrons at the  $^4S_{3/2}$  level to the  $^2H_{11/2}$  level, and thus leading to an enhancement of PL emissions at 523 nm at the expense of the emissions at 547 nm. At  $T = 64^\circ\text{C}$  that is the  $T_m$  of BZT-0.15-Er, the rhombohedral-to-cubic phase change occurs. The structural symmetry is increased, and the PL emissions are then weakened at  $T > 64^\circ\text{C}$  [84]. Moreover, the multiphonon relaxation (non-radiative emission) rate is reported to be temperature-dependent which the rate increases with increasing temperature [89]–[91]. Therefore, the PL emissions are further weakened when the temperature rises.

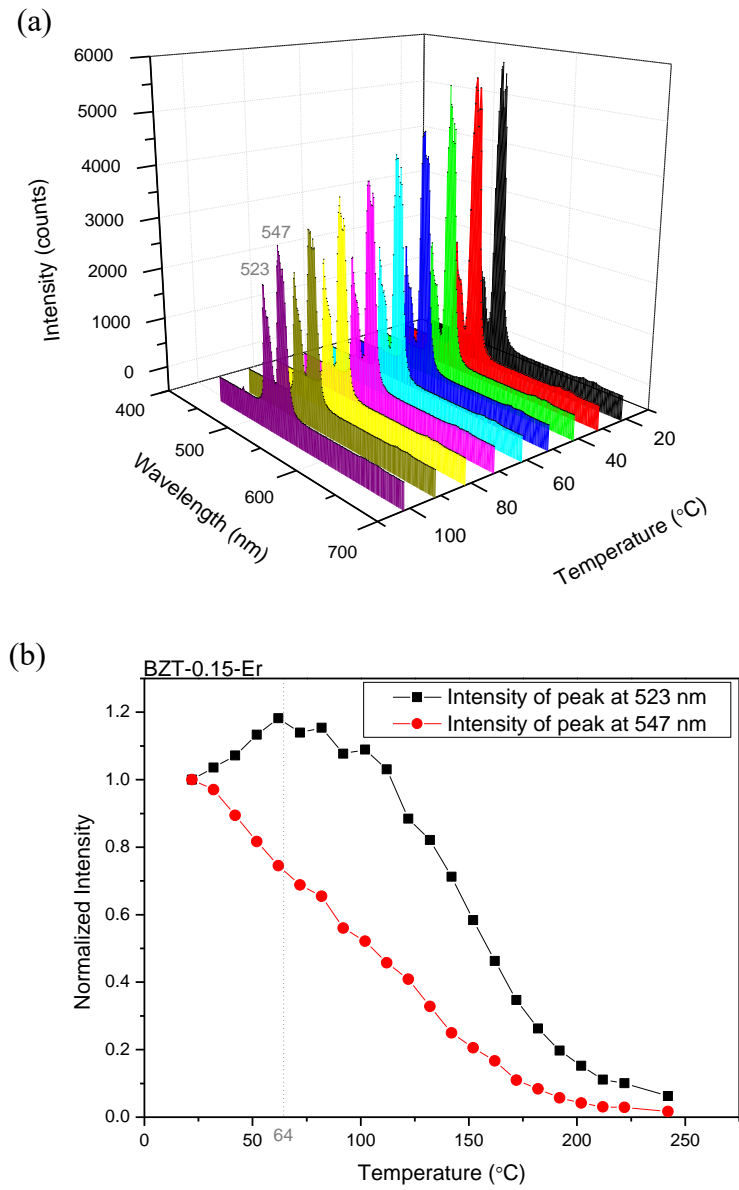
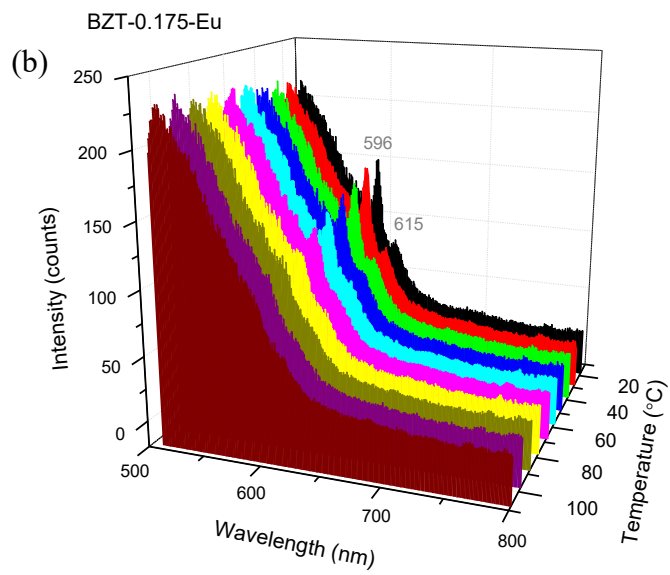
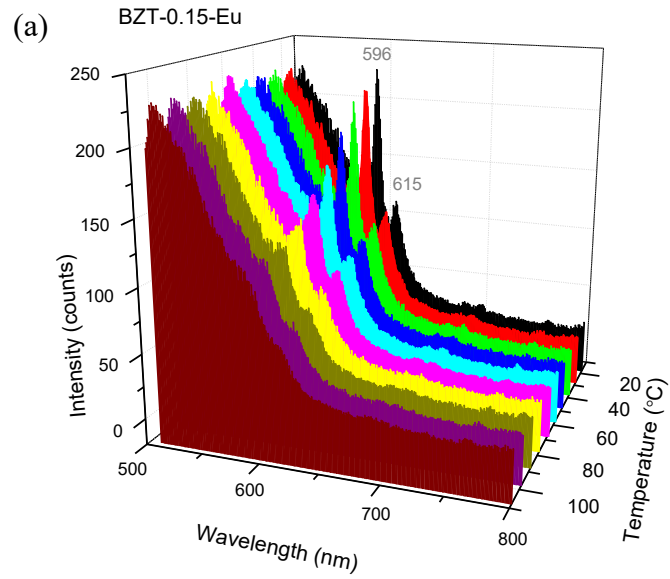


FIGURE 4-23 (a) 3D plot of temperature dependent UC PL emission spectra and (b) normalized intensities of two green emission peaks versus temperature of BZT-0.15-Er ceramic.



#### 4.7.3.2. BZT-x-Eu ceramics

The DC PL emissions of the BZT-x-Eu ( $x = 0.15$  and  $0.175$ ) ceramics under 396-nm excitation are measured in the temperature of 18-208°C. Figure 4-24 (a) and (b) show the PL spectra from 18 to 108°C for the  $x = 0.15$  and  $0.175$  ceramics, respectively. As compared with the DC PL emission spectra shown in Figure 4-22 (d), a large background signal is observed, in particular in the range of 500-620 nm, which should be attributed to the different equipment, fluorescence spectrometer (F-7000, Hitachi, Japan), used for the measurement. Nevertheless, it can be seen that for both ceramics, the two red emissions at 596 nm ( ${}^5D_0 \rightarrow {}^7F_1$ ) and 615 nm ( ${}^5D_0 \rightarrow {}^7F_2$ ) reduce gradually with increasing temperature (T). The PL intensities of the two red emissions (with background subtracted) are plotted against temperature as shown in Figure 4-24 (c) and (d). For both the  $x = 0.15$  and  $0.175$  ceramics, the PL intensities decrease significantly near their  $T_m$  (66°C and 52°C, respectively). The PL intensities of  $x = 0.15$  ceramic reduces to almost zero when  $T \geq 108^\circ\text{C}$ . When  $T \geq 98^\circ\text{C}$ , the PL intensity of emission at 596 nm of  $x = 0.175$  ceramic are  $\sim 10\%$  but the one at 615 nm seems to persist with  $\sim 20\%$ . The two emission should be almost faded but the signal to noise ratio at 615 nm is relatively low and thus leading to the inconsistent observation. Similarly, the reduction in PL intensities should be attributed to the increase in structural symmetry arisen from the rhombohedral-to-cubic phase change, and enhanced multiphonon relaxation rate due to increasing temperature.



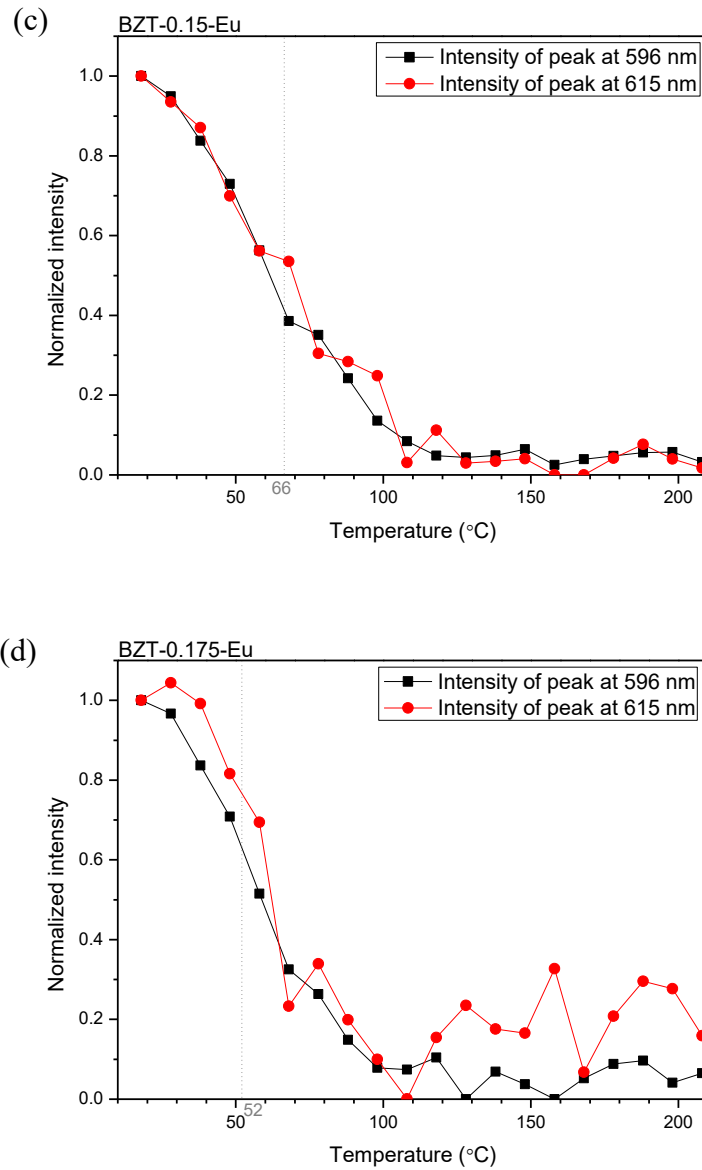


FIGURE 4-24 3D plots of temperature dependent DC PL emission spectra BZT-x-Eu ceramics, (a)  $x = 0.15$  and (b)  $x = 0.175$ . Normalized intensities of two green emission peaks versus temperature of BZT-x-Eu ceramics (with background subtracted), (c)  $x = 0.15$  and (d)  $x = 0.175$ .



#### 4.8. Conclusions

BZT-x-RE ceramics have been successfully fabricated by solid-state reaction method and their dielectric, ferroelectric, piezoelectric and PL properties have been studied. XRD results reveals that all the BZT-x-RE ceramics (except BZT-0.1-Er) have been crystallized in a perovskite structure with rhombohedral and cubic phase. The BZT-0.1-Er ceramic is in a perovskite structure with both rhombohedral and orthorhombic phase. The XRD pattern of BZT-0.15-Er ceramic has been observed under external E-field. Shifting towards small angle and additional peak are found when E-field is applied. Therefore, applying E-field might induce strain and rhombohedral-to-cubic phase change. As evidenced by FE-SEM micrographs, all the ceramics are dense and have irregular-shaped grains. According to the results of temperature-dependent dielectric properties, the  $T_m$  of all the series of ceramics decreases with increasing Zr content. Comparing with BZT-x, the observed  $\epsilon_m$  of all BZT-x-RE ceramics are also enhanced. Similar to the BZT-x ceramics, the room-temperature ferroelectric and piezoelectric properties of the BZT-x-RE ceramics are weakened with increasing x due to the increase in the cubic phase content. Both the doping of  $\text{Er}^{3+}$  and  $\text{Eu}^{3+}$  enhance considerably the piezoelectric properties of the BZT-x ceramics, but the effect of  $\text{Dy}^{3+}$  is relatively minor.

The UC PL properties of the BZT-x-Er ceramics have been investigated using the power dependent measurements for verifying the multi-photon absorption process. Moreover, the DC PL properties of the BZT-x-RE ceramics have been studied. Due to the Stark effect, both the UC and DC emission spectra of the BZT-x-Er ceramics are found with split peaks. In addition, the UC PL emission of BZT-0.15-Er and DC PL emission of BZT-x-Eu ( $x = 0.15$  and  $0.175$ ) ceramics are observed with increasing temperature. Phase change and enhanced multiphonon relaxation is found to be the main reasons for



the diminishing of the PL intensities with growing temperature. The results of the BZT-0.15-Er ceramic also shows the characteristic of the pair of thermally coupled emission levels  $^4S_{3/2}$  and  $^2H_{11/2}$  as TAG occurs between the two levels.



## Chapter 5 Electric Field-Induced PL Response of RE-Doped BZT Ceramics

### 5.1. Introduction

As discussed in Chapter 1, the photoluminescence (PL) property can be manipulated with external electric field (E-field) [78], [81]. Also, tunable PL property allows numerous optical applications, such as biological labeling, volumetric 3D displays and long-distance quantum communication if rapid and reversible manipulation is realized [43], [73], [74]. In this work, ferroelectric ceramic barium zirconate titanate (BZT) has been chosen as the host and three rare earth (RE) ions:  $\text{Dy}^{3+}$ ,  $\text{Er}^{3+}$  and  $\text{Eu}^{3+}$  have been selected as dopants in order to achieve tuning of PL emissions under E-field. Three groups of RE-doped samples have been studied; they are: (i)  $\text{BaZr}_x\text{Ti}_{1-x}\text{O}_3$  (BZT-x) ceramics ( $x = 0.15$  and  $0.2$ ) doped with  $0.2$  mol%  $\text{Dy}^{3+}$  (BZT-x-Dy); (ii) BZT-x ceramics ( $x = 0.1$ ,  $0.15$  and  $0.2$ ) doped with  $0.2$  mol%  $\text{Er}^{3+}$  (BZT-x-Er); and (iii) BZT-x ceramics ( $x = 0.15$ ,  $0.175$  and  $0.2$ ) doped with  $0.2$  mol%  $\text{Eu}^{3+}$  (BZT-x-Eu). All the samples are also abbreviated as BZT-x-RE. Results in Chapter 4 indicate that the three ions can not only enhance the functional properties of host but also act as activator for PL emission. Suitable excitation wavelengths have been chosen for each of the dopants based on the PL measurements. Moreover, the in-situ XRD result of BZT-0.15-Er ceramic shows rhombohedral-to-cubic phase change and strain might be induced by E-field. In this chapter, PL responses of the BZT-x-RE ceramics under external E-field have been investigated. Indium tin oxide (ITO) transparent electrodes have been deposited on the sample surfaces using magnetron sputtering for the application of E-field.

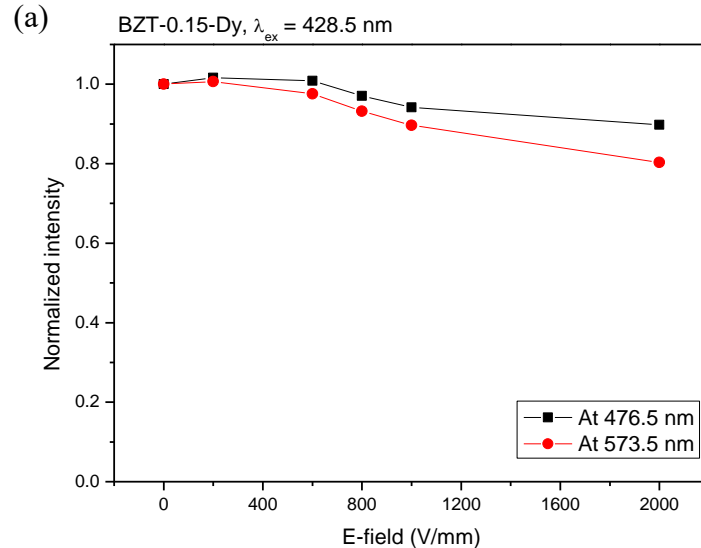


## 5.2. BZT-x-Dy ceramics

The down-conversion (DC) PL responses of the BZT-0.15-Dy ceramics under an E-field of 0-2000 V/mm have been measured; from which the observed PL intensities at 476.5 nm ( ${}^4F_{9/2} \rightarrow {}^6H_{15/2}$ ) and 573.5 nm ( ${}^4F_{9/2} \rightarrow {}^6H_{13/2}$ ) are determined and plotted as a function of E-field as shown in Figure 5-1 (a). Both the observed PL intensities remain almost unchanged with increasing E-field, and then start to decrease gradually when the E-field becomes higher than 600 V/mm. Under an E-field of 2 kV/mm, the PL intensity of the blue emission (476.5 nm) reduces to 90% and that of the yellow emission (573.5 nm) reduces to 80%. Moreover, it has been noted that the PL emissions continue to weaken under the E-field. After 40 min under 2 kV/mm, the observed PL intensity of the blue emission reduces significantly to 60% (with reference to the initial value), while that of the yellow emission reduces to 45% (Figure 5-1 (b)). After the removal of the E-field, both the emissions become slightly stronger, showing a recovery in PL intensity of 8% and 12%, respectively, in 60 min. Unlike BZT-0.15-Dy, there are no significant changes (< 10%) in the PL emissions of the BZT-0.2-Dy ceramic under various E-fields as shown in Figure 5-1 (c). The reductions in PL emissions are assumed to be mainly due to the phase change of the ceramic host induced by the E-field. As in-situ XRD pattern of BZT-0.15-Er ceramic observed under E-field indicated, applying E-field might induce rhombohedral-to-cubic phase change and strain (Section 4.2). Moreover, Ti-rich and Zr-rich cluster retaining their individuality have been observed in BZT ceramics, which might thus be considered as a mixture of BaTiO<sub>3</sub> and BaZrO<sub>3</sub> [28]. In addition, it has been reported that the phase transition temperature of BaTiO<sub>3</sub> could be reduced by high E-fields [92], [93]. As a result, the application of the high E-field (2 kV/mm) may lead to a rhombohedral-to-cubic phase change and thus an increase in structural symmetry in the



BZT-0.15-Dy ceramic. It has been reported that an increase in structural symmetry will weaken PL emissions [84]. Owing to the low transition temperature  $T_m$  (i.e., the temperature at which the dielectric constant becomes maximum, 30°C), the rhombohedral phase content of the BZT-0.2-Dy ceramic (at room temperature) should be low, and thus the relative change in cubic phase content arisen from the E-field should not be high enough to induce a significant change in PL emissions. Another factor might lead to changes in structural symmetry and then PL emissions is the alignment of the spontaneous polarization [78]. As evidenced by the limited recovery in PL intensity after the removal of the E-field (Figure 5-1 (b)), the effects of polarization alignment and strain should be minor for the BZT-x-Dy ceramics.



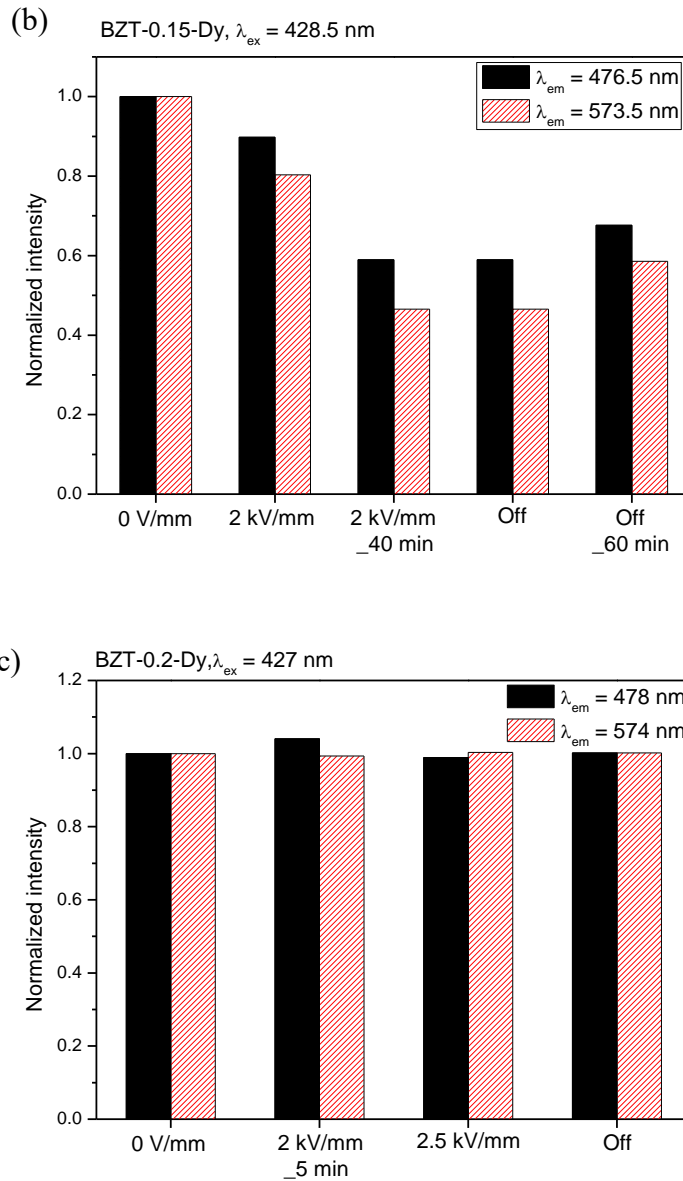


FIGURE 5-1 (a) DC PL response under different E-fields of BZT-0.15-Dy, DC PL response of BZT-x-Dy ceramics under E-field and removal of field (b)  $x = 0.15$  and (c)  $x = 0.2$ .



### 5.3. BZT-x-Er ceramics

The up-conversion (UC) and DC PL responses of the BZT-x-Er ceramics under external E-fields have been studied. The variations of the observed UC PL intensities at 523.5 nm ( $^2H_{11/2} \rightarrow ^4I_{15/2}$ ) and 548 nm ( $^4S_{3/2} \rightarrow ^4I_{15/2}$ ) with E-field in the range of 0-2000 V/mm for the BZT-0.1-Er ceramic are shown in Figure 5-2 (a). Both the PL intensities change slightly ( $< 5\%$ ) with increasing E-field. Although a higher E-field (3 kV/mm) has been applied for 10 min, they only reduce to 94% (Figure 5-2 (b)). After the removal of the E-field, a recovery of about 2% is observed for both the PL intensities in 30 min. Figure 5-3 (a) shows the variations of the observed DC PL intensities at 523.5 nm and 548 nm with E-field in the range of 0-2000 V/mm. Similarly, a slight reduction ( $< 10\%$ ) in both the PL intensities are observed. However, as shown in Figure 5-3 (b), after applying a higher E-field of 3 kV/mm for 10 min, the reductions of the PL intensities at 523.5 nm and 548 nm increase to 15% and 13%, respectively. After the removal of E-field (Figure 5-3 (b)), the recoveries in PL intensities are slight,  $< 5\%$  in 30 min. As discussed in Chapter 4, the BZT-0.1-Er ceramic has three phase transitions: rhombohedral-orthorhombic, orthorhombic-tetragonal and tetragonal-cubic. The observed  $T_m$  of the BZT-0.1-Er ceramic, which is  $88^\circ\text{C}$  and refers to the tetragonal-cubic transition, is far above room temperature. Therefore, the rhombohedral-orthorhombic and orthorhombic-tetragonal transitions (with corresponding temperatures  $65^\circ\text{C}$  and  $74^\circ\text{C}$ , respectively) are more likely to be induced by the external E-field. The two transitions have opposite effects on PL emissions. The rhombohedral-orthorhombic phase transition will reduce the crystal symmetry and then enhance the PL intensities. On the other hand, the orthorhombic-tetragonal phase transition will increase the crystal symmetry and weaken the PL emissions. Accordingly, if both occur simultaneously, their effects on PL

intensity will be neutralized, and thus leading to a minor change in PL intensities. Moreover, the minor recovery may indicate that the effect of polarization alignment on PL intensity for the BZT-0.1-Er ceramic is small.

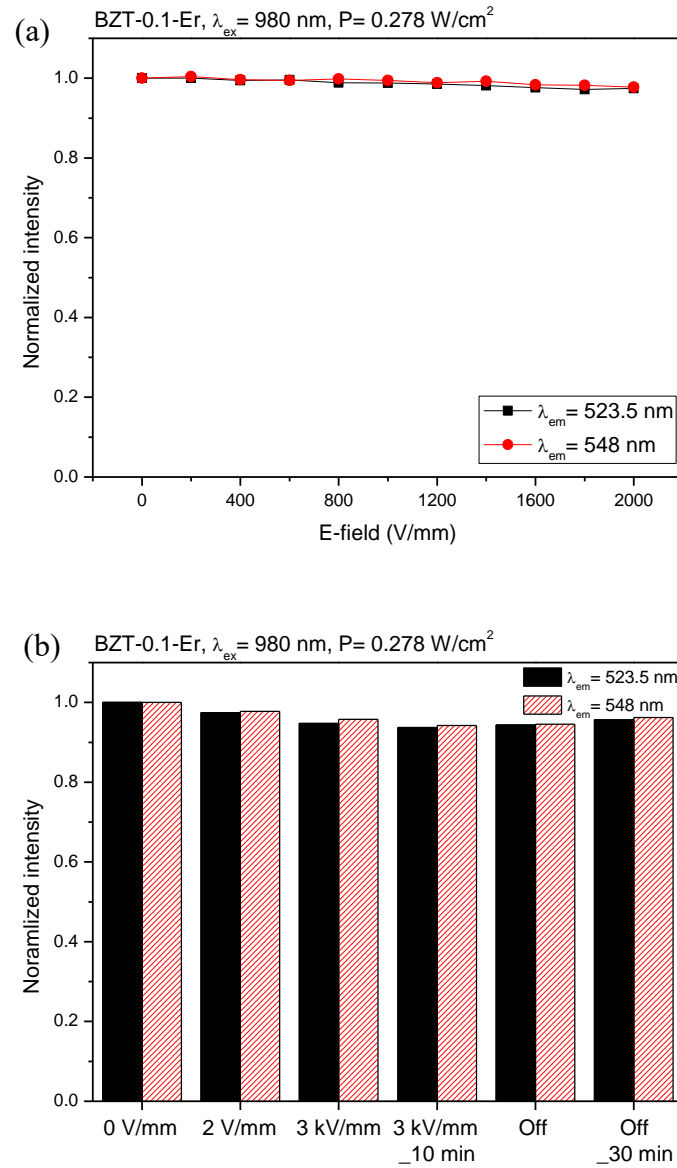


**FIGURE 5-2** UC PL response under (a) different E-fields, and (b) under E-field and removal of field of BZT-0.1-Er ceramic.

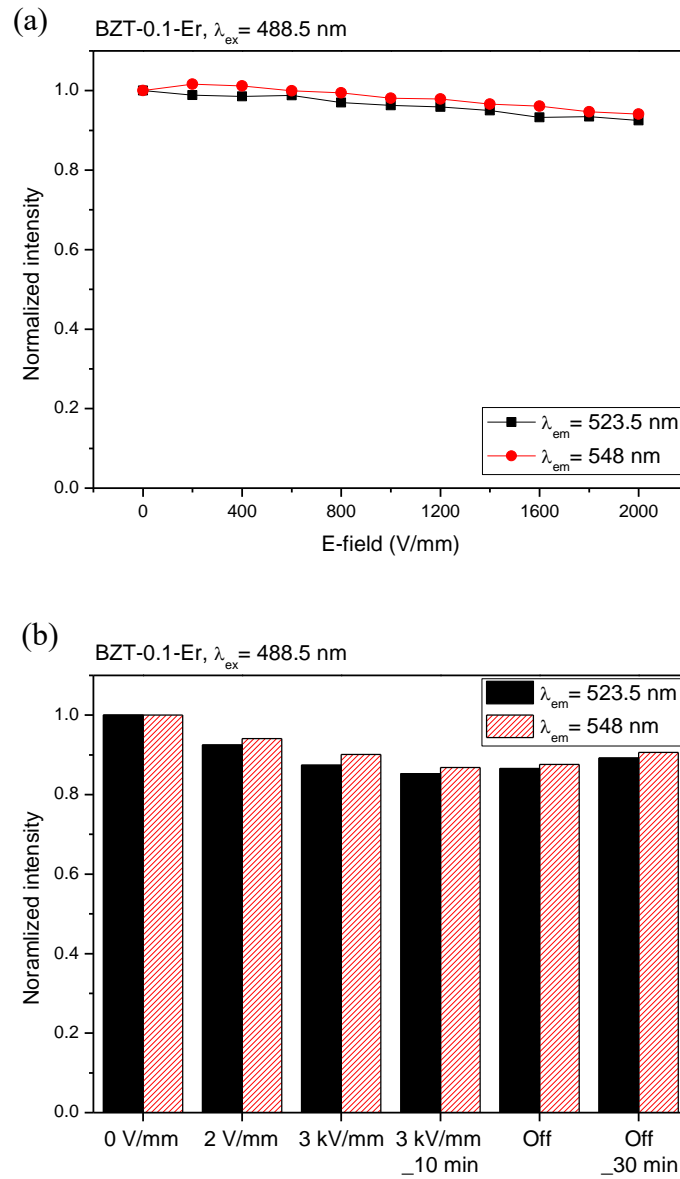


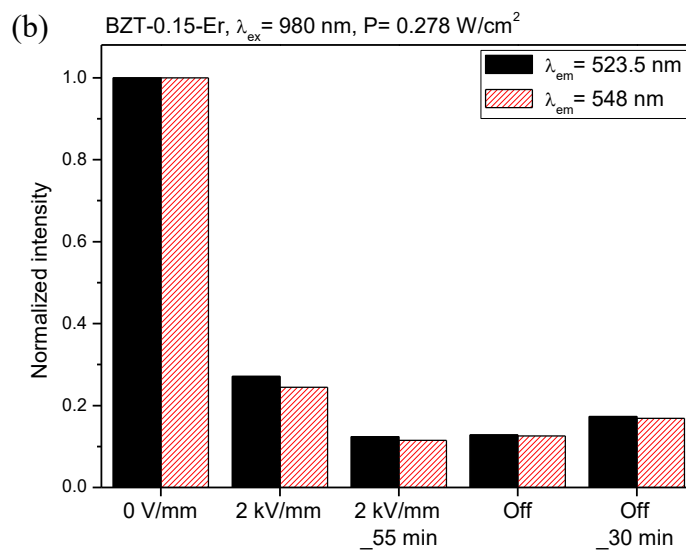
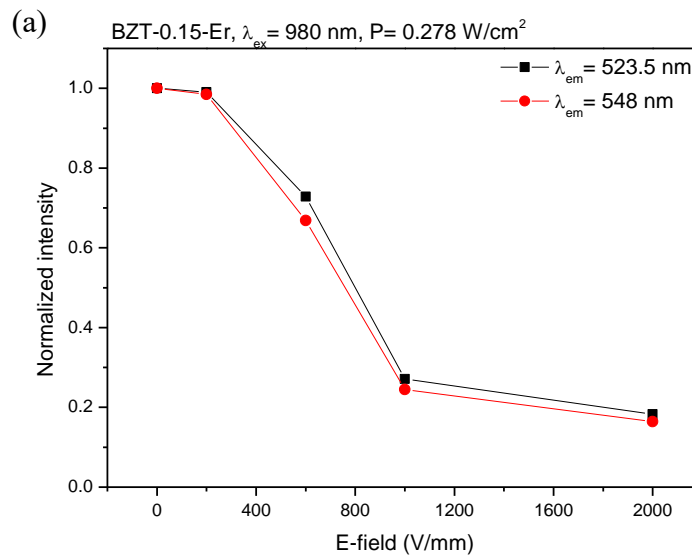
FIGURE 5-3 DC PL response under (a) different E-fields, and (b) under E-field and removal of field of BZT-0.1-Er ceramic.

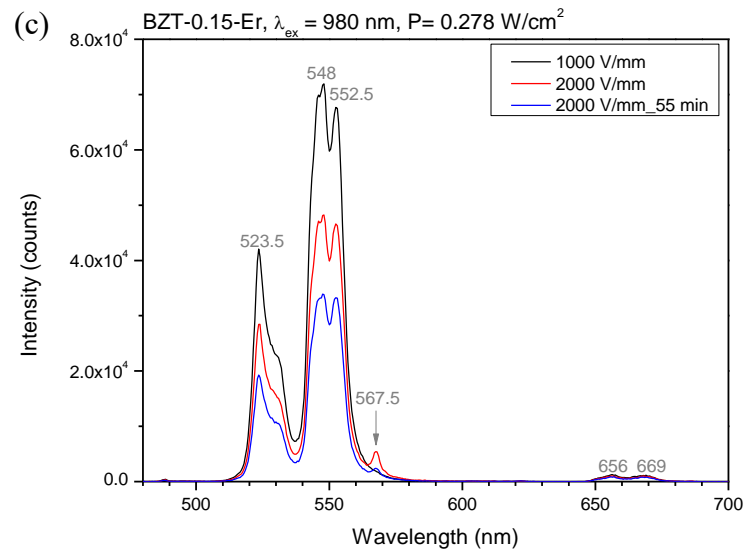


Figure 5-4 (a) shows the variations of the observed UC PL intensities at 523.5 nm and 548 nm with E-field for the BZT-0.15-Er ceramic. The observed PL intensities decrease with increasing E-field, giving a significant decrease of 80% when the E-field reaches 2 kV/mm. Similar to BZT-0.15-Dy, the PL emissions continue to diminish under the E-field. After 55 min under 2 kV/mm, a further decrease of 10% is observed (Figure 5-4 (b)). Only a minor recovery of ~5% is observed in 30 min after the removal of the E-field. As shown in Figure 5-4 (c), an additional PL emission at 567.5 nm appears when the E-field increases to 2 kV/mm. The peak becomes weaker after the field has been applied for 55 min. This may be due to the Stark effect induced by the external E-field as reported by similar works on Eu-doped ceramics [80]. The DC PL emissions exhibit similar dependence on E-field. As shown in Figure 5-5 (a), the observed PL intensities of the two green emissions gradually decrease with increasing E-field. Under an E-field of 2 kV/mm, the PL intensities of two green emissions reduce to 30%. After 20 min under 2 kV/mm, they reduce further to 15% (Figure 5-5 (b)). Similarly, the recovery in PL intensities is only 5% after the removal of E-field for 30 min. As shown in Figure 5-5 (c), the PL intensities recover further to 30% (of the initial values) after 23 h. Thereafter, under an E-field of 2 kV/mm, the PL intensities decrease again to 20% and then to 15% after 20 min. Upon the removal of the E-field, the emissions become somewhat stronger immediately. A recovery of 5% in PL intensities is observed after the field has been removed for 60 min. In general, the reductions in UC and DC PL intensities of the BZT-0.15-Er ceramic are much larger than those for the BZT-0.1-Er ceramic (70% vs 10%). This should be due to its lower  $T_m$  (62°C vs 82°C) and thus a larger increase in the amount of cubic phase resulted from the E-field-induced phase change. When an E-field of 2 kV/mm is applied, the PL intensities of the two green emissions for the BZT-0.15-Er

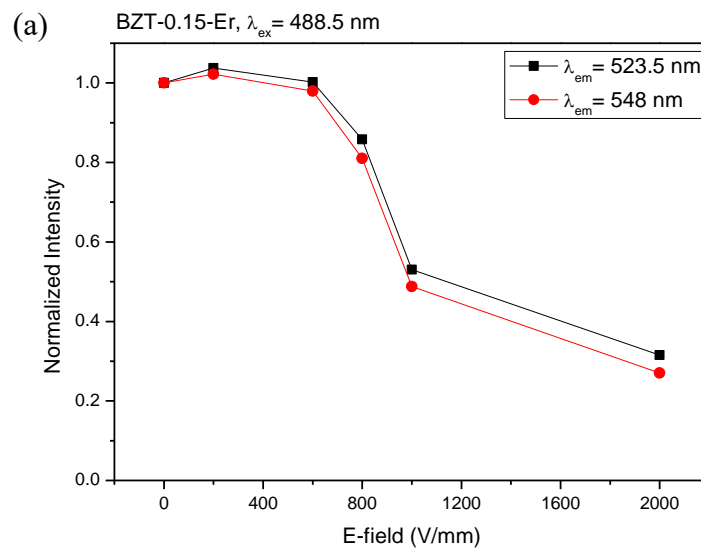


ceramic reduce to 20% and 30% for UC and DC respectively, while the DC PL intensities of the blue and yellow emission for the BZT-0.15-Dy ceramic reduce to 60% and 45% respectively. The larger reductions in PL intensity for the Er-doped ceramics should be attributed to the higher sensitivity of  $\text{Er}^{3+}$  to the crystal symmetry of the host [68], [69]. Also, the limited recovery in PL intensity after the removal of E-field indicates that the effects of polarization alignment and strain are minor for the BZT-0.15-Er ceramic.





**FIGURE 5-4** UC PL response under (a) different E-fields, (b) E-field and removal of field, and (c) UC emission spectra with an additional peak found at 567.5 nm when an E-field of 2 kV/mm is applied, of BZT-0.15-Er ceramic.



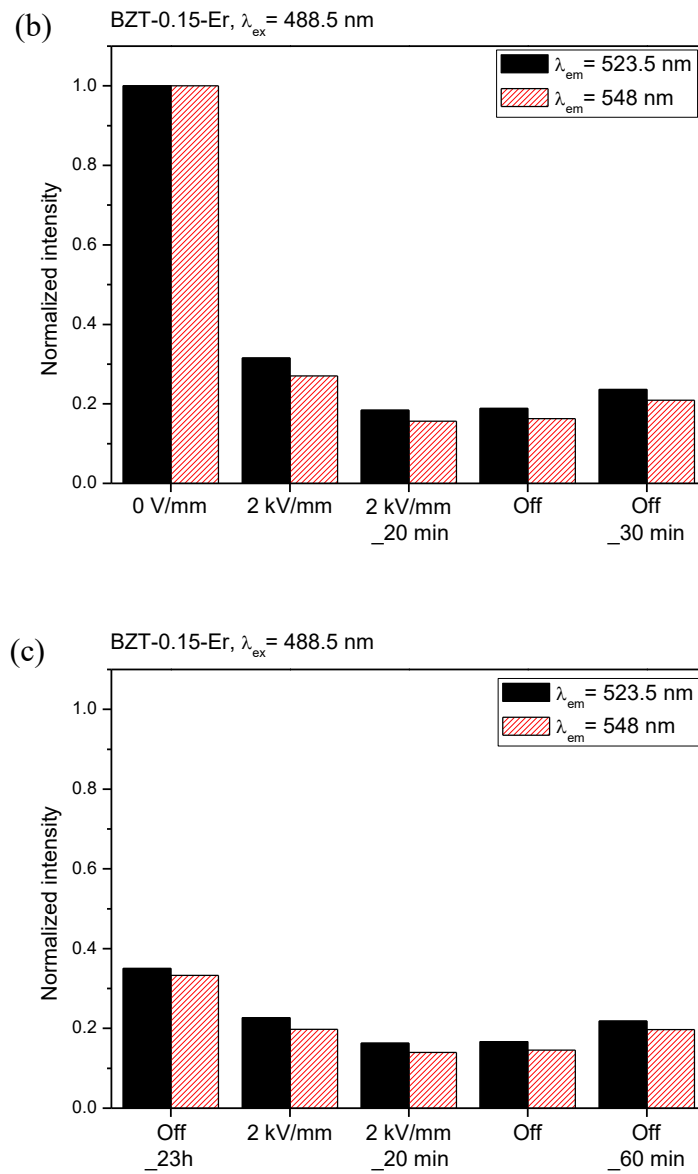
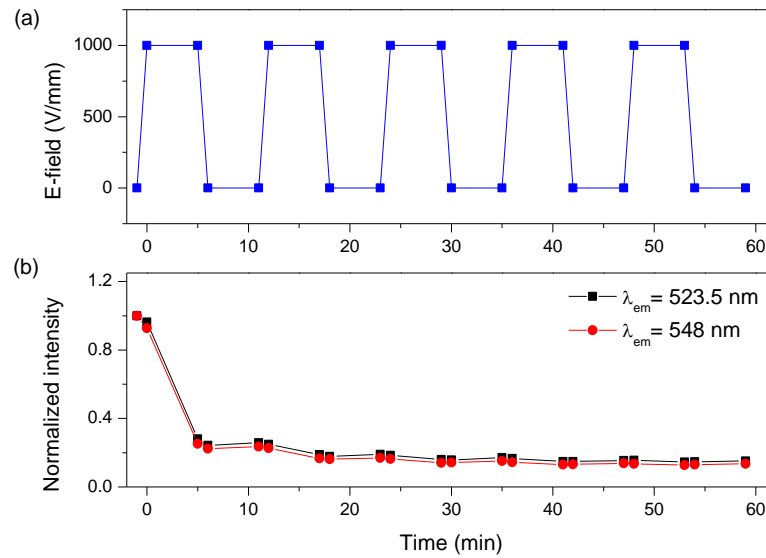


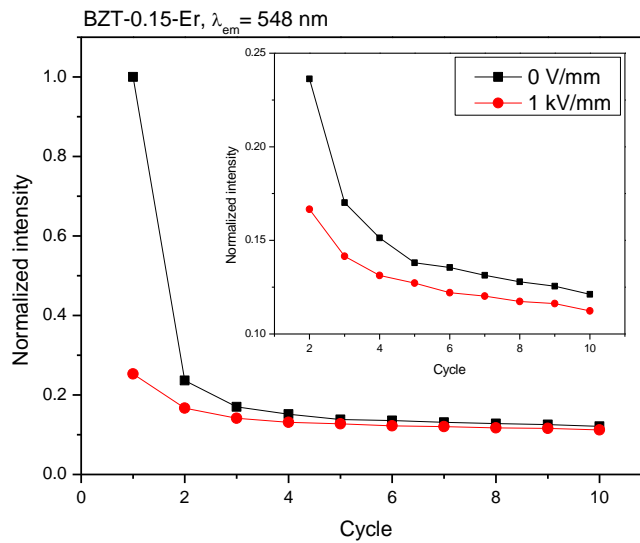
FIGURE 5-5 DC PL response under (a) different E-fields, (b) and (c) under E-field and removal of field of BZT-0.15-Er ceramic.



The reversibility of the E-field-induced DC PL response for the BZT-0.15-Er ceramic has been studied. As shown in Figure 5-6 (a), an E-field switching between 0 and 1 kV/mm for five cycles has been applied to the ceramic. The E-field at each level, i.e., 0 or 1 kV/mm, is kept for 5 min. The observed PL intensities at 523.5 nm and 548 nm are shown in Figure 5-6 (b). In the 1<sup>st</sup> cycle, the observed PL intensities reduce significantly to ~25% upon the application of the E-field. However, almost no recovery is observed after the E-field is removed for 5 min. A further decrease of PL intensity to 16% is observed in the 2<sup>nd</sup> cycle, and similarly the PL intensity remains almost unchanged after the removal of the E-field. Figure 5-7 shows the variations of the normalized PL intensities at 0 and 1 kV/mm in ten E-field cycles, while the inset enlarges the plot in the 2<sup>nd</sup> - 10<sup>th</sup> cycles for the ease of examination. It can be seen that the variation between the PL intensities at 0 V/mm and 1 kV/mm becomes less than 10% since the 2<sup>nd</sup> cycle. For the 5<sup>th</sup> - 10<sup>th</sup> cycles, the variation is just ~1%. As discussed, the reduction in PL intensity is attributed to the change in structural symmetry arisen from the E-field-induced rhombohedral-to-cubic phase change. The low reversibility of the PL response should thus indicate that the phase change is irreversible.



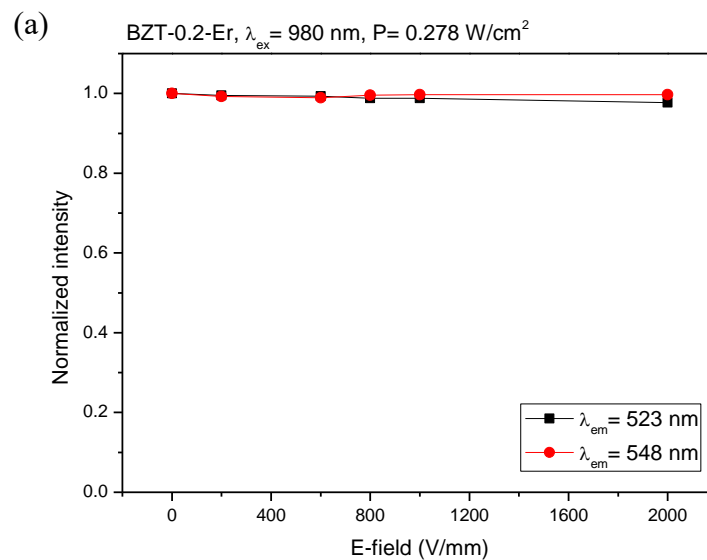
**FIGURE 5-6** (a) Variation of applied E-field and (b) the two observed DC PL intensities of BZT-0.15-Er ceramic.



**FIGURE 5-7** DC PL response (at 548 nm) of BZT-0.15-Er ceramic at 0 V/mm and 1 kV/mm in the 10 consecutive E-field cycles. The inset is the magnified 2<sup>nd</sup> - 10<sup>th</sup> cycles.



The UC and DC PL responses of the BZT-0.2-Er ceramic under an E-field in the range of 0-2000 V/mm have been measured. Figures 5-8 (a)-(b) show the variations of the observed PL intensities at 523 nm and 548 nm, respectively, with E-field. The changes of both the observed UC and DC PL intensities are minor ( $< 10\%$ ). This is similar to the BZT-0.2-Dy ceramic that also exhibits a minor change ( $< 10\%$ ) in PL intensities under E-field. As discussed, it is believed that the reduction in PL emission is mainly related to the phase change induced by E-field. The observed  $T_m$  of the BZT-0.2-Er ceramic ( $33^\circ\text{C}$ ) is close to room temperature, so its rhombohedral phase content (at room temperature) should be lesser than those in the BZT-0.1-Er and BZT-0.15-Er ceramics. Therefore, the relative change in cubic phase content induced by E-field is not sufficient to trigger a considerable reduction in PL emissions.



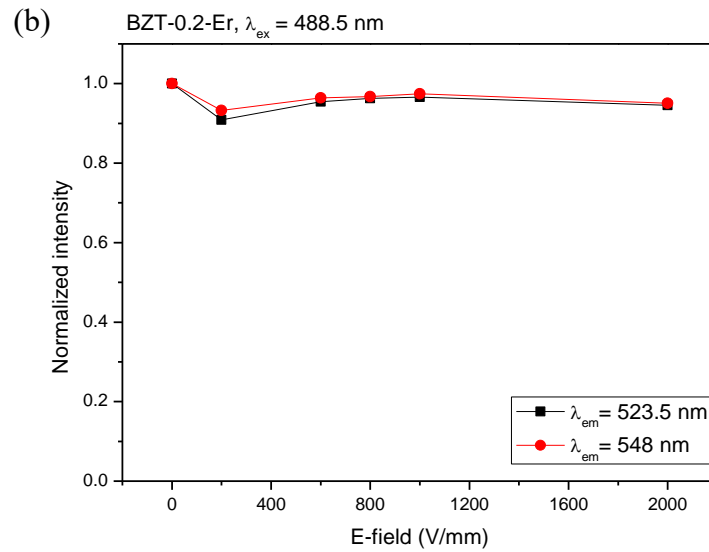
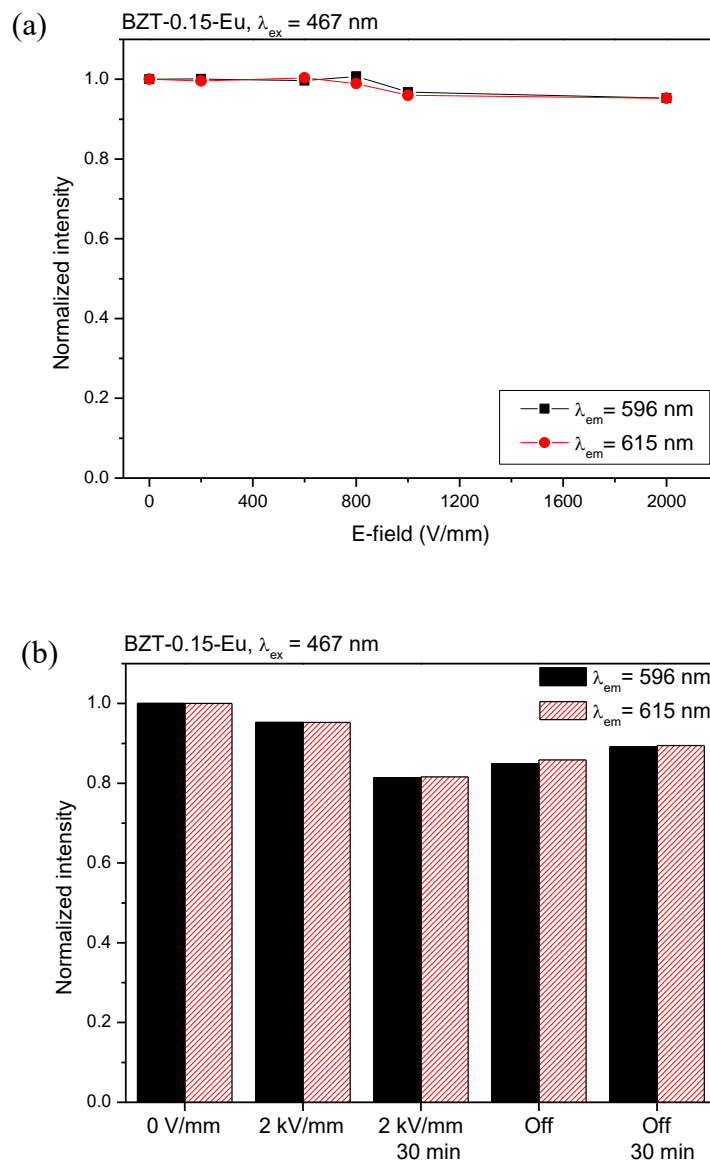


**FIGURE 5-8** (a) UC and (b) DC PL response under different E-fields of BZT-0.2-Er ceramic.

#### 5.4. BZT-x-Eu ceramics

The DC PL responses of the BZT-x-Eu ceramics under an E-field have been studied. The observed DC PL intensities of the two red emissions at 596 nm ( $^5D_0 \rightarrow ^7F_1$ ) and 615 nm ( $^5D_0 \rightarrow ^7F_2$ ) for the BZT-0.15-Eu ceramic under an E-field in the range of 0-2000 V/mm are shown in Figure 5-9 (a). The PL intensities are almost unchanged under an E-field lower than 1 kV/mm, and then decrease slightly by 5% when the E-field reaches 2 kV/mm. Similar to other series of ceramics, the observed PL intensities further decrease to 82% after 30 min under 2 kV/mm (Figure 5-9 (b)). They recover by 8% after the removal of E-field for 30 min. Although the reduction ( $< 20\%$ ) is much lesser than those of the BZT-0.15-Dy ( $\geq 40\%$ ) and BZT-0.15-Er ceramics ( $\geq 75\%$ ), it should still be mainly related to the phase change induced by E-field. When the structural symmetry increases due to the phase change from rhombohedral to cubic, the PL emissions are weakened.

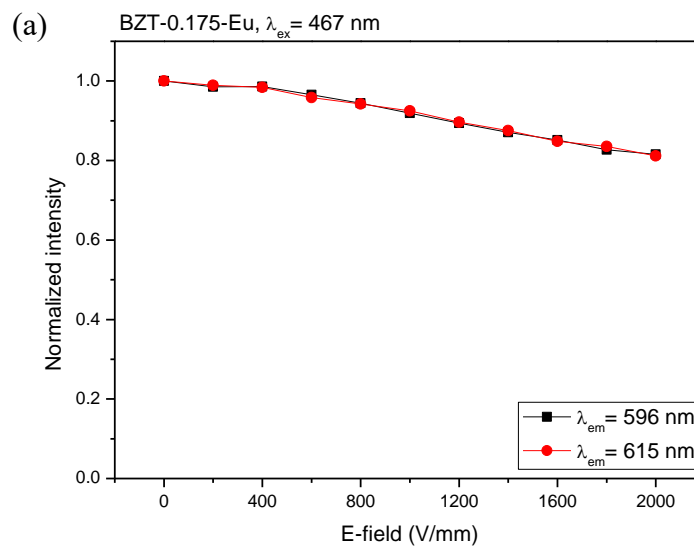
The minor reduction may be due to the high  $T_m$  of the BZT-0.15-Eu ceramic ( $67^\circ\text{C}$ ) and the lesser sensitivity of  $\text{Eu}^{3+}$  to the crystal symmetry of the host. The slight recovery (8%) may suggest that the effect of polarization alignment and strain are also not significant for the BZT-0.15-Eu ceramic.



**FIGURE 5-9** DC PL response under (a) different E-fields, (b) under E-field and removal of field of BZT-0.15-Eu ceramic.



The observed DC PL intensities at 596 nm and 615 nm for the BZT-0.175-Eu ceramic under an E-field in the range of 0-2000 V/mm are shown in Figure 5-10 (a). The PL intensities gradually decrease with increasing E-field. Under an E-field of 2 kV/mm, the observed PL intensities at 596 nm and 615 nm decrease to 82% and 81%, respectively. However, unlike BZT-0.15-Eu, the PL intensities remain almost unchanged under the E-field, only further decreasing about 4 and 2%, respectively, in 30 min (Figure 5-10 (b)). Therefore, increasing the holding time of the E-field does not considerably weaken the PL emissions. The  $T_m$  of the BZT-0.175-Eu ceramic ( $52^\circ\text{C}$ ) is closer to room temperature as compared to BZT-0.15-Eu ( $67^\circ\text{C}$ ), and thus it may response to the E-field faster. It also has lesser rhombohedral content and most of the rhombohedral content has been transformed into cubic phase upon the application of the E-field. The recovery is relatively slight ( $< 5\%$ ), which implies that the effect of polarization alignment and strain are also not significant for the BZT-0.175-Eu ceramic.



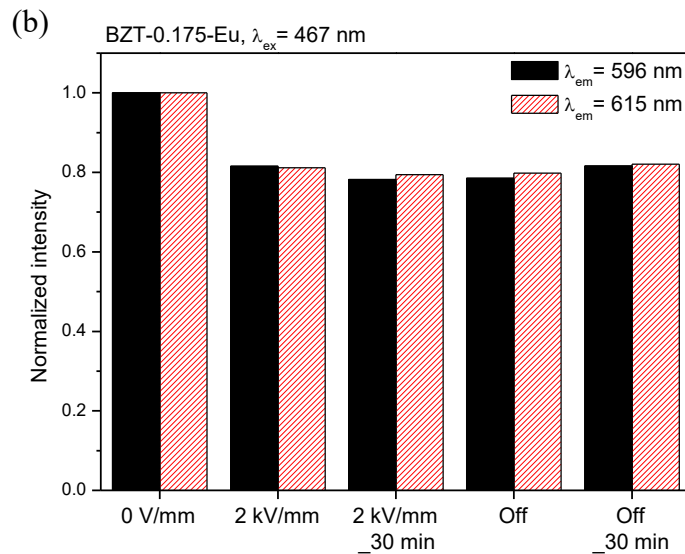


**FIGURE 5-10** DC PL response under (a) different E-fields, (b) under E-field and removal of field of BZT-0.175-Eu ceramic.

The observed DC PL intensities of the two red emissions under an E-field in the range of 0-2000 V/mm for the BZT-0.2-Eu ceramic are shown in Figure 5-11 (a). The observed PL intensities decrease gradually to 94% as the E-field increases from 0 to 2 kV/mm. As shown in Figure 5-11 (b), the PL intensities remain almost unchanged under a higher E-field of 3 kV/mm for 10 min, the PL intensities at 596 nm and 615 nm reduce to 93% and 92% respectively. The reductions in PL intensities are still less than 10%. The recovery after removal of field for 30 min is almost negligible (~1%). The finding is consistent with the one of BZT-0.2-Dy and BZT-0.2-Er as no significant change in PL intensity is observed. Similarly, this may be due to low rhombohedral content of BZT-0.2-Eu so the reduction in PL intensity induced by rhombohedral-to-cubic phase change is limited.

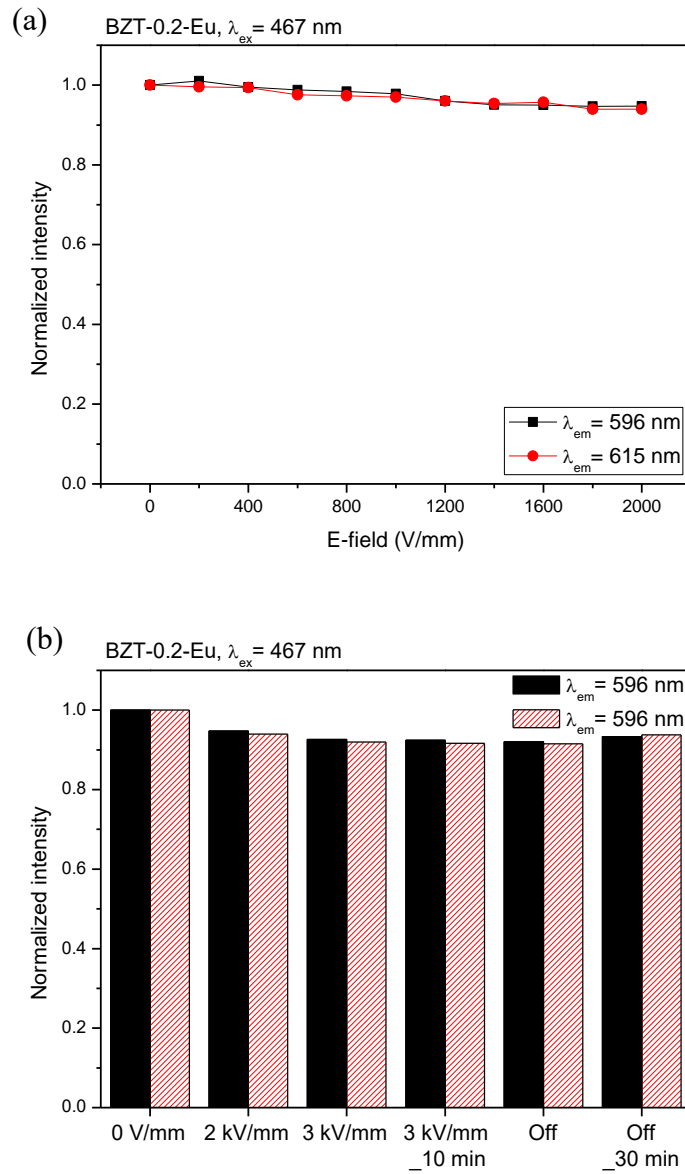


FIGURE 5-11 DC PL response under (a) different E-fields, (b) under E-field and removal of field of BZT-0.2-Eu ceramic.



### 5.5. Conclusions

PL responses under E-field for the BZT-x-RE ceramics have been studied. All the observed PL intensities of the BZT-x-RE ceramics reduce when a sufficiently high E-field is applied. Phase change induced by E-field is proposed as the main reason for the weakened PL emissions. For the BZT-x-RE ceramics (except BZT-0.1-Er), after the phase changes from rhombohedral to cubic (induced by E-field), the structural symmetry increases and thus the PL intensity diminishes. No significant change in PL intensity is found in the BZT-0.1-Er ceramic as the effects of the two transitions rhombohedral-orthorhombic and orthorhombic-tetragonal on structural symmetry are opposite and thus may cancel each other. As compared with BZT-0.15-RE, the BZT-0.2-RE ceramic contains more cubic phase at room temperature and thus shows less change in PL intensity (10% vs  $\geq 20\%$ ). Among the three dopants,  $\text{Er}^{3+}$  is the most sensitive one to the crystal symmetry of the host, as evidenced by the largest reduction of PL intensity (75-80%) in the BZT-0.15-Er ceramic induced by an E-field of 2 kV/mm. The recovery in PL intensity for all the samples is found to be time-dependent and limited. Another factors that may lead to the changes in PL emission is the spontaneous polarization and strain, and the corresponding effects are believed to be minor as little recovery is found after the removal of E-field. The reversibility of E-field-induced PL response has been studied with BZT-0.15-Er ceramic and is found to be low.



## Chapter 6 Conclusions

The present work aims to develop new lead-free rare earth (RE)-doped barium zirconate titanate (BZT)-based ceramics with tunable PL responses under electric field (E-field) at room temperature. Three RE ions,  $\text{Dy}^{3+}$ ,  $\text{Er}^{3+}$  and  $\text{Eu}^{3+}$ , have been used as luminescent activators, and the ceramics have fabricated by the conventional solid-state reaction method. The PL responses of the RE-doped ceramics under E-field have been studied. Moreover, the effects of the three dopants on the dielectric, ferroelectric and piezoelectric properties of BZT ceramics have also been investigated.

$\text{BaZr}_x\text{Ti}_{1-x}\text{O}_3$  (BZT-x) ferroelectric ceramics with  $x = 0.15, 0.2, 0.25$  and  $0.3$  have been fabricated in this work for determining the suitable host. Similar to other research works, the transition temperature  $T_m$  of the ceramics determined based on their temperature-dependent dielectric properties decreases with increasing Zr content. As their  $T_m$  are close to room temperature, the BZT-0.15 and BZT-0.2 ceramics have been selected as the hosts for the RE-doping. Moreover, all the ceramics are well densified to a perovskite structure. They are dense and have irregular-shaped grains. Their ferroelectric and piezoelectric properties are weakened with increasing Zr content.

Three series of luminescent samples have been prepared in this work; they are: (i) BZT-x ceramics ( $x = 0.15$  and  $0.2$ ) doped with  $0.2 \text{ mol}\%$   $\text{Dy}^{3+}$  (BZT-x-Dy); (ii) BZT-x ceramics ( $x = 0.1, 0.15$  and  $0.2$ ) doped with  $0.2 \text{ mol}\%$   $\text{Er}^{3+}$  (BZT-x-Er); and (iii) BZT-x ceramics ( $x = 0.15, 0.175$  and  $0.2$ ) doped with  $0.2 \text{ mol}\%$   $\text{Eu}^{3+}$  (BZT-x-Eu). All the samples are also abbreviated as BZT-x-RE. Except BZT-0.1-Er ceramic that contains both rhombohedral and orthorhombic phase, all the BZT-x-RE ceramics have crystallized in a perovskite structure with both rhombohedral and cubic phase. Through observing the XRD pattern of BZT-0.15-Er ceramic, applying E-field is found may induce



rhombohedral-to-cubic phase change and strain. Both the doping of  $\text{Er}^{3+}$  and  $\text{Eu}^{3+}$  ions have improved the piezoelectric properties of the BZT ceramics. The UC PL properties of the BZT-x-Er ceramics have been studied. Based on the power-dependent measurements, multi-photon absorption process is confirmed in the UC emission. Typical DC PL emissions are obtained for all the BZT-x-RE ceramics. For studying the effects of structural phase change, the UC PL emissions of the BZT-0.15-Er ceramic and the DC PL emissions of the BZT-x-Eu ( $x = 0.15$  and  $0.175$ ) ceramics have been measured at functions of temperature. Due to the increase in structural symmetry resulted from the thermally induced rhombohedral-to-cubic phase change, the PL intensity decreases with increasing temperature. Moreover, the result of the BZT-0.15-Er ceramic reveals the occurrence of thermal agitation (TAG) between two thermally coupled emission levels  $^4\text{S}_{3/2}$  and  $^2\text{H}_{11/2}$ .

The PL responses under E-field for the BZT-x-RE ceramics have been studied. The observed PL intensities of all the BZT-x-RE ceramics are found diminished under a sufficiently high E-field. Phase change induced by E-field is believed to be the major cause for the weakening of PL intensity. Under a sufficiently high E-field, rhombohedral-to-cubic phase change happens for all the BZT-x-RE ceramics (except BZT-0.1-Er), and thus leading to an enhancement in structural symmetry and then a reduction in PL intensity. For the BZT-0.1-Er ceramic, rhombohedral-to-orthorhombic as well as orthorhombic-to-tetragonal phase changes occur under an E-field. As their effects on structural symmetry are opposed, the overall change in PL intensity becomes insignificant. Under an E-field of 2 kV/mm, the BZT-0.2-RE ceramics, which contain more cubic phase at room temperature, show less change ( $< 10\%$ ) in PL intensity as compared to the BZT-0.15-RE ceramics ( $\geq 20\%$ ). Owing the higher sensitivity to the host crystal symmetry, the



BZT-0.15-Er ceramic exhibits the largest reduction in PL intensity (75-80%) under an E-field of 2 kV/mm. After the removal of E-field, the recovery in PL intensity is found to be time-dependent and limited ( $< 10\%$ ) for all the ceramics. This indicates that the E-field-induced rhombohedral-to-cubic phase change is irreversible and the effect of polarization switching, which is another factor that leading to changes in PL emissions, is small.



## References

- [1] R. E. Cohen, "Origin of ferroelectricity in perovskite oxides," *Nature*, vol. 358, no. 6382, pp. 136–138, 1992.
- [2] G. H. Haertling, "Ferroelectric Ceramics: History and Technology," *J. Am. Ceram. Soc.*, vol. 82, p. 797, 1999.
- [3] R. B. Gary, "Transducer and Method of Making the same," U.S. Pat. No. 2 486 560, 1949.
- [4] K. Uchino, "Advanced Piezoelectric Materials," in *Woodhead Publishing Series in Electronic and Optical Materials*, 2010, pp. 799–800.
- [5] S. Priya and S. Nahm, Eds., *Lead-Free Piezoelectrics*. New York, NY: Springer New York, 2012.
- [6] S. O. Leontsev and R. E. Eitel, "Progress in engineering high strain lead-free piezoelectric ceramics," *Sci. Technol. Adv. Mater.*, vol. 11, no. 4, p. 44302, 2010.
- [7] Y. Saito, H. Takao, T. Tani, T. Nonoyama, K. Takatori, T. Homma, T. Nagaya, and M. Nakamura, "Lead-free piezoceramics," *Nature*, vol. 432, no. 7013, pp. 84–7, 2004.
- [8] P. B. Jamieson, "Ferroelectric Tungsten Bronze-Type Crystal Structures. I. Barium Strontium Niobate  $Ba_{0.27}Sr_{0.75}Nb_2O_5.78$ ," *J. Chem. Phys.*, vol. 48, no. 11, p. 5048, 1968.
- [9] R. Barns, "Barium sodium niobate ( $Ba_{(4+x)}Na_{(2-2x)}Nb_{10}O_{30}$ ): crystallographic data and thermal expansion coefficients," *J. Appl. Crystallogr.*, vol. 1, no. 5, pp. 290–292, 1968.
- [10] S. C. Abrahams, P. B. Jamieson, and J. L. Bernstein, "Ferroelectric Tungsten Bronze-Type Crystal Structures. III. Potassium Lithium Niobate  $K_{(6-x-y)}Li_{(4+x)}Nb_{(10+y)}O_{30}$ ," *J. Chem. Phys.*, vol. 54, no. 6, pp. 2355–2364, 1971.
- [11] K. W. Kwok and H. Y. Wong, "Piezoelectric and pyroelectric properties of Cu-doped  $CaBi_4Ti_4O_{15}$  lead-free ferroelectric ceramics," *J. Phys. D: Appl. Phys.*, vol. 42, no. 9, p. 95419, May 2009.
- [12] B. Aurivillius, "Mixed bismuth oxides with layer lattices. II. Structure of  $Bi_4Ti_3O_{12}$ ," *Ark. foer Kemi*, vol. 1, pp. 499–512, 1949.
- [13] G. Li, L. Zheng, Q. Yin, B. Jiang, and W. Cao, "Microstructure and ferroelectric properties of MnO[sub 2]-doped bismuth-layer  $(Ca,Sr)Bi_4Ti_4O_{15}$  ceramics," *J. Appl. Phys.*, vol. 98, no. 6, p. 64108, 2005.



- [14] T. B. Wu, C. M. Wu, and M. L. Chen, "Highly insulative barium zirconate-titanate thin films prepared by rf magnetron sputtering for dynamic random access memory applications," *Appl. Phys. Lett.*, vol. 69, no. 18, pp. 2659–2661, 1996.
- [15] Z. Yu, C. Ang, R. Guo, and A. S. Bhalla, "Piezoelectric and strain properties of  $\text{Ba}(\text{Ti}_{1-x}\text{Zr}_x)\text{O}_3$  ceramics," *J. Appl. Phys.*, vol. 92, no. 3, p. 1489, 2002.
- [16] J. Q. Qi, B. B. Liu, H. Y. Tian, H. Zou, Z. X. Yue, and L. T. Li, "Dielectric properties of barium zirconate titanate (BZT) ceramics tailored by different donors for high voltage applications," *Solid State Sci.*, vol. 14, no. 10, pp. 1520–1524, 2012.
- [17] D. Hennings, A. Schnell, and G. Simon, "Diffuse ferroelectric phase transitions in  $\text{Ba}(\text{Ti}_{1-y}\text{Zr}_y)\text{O}_3$  ceramics," *J. Am. Ceram. Soc.*, vol. 65, no. 11, pp. 539–544, 1982.
- [18] R. C. Kell and N. J. Hellicar, "Structural transitions in barium titanate-zirconate transducer materials," *Acta Acust. united with Acust.*, vol. 6, no. 2, pp. 235–245, 1956.
- [19] H. H. Huang, H. H. Chiu, N. C. Wu, and M. C. Wang, "Tetragonality and properties of  $\text{Ba}(\text{Zr}_x\text{Ti}_{1-x})\text{O}_3$  ceramics determined using the Rietveld method," *Metall. Mater. Trans. A Phys. Metall. Mater. Sci.*, vol. 39, no. 13, pp. 3276–3282, 2008.
- [20] L. Cross, "Relaxor Ferroelectrics," *Ferroelectrics*, vol. 76, no. 1, pp. 241–267, 1987.
- [21] A. Dixit, S. B. Majumder, R. S. Katiyar, and A. S. Bhalla, "Relaxor behavior in sol-gel-derived  $\text{BaZr}_{(0.40)}\text{Ti}_{(0.60)}\text{O}_3$  thin films," *Appl. Phys. Lett.*, vol. 82, no. 16, pp. 2679–2681, 2003.
- [22] D. Viehland, M. Wuttig, and L. E. Cross, "The glassy behavior of relaxor ferroelectrics," *Ferroelectrics*, vol. 120, no. 1, pp. 71–77, 1991.
- [23] H. T. Martirena and J. C. Burfoot, "Grain-size and pressure effects on the dielectric and piezoelectric properties of hot-pressed PZT-5," *Ferroelectrics*, vol. 7, no. 1, pp. 151–152, 1974.
- [24] K. Uchino and S. Nomura, "Critical exponents of the dielectric constants in diffused-phase-transition crystals," *Ferroelectr. Lett. Sect.*, vol. 44, no. 3, pp. 55–61, 1982.
- [25] X. G. Tang, J. Wang, X. X. Wang, and H. L. W. Chan, "Effects of grain size on the dielectric properties and tunabilities of sol-gel derived  $\text{Ba}(\text{Zr}_{0.2}\text{Ti}_{0.8})\text{O}_3$  ceramics," *Solid State Commun.*, vol. 131, no. 3–4, pp. 163–168, 2004.
- [26] X. G. Tang, K.-H. Chew, and H. L. W. Chan, "Diffuse phase transition and dielectric tunability of  $\text{Ba}(\text{Zr}_y\text{Ti}_{1-y})\text{O}_3$  relaxor ferroelectric ceramics," *Acta Mater.*, vol. 52, no. 17, pp. 5177–5183, 2004.



- [27] A. K. Tagantsev, V. O. Sherman, K. F. Astafiev, J. Venkatesh, and N. Setter, "Ferroelectric materials for microwave tunable applications," *J. Electroceramics*, vol. 11, no. 1–2, pp. 5–66, 2003.
- [28] V. Buscaglia, S. Tripathi, V. Petkov, M. Dapiaggi, M. Deluca, A. Gajovic, and Y. Ren, "Average and local atomic-scale structure in  $\text{BaZr}_x\text{Ti}_{1-x}\text{O}_3$  ( $x = 0.10, 0.20, 0.40$ ) ceramics by high-energy x-ray diffraction and Raman spectroscopy," *J. Phys. Condens. Matter*, vol. 26, no. 6, p. 65901, Feb. 2014.
- [29] Q. Xu, D. Zhan, D. P. Huang, H. X. Liu, W. Chen, and F. Zhang, "Dielectric inspection of  $\text{BaZr}_{0.2}\text{Ti}_{0.8}\text{O}_3$  ceramics under bias electric field: A survey of polar nano-regions," *Mater. Res. Bull.*, vol. 47, no. 7, pp. 1674–1679, 2012.
- [30] R. Farhi, M. El Marssi, A. Simon, and J. Ravez, "A Raman and dielectric study of ferroelectric  $\text{Ba}(\text{Ti}_{1-x}\text{Zr}_x)\text{O}_3$  ceramics," *Eur. Phys. J. B - Condens. Matter Complex Syst.*, vol. 9, no. 4, pp. 599–604, 1999.
- [31] S. M. Neirman, "The Curie point temperature of  $\text{Ba}(\text{Ti}_{1-x}\text{Zr}_x)\text{O}_3$  solid solutions," *J. Mater. Sci.*, vol. 23, no. 11, pp. 3973–3980, 1988.
- [32] Z. Yu, R. Guo, and A. S. Bhalla, "Growth of  $\text{Ba}(\text{Ti}_{1-x}\text{Zr}_x)\text{O}_3$  single crystals by the laser heated pedestal growth technique," *J. Cryst. Growth*, vol. 233, pp. 460–465, 2001.
- [33] P. W. Rehrig, S.-E. Park, S. Trolier-McKinstry, G. L. Messing, B. Jones, and T. R. Shrout, "Piezoelectric properties of zirconium-doped barium titanate single crystals grown by templated grain growth," *J. Appl. Phys.*, vol. 86, no. 3, p. 1657, 1999.
- [34] H. Maiwa, "Preparation and Properties of  $\text{BaTiO}_3$  and  $\text{Ba}(\text{Zr,Ti})\text{O}_3$  Ceramics by Spark Plasma Sintering," in *Advances in Ceramics - Electric and Magnetic Ceramics, Bioceramics, Ceramics and Environment*, vol. 47, no. 9 PART 2, InTech, 2011, pp. 7646–7649.
- [35] B. Valeur and M. N. Berberan-Santos, "A brief history of fluorescence and phosphorescence before the emergence of quantum theory," *J. Chem. Educ.*, vol. 88, no. 6, pp. 731–738, 2011.
- [36] S. E. Braslavsky, "Glossary of terms used in photochemistry, 3rd edition (IUPAC Recommendations 2006)," *Pure Appl. Chem.*, vol. 79, no. 3, pp. 293–465, 2007.
- [37] K. N. Shinde, S. J. Dhoble, H. C. Swart, and K. Park, *Phosphate Phosphors for Solid-State Lighting*, vol. 174. Berlin, Heidelberg: Springer, 2012.



- [38] M. V. DaCosta, S. Doughan, Y. Han, and U. J. Krull, “Lanthanide upconversion nanoparticles and applications in bioassays and bioimaging: A review,” *Anal. Chim. Acta*, vol. 832, pp. 1–33, 2014.
- [39] F. Auzel, “Upconversion and Anti-Stokes Processes with f and d Ions in Solids,” *Chem. Rev.*, vol. 104, no. 1, pp. 139–173, 2004.
- [40] H. Dong, L.-D. Sun, and C.-H. Yan, “Energy transfer in lanthanide upconversion studies for extended optical applications,” *Chem. Soc. Rev.*, vol. 44, no. 6, pp. 1608–1634, 2015.
- [41] P. Salas and H. Desirena, “Enhanced cooperative absorption and upconversion in Yb<sup>3+</sup> doped YAG nanophosphors,” *Opt. Mater. (Amst.)*, vol. 27, pp. 1305–1310, 2005.
- [42] Q. Song, C. Li, J. Li, and W. Ding, “Photoluminescence properties of the Yb : Er co-doped Al<sub>2</sub>O<sub>3</sub> thin film fabricated by microwave ECR plasma source enhanced RF magnetron sputtering,” *Opt. Mater. (Amst.)*, vol. 28, pp. 1344–1349, 2006.
- [43] F. Wang and X. Liu, “Recent advances in the chemistry of lanthanide-doped upconversion nanocrystals,” *Chem. Soc. Rev.*, vol. 38, no. 4, pp. 976–989, 2009.
- [44] F. Wang, D. Banerjee, Y. Liu, X. Chen, and X. Liu, “Upconversion nanoparticles in biological labeling, imaging, and therapy,” *Analyst*, vol. 135, no. 8, pp. 1839–1854, 2010.
- [45] F. Wang, R. Deng, J. Wang, Q. Wang, Y. Han, H. Zhu, Z. Chen, and X. Liu, “Tuning upconversion through energy migration in core-shell nanoparticles,” *Nat. Mater.*, vol. 10, pp. 968–973, 2011.
- [46] B. S. Richard and A. Shalav, “The role of polymers in the luminescence conversion of sunlight for enhanced solar cell performance,” *Synth. Met.*, vol. 154, no. 1–3, pp. 61–64, 2005.
- [47] Y.-W. Su, S.-C. Lan, and K.-H. Wei, “Organic photovoltaics,” *Mater. Today*, vol. 15, no. 12, pp. 554–562, 2012.
- [48] N. G. Connelly, T. Damhus, R. M. Hartshorn, and A. T. Hutton, Eds., *Nomenclature of Inorganic Chemistry: IUPAC Recommendations 2005*. Cambridge: The Royal Society of Chemistry, 2005.
- [49] G. Liu, “Advances in the theoretical understanding of photon upconversion in rare-earth activated nanophosphors,” *Chem. Soc. Rev.*, vol. 44, pp. 1635–1652, 2015.
- [50] D. C. Arnold, “Composition-Driven Structural Phase Transitions in Rare-Earth-Doped BiFeO<sub>3</sub> Ceramics : A Review,” *Ieee Trans. Ultrason. Ferroelectr. Freq. Control*, vol. 62, no. 1, pp. 62–82, 2015.



- [51] S. Xiu, S. Xiao, W. Zhang, S. Xue, B. Shen, and J. Zhai, "Effect of rare-earth additions on the structure and dielectric energy storage properties of  $\text{Ba}_x\text{Sr}_{1-x}\text{TiO}_3$ -based barium boronaluminosilicate glass-ceramics," *J. Alloys Compd.*, vol. 670, pp. 217–221, 2016.
- [52] X. Wang, Q. Liu, Y. Bu, C.-S. Liu, T. Liu, and X. Yan, "Optical temperature sensing of rare-earth ion doped phosphors," *RSC Adv.*, vol. 5, no. 105, pp. 86219–86236, 2015.
- [53] J. Liu, C. L. Wang, Y. Li, W. B. Su, Y. H. Zhu, J. C. Li, and L. M. Mei, "Influence of rare earth doping on thermoelectric properties of  $\text{SrTiO}_3$  ceramics," *J. Appl. Phys.*, vol. 114, no. 22, 2013.
- [54] M. Reddi Babu, N. Madhusudhana Rao, A. Mohan Babu, N. Jaidass, C. Krishna Moorthy, and L. Rama Moorthy, "Effect of  $\text{Dy}^{3+}$  ions concentration on optical properties of lead borosilicate glasses for white light emission," *Optik (Stuttg.)*, vol. 127, no. 5, pp. 3121–3126, 2016.
- [55] X. Zhang, Z. Lu, F. Meng, L. Hu, X. Xu, J. Lin, and C. Tang, "Luminescence properties of  $\text{Ca}_3\text{Si}_2\text{O}_7$ :  $\text{Dy}^{3+}$  phosphor for white light-emitting diodes," *Mater. Lett.*, vol. 79, no. 76, pp. 292–295, 2012.
- [56] J. Kuang, Y. Liu, and J. Zhang, "White-light-emitting long-lasting phosphorescence in  $\text{Dy}^{3+}$ -doped  $\text{SrSiO}_3$ ," *J. Solid State Chem.*, vol. 179, no. 1, pp. 266–269, 2006.
- [57] Y. Liu, G. Liu, J. Wang, X. Dong, and W. Yu, "Single-Component and Warm-White-Emitting Phosphor  $\text{NaGd}(\text{WO}_4)_2$ : $\text{Tm}^{3+}$ ,  $\text{Dy}^{3+}$ ,  $\text{Eu}^{3+}$ : Synthesis, Luminescence, Energy Transfer, and Tunable Color.," *Inorg. Chem.*, vol. 4, 2014.
- [58] S. Das, A. Amarnath Reddy, S. Surendra Babu, and G. Vijaya Prakash, "Controllable white light emission from  $\text{Dy}^{3+}$ - $\text{Eu}^{3+}$  co-doped  $\text{KCaBO}_3$  phosphor," *J. Mater. Sci.*, vol. 46, no. 24, pp. 7770–7775, 2011.
- [59] S. Das, C.-Y. Yang, and C.-H. Lu, "Structural and Optical Properties of Tunable Warm-White Light-Emitting  $\text{ZrO}_2$ : $\text{Dy}^{3+}$ - $\text{Eu}^{3+}$  Nanocrystals," *J. Am. Ceram. Soc.*, vol. 96, no. 5, pp. 1602–1609, 2013.
- [60] H. Guan, G. Liu, J. Wang, X. Dong, and W. Yu, "Tunable luminescence and energy transfer properties of  $\text{NaGdF}_4$ : $\text{Dy}^{3+}$ ,  $\text{Eu}^{3+}$  nanophosphors," *New J. Chem.*, vol. 38, no. 10, pp. 4901–4907, 2014.
- [61] S. E. Hao, L. Sun, and J. X. Huang, "Preparation and dielectric properties of Dy, Er-doped  $\text{BaZr}_{0.2}\text{Ti}_{0.8}\text{O}_3$  ceramics," *Mater. Chem. Phys.*, vol. 109, no. 1, pp. 45–49, 2008.



- [62] K. Watanabe, H. Ohsato, H. Kishi, and Y. Okino, "Solubility of La–Mg and La–Al in BaTiO<sub>3</sub>," *Solid State Ionics*, vol. 108, pp. 129–135, 1998.
- [63] L. Chen, B. C. Luo, N. Y. Chan, J. Y. Dai, M. Hoffman, S. Li, and D. Y. Wang, "Enhancement of photovoltaic properties with Nb modified (Bi,Na)TiO<sub>3</sub>-BaTiO<sub>3</sub> ferroelectric ceramics," *J. Alloys Compd.*, vol. 587, pp. 339–343, 2014.
- [64] P. Du, L. Luo, W. Li, Q. Yue, and H. Chen, "Optical temperature sensor based on upconversion emission in Er-doped ferroelectric 0.5Ba(Zr<sub>0.2</sub>Ti<sub>0.8</sub>)O<sub>3</sub>-0.5(Ba<sub>0.7</sub>Ca<sub>0.3</sub>)TiO<sub>3</sub> ceramic," *Appl. Phys. Lett.*, vol. 104, no. 15, p. 152902, 2014.
- [65] B. Dong, B. Cao, Y. He, Z. Liu, Z. Li, and Z. Feng, "Temperature sensing and in vivo imaging by molybdenum sensitized visible upconversion luminescence of rare-earth oxides," *Adv. Mater.*, vol. 24, no. 15, pp. 1987–1993, 2012.
- [66] L. H. Fischer, G. S. Harms, and O. S. Wolfbeis, "Upconverting nanoparticles for nanoscale thermometry," *Angew. Chemie - Int. Ed.*, vol. 50, no. 20, pp. 4546–4551, 2011.
- [67] M. D. Shinn, W. A. Sibley, M. G. Drexhage, and R. N. Brown, "Optical transitions of Er<sup>3+</sup> ions in fluorozirconate glass," *Phys. Rev. B*, vol. 27, no. 11, pp. 6635–6648, 1983.
- [68] X. Wu, S. Lu, and K. W. Kwok, "Photoluminescence, electro-optic response and piezoelectric properties in pressureless-sintered Er-doped KNN-based transparent ceramics," *J. Alloys Compd.*, vol. 695, no. January 2017, pp. 3573–3578, 2017.
- [69] Y. Yao, L. Luo, W. Li, J. Zhou, and F. Wang, "An intuitive method to probe phase structure by upconversion photoluminescence of Er<sup>3+</sup> doped in ferroelectric Pb(Mg<sub>1/3</sub>Nb<sub>2/3</sub>)O<sub>3</sub>-PbTiO<sub>3</sub>," *Appl. Phys. Lett.*, vol. 106, no. 8, pp. 1–5, 2015.
- [70] G. Muller, "Luminescent chiral lanthanide(III) complexes as potential molecular probes," *Dalton Trans.*, no. 44, pp. 9692–707, 2009.
- [71] F. Richardson, "Selection rules for lanthanide optical activity," *Inorg. Chem.*, no. 10, pp. 2806–2812, 1980.
- [72] G. N. Bhargavi and A. Khare, "Effect of UV Irradiation on Thermoluminescence Properties of Perovskite Structured Pure and Europium Doped Barium Zirconium Titanate," *Int. J. Lumin. Appl.*, vol. 5, no. 1, pp. 115–117, 2015.
- [73] E. Downing, L. Hesselink, J. Ralston, and R. Macfarlane, "A Three-Color, Solid-State, Three-Dimensional Display," *Science.*, vol. 273, no. 5279, pp. 1185–1189, 1996.
- [74] K. De Greve, L. Yu, P. L. McMahon, J. S. Pelc, C. M. Natarajan, N. Y. Kim, E. Abe, S. Maier, C. Schneider, M. Kamp, S. Höfling, R. H. Hadfield, A. Forchel, M. M. Fejer, and



---

**THE HONG KONG POLYTECHNIC UNIVERSITY**

---

- Y. Yamamoto, “Quantum-dot spin–photon entanglement via frequency downconversion to telecom wavelength,” *Nature*, vol. 491, no. V, p. 421, 2012.
- [75] N. E. Korsunskaya, M. Dybiec, L. Zhukov, S. Ostapenko, and T. Zhukov, “Reversible and non-reversible photo-enhanced luminescence in CdSe/ZnS quantum dots,” *Semicond. Sci. Technol.*, vol. 20, no. 8, pp. 876–881, 2005.
- [76] S.-J. Park, S.-G. Kang, M. Fryd, J. G. Saven, and S. Park, “Highly Tunable Photoluminescent Properties of Amphiphilic Conjugated Block Copolymers,” *J. Am. Chem. Soc.*, vol. 132, no. 29, pp. 9931–9933, Jul. 2010.
- [77] X. Wu, T. H. Chung, H. Sun, and K. W. Kwok, “Tunable photoluminescence properties of Pr<sup>3+</sup>/Er<sup>3+</sup>-doped 0.93Bi<sub>0.5</sub>Na<sub>0.5</sub>TiO<sub>3</sub>–0.07BaTiO<sub>3</sub> low-temperature sintered multifunctional ceramics,” *Ceram. Int.*, vol. 42, no. 8, pp. 9899–9905, 2016.
- [78] H. L. Sun, X. Wu, T. H. Chung, and K. W. Kwok, “In-situ Electric Field-Induced Modulation of Photoluminescence in Pr-doped Ba<sub>0.85</sub>Ca<sub>0.15</sub>Ti<sub>0.90</sub>Zr<sub>0.10</sub>O<sub>3</sub> Lead-Free Ceramics,” *Sci. Rep.*, vol. 6, no. March, p. 28677, 2016.
- [79] J. Hao, Y. Zhang, and X. Wei, “Electric-induced enhancement and modulation of upconversion photoluminescence in epitaxial BaTiO<sub>3</sub>:Yb/Er thin films,” *Angew. Chemie - Int. Ed.*, vol. 50, no. 30, pp. 6876–6880, 2011.
- [80] D. K. Khatua, A. Kalaskar, and R. Ranjan, “Tuning Photoluminescence Response by Electric Field in Electrically Soft Ferroelectrics,” *Phys. Rev. Lett.*, vol. 116, no. 11, p. 117601, 2016.
- [81] Z. Liang, E. Sun, Z. Liu, Z. Zhang, J. Zeng, W. Ruan, G. Li, and W. Cao, “Electric field induced upconversion fluorescence enhancement and its mechanism in Er<sup>3+</sup> doped 0.75Pb(Mg<sub>1/3</sub>Nb<sub>2/3</sub>)O<sub>3</sub>–0.25PbTiO<sub>3</sub> transparent ceramic,” *Appl. Phys. Lett.*, vol. 109, no. 13, p. 132904, 2016.
- [82] T. Taniguchi, T. Murakami, A. Funatsu, K. Hatakeyama, M. Koinuma, and Y. Matsumoto, “Reversibly tunable upconversion luminescence by host-guest chemistry,” *Inorganic Chemistry*, vol. 53, no. 17, pp. 9151–9155, 2014.
- [83] K. Liu, H. You, Y. Zheng, G. Jia, Y. Song, Y. Huang, M. Yang, J. Jia, N. Guo, and H. Zhang, “Facile and rapid fabrication of metal-organic framework nanobelts and color-tunable photoluminescence properties,” *J. Mater. Chem.*, vol. 20, no. 16, pp. 3272–3279, 2010.
- [84] G. Blasse and B. C. Grabmaier, *Luminescent Materials*, vol. 1, no. 3. 1994.



- [85] Edinburgh Instruments Ltd., *FLSP920 Series User Guide*. 2011.
- [86] Z. Yu, C. Ang, R. Guo, and A. S. Bhalla, “Ferroelectric-relaxor behavior of  $\text{Ba}(\text{Ti}_{0.7}\text{Zr}_{0.3})\text{O}_3$  ceramics,” *J. Appl. Phys.*, vol. 92, no. 5, pp. 2655–2657, 2002.
- [87] G. A. Samara, “The relaxational properties of compositionally disordered  $\text{ABO}_3$  perovskites,” *J. Phys. Condens. Matter*, vol. 15, no. 9, pp. R367–R411, 2003.
- [88] X. Chou, J. Zhai, H. Jiang, and X. Yao, “Dielectric properties and relaxor behavior of rare-earth (La, Sm, Eu, Dy, Y) substituted barium zirconium titanate ceramics,” *J. Appl. Phys.*, vol. 102, no. 8, p. 84106, 2007.
- [89] M. J. Weber, “Probabilities for radiative and nonradiative decay of  $\text{Er}^{3+}$  in  $\text{LaF}_3$ ,” *Phys. Rev.*, vol. 157, no. 2, pp. 262–272, 1967.
- [90] L. A. Riseberg and H. W. Moos, “Multiphonon orbit-lattice relaxation of excited states of rare-earth ions in crystals,” *Phys. Rev.*, vol. 174, no. 2, pp. 429–438, 1968.
- [91] R. Reisfeld and Y. Eckstein, “Dependence of spontaneous emission and nonradiative relaxations of  $\text{Tm}^{3+}$  and  $\text{Er}^{3+}$  on glass host and temperature,” *J. Chem. Phys.*, vol. 63, no. 9, p. 4001, 1975.
- [92] A. J. Bell and L. E. Cross, “A phenomenological gibbs function for  $\text{BaTiO}_3$  giving correct E field dependence of all ferroelectric phase changes,” *Ferroelectrics*, vol. 59, pp. 197–203, 1984.
- [93] O. E. Fesenko and V. S. Popov, “Phase T.E-Diagram Of Barium Titanate,” *Ferroelectrics*, vol. 37, no. 1, pp. 729–731, 1981.